AN ABSTRACT OF THE THESIS OF

Edward J. Kohut for the degree of Doctor of Philosophy in Geology presented on February 13, 2004. Title: Olivine and Plagioclase-Hosted Melt Inclusions and Their Application to Determining Parental Arc Magmas

Abstract approved: Redacted for Privacy

Roger L. Nielsen

Three broadly interrelated problems of critical significance to the proper interpretation of melt inclusion (MI) data are addressed in this thesis. The first issue, the petrogenesis of anorthitic plagioclase phenocrysts in MORB lavas, has relevance due to the presence of numerous MI in many high-An feldspars. This problem was addressed experimentally using basaltic starting compositions saturated with anorthite and forsterite at 1 atm. The resulting liquids were in equilibrium with Al-spinel (Al_2O_3 of 61-68 wt%) at 1290°C and with both $>Fo_{89}$ olivine and $>An_{85}$ feldspar at temperatures of 1230° and 1210°. Melt compositions were similar to natural MORB glasses with Mg#s of 63 to>85. The results suggest that dry, anorthite-bearing basaltic magmas may develop from interaction between primary melt and Al-spinel bearing upper mantle, and consequently MI in natural high-An feldspars may not represent primary magmas.

It has been proposed that the mechanisms of MI formation could modify the entrapped melt composition. This problem was addressed through another experimental series using anorthite/forsterite saturated anhydrous mafic liquids. Charges were cooled from 1300° to 1230° and 1210° C at rates of 1°-10°/min. followed by 0-24 hour isothermal periods. Hopper and skeletal crystal morphologies developed during the cooling period, and planar overgrowth of these textures during isothermal periods formed most inclusions. In general, inclusion compositions were uniform and similar to the host glass, indicating that boundary layers were not entrapped and inclusion formation by this mechanism did not modify entrapped melts.

The third problem addressed the usefulness of MI in identifying primary arc magmas. Melt trapped within olivine phenocrysts in a Mariana arc picrite lava (Mg# ~ 76) were the focus of this study. These had compositions of up to 21.7 wt% MgO, 0.4-0.8 wt% TiO_2, 43.2-47.0 wt% SiO_2, and 1.7-3.4 wt% total alkalis. Major, trace element and volatile data from MI within Fo_{92} olivine indicate that these MI were samples of water-poor primary arc melts. Trace element patterns displayed an arc signature, but at lower total abundances relative to most arc melt inclusions. We propose that the MI do represent primary magmas from both fluxed and decompression melting of the mantle wedge.

Portions of this manuscript have appeared in Geochemistry, Geophysics and Geosystems, Contributions to Mineralogy and Petrology and the Journal of Petrology.

Olivine And Plagioclase-Hosted Melt Inclusions And Their Application to Determining Parental Arc Magmas

by
Edward John Kohut

A THESIS

Submitted to

Oregon State University

in partial fulfillment of
the requirements for the
degree of

Doctor of Philosophy

Presented February 13, 2004
Commencement June 2004

Doctor of Philosophy thesis of Edward J. Kohut
presented on February 13, 2004

APPROVED:

Redacted for Privacy

Major Professor, representing Geology

Redacted for Privacy

Chair of Department of Geosciences

Redacted for Privacy

Dean of Graduate School

I understand that my thesis will become part of the permanent collection of the Oregon State University libraries. My signature below authorizes release of my thesis to any reader upon request.

Redacted for Privacy

Edward J. Kohut, Author

ACKNOWLEDGEMENTS

I wish to express sincere gratitude to Roger Nielsen for serving as advisor and providing continuous academic and financial support. I would like to thank Sherm Bloomer and Bob Stern for involving me with the Mariana project. I also wish to thank Anita Grunder and Andrew Meigs for serving on my committee and providing outstanding courses and field excursions. This research could not have been completed without the assistance of Adam Kent and Paul Wallace in conducting LA-ICP-MS and FTIR analyses and the age data provided by Bob Duncan and John Huard. I also want to thank the reviewers and editors of my submitted papers, notably Bill White, Jim Natland, Tim Grove and Leonid Danyushevsky.

I would also like to thank those friends who kept things interesting throughout the good and the boring in Corvallis, notably Heather and Mike, Chris Krugh, Chris Russo, Erik Klemetti, Mariek Schmidt, Mike Rowe and last but not least Martin Hannigan, even if he is from Northern Ireland.

CONTRIBUTION OF AUTHORS

Dr. Roger Nielsen contributed to all three papers that comprise this thesis and oversaw the experimental work and EMP analyses. He was also P.I. on the grant for the experimental work. Dr. Sherman Bloomer and Dr. Robert Stern were chief scientists for the Cook 7 expedition to the Marianas in the spring of 2001 and served as the P.I.s on the Marianas project. Dr. Adam Kent provided trace element analyses by Laser-ablation ICP-MS and is directing further research on the Mariana Arc. Dr. Matthew Leybourne was a member of the science party for the Cook 7 expedition and conducted the isotopic analyses of the bulk rock samples.

TABLE OF CONTENTS

TABLE OF CONTENTS CONTINUED

LIST OF FIGURES

LIST OF FIGURES CONTINUED

Figure **Page**

LIST OF TABLES

Table **Page**

For Alicia, Nicholaus, Matthew, Christopher and Liam

INTRODUCTION:
OLIVINE AND PLAGIOCLASE-HOSTED MELT INCLUSIONS AND THEIR APPLICATION TO DETERMINING PARENTAL ARC MAGMAS

In this thesis, I address three broadly interrelated problems that have relevance to melt inclusion formation mechanisms, anorthite phase equilibria, and parental arc magmas. In addition to providing potential answers to melt inclusion formation questions, this research will further understanding of the regions and extent of melting in arcs, and their thermal structure. The first two parts involve experimental investigations, the third is an applied study.

The first problem addressed involves the occurrence of anorthitic feldspar (An >90) in anhydrous basaltic magmas and how the phase equilibria affect the utility of anorthite hosted melt inclusions as probes of parent magmas. The An content of feldspar can be increased either by increasing the H_2O content of the magma (Sisson and Grove, 1993) or by raising the Ca/Na or Al of the melt (Panjasawatwong et al., 1995). Although anorthitic feldspars are common in many igneous rocks (e.g. Ribbe, 1976; Marsh et al., 1990; Korenga and Kelemen, 1997), their petrogenesis is not easily explained in anhydrous basaltic magmas. While experimental anhydrous magmas have crystallized equilibrium anorthite, the compositions of these melts did not resemble any naturally occurring basaltic liquid (Panjasawatwong et al., 1995; Nielsen et al., 1995). Knowledge of the phase equilibria of anorthite has implications with regard to the source and degree of melting involved in basalt petrogenesis, and whether or not a specific basalt is truly "primary" or has been modified before eruption. It has been suggested that MORB-like magmas (i.e. those produced by pressure release dry melting of a depleted mantle source) may be a component of some arc lavas (Nye and Reid, 1986; Gribble et al., 1996; Bacon et al., 1997; Sisson and Bronto, 1998). Because of this possibility, the results of this work have bearing on the study of arc, as well as MORB lavas.

The second problem addressed relates to the formation of melt inclusions in olivine and high-An feldspar in anhydrous basaltic liquids. The answers to this problem have significance regarding the utility, application and proper interpretation of data from such inclusions. If melt inclusions in primitive phenocrysts are to be used as probes for sampling parent magmas, then issues related to their formation must be resolved, that is, to what extent do melt inclusions represent the composition of the magmas in which the phenocrysts formed? To answer this question, three things need to be understood: the

mechanisms by which melt is trapped and quenched as glass within a growing crystal, the sources of compositional diversity of inclusion in a single phenocryst, and the effects of post-entrapment crystallization. Some workers (Nakamura and Shimakita, 1998) have suggested that dissolution of the host grain boundary as an inclusion producing mechanism, if so such inclusions would not be in equilibrium with the original melt. My experimental work addressed this issue through observation of the crystallization of feldspar and olivine during various time-temperature paths to determine the cooling conditions required for the creation of melt inclusions in these minerals.

In the third part of this thesis, I present analyses of olivine-hosted melt inclusions from a picrite lava that erupted along the Mariana arc. The origins of magmas in subduction zones is one the most important areas of study in igneous petrology today (Myers and Johnston, 1996; Lee and Stern, 1998; Hirschmann et al., 2000). An understanding of the diversity of parental magma components and their volatile contents across and along a subduction zone is critical to any model of the thermal and physical nature of that subduction system. The compositions of primitive arc melts can constrain, via experimental reproduction, sub-arc mantle temperatures, pressures, and volatile contents in the melting zones (Hirschmann et al., 2000). However, even primitive arc magmas appear to have undergone some mixing and fractionation, and these melts also last equilibrated with the mantle at much lower pressures (~12 kbar) than that presumed for initial primary melting, i.e. 30 kbar (Myers and Johnston, 1996).

Melt inclusion (MI) compositions provide the opportunity for a different approach to addressing this problem. Melt trapped within early formed phenocrysts in primitive basalt lavas are presumed to be samples of the parental liquid for those lavas, and thus would be less modified and closer to the initial melt composition in equilibrium with the mantle.

In the spring of 2001, the Cook 7 expedition dredged a small parasitic volcano situated on the magmatic front NW of Rota in the Marianas. We discovered that a picritic lava from the volcano contained Fo_{89-92} olivines with very primitive (Mg#s to 79.9) melt inclusions. These MI are reasonably similar to the presumed primary melt compositions, and have MgO contents of 16.89-23.19 wt%, 1.34-2.73 wt% total alkalis, <11.33 wt% Al_2O_3, < 0.62 wt% TiO_2, and low amounts of incompatible trace elements

relative to other arc MI. Cl/K ratios are close to the mantle value of 0.04 and H_2O contents are ~0.32 wt%. Significantly, the data show that arc picrites arise from substantial amounts of decompression melting, and this adds to a growing body of evidence that decompression melting plays an important role in arc magmagenesis.

LOW PRESSURE PHASE EQUILIBRIA OF ANHYDROUS ANORTHITE-BEARING MAFIC MAGMAS

Edward J. Kohut
Roger L.Nielsen

This ms published in Geochemistry, Geophysics, Geosystems

www.agu.org/journals/gc/

VOL. 4, NO. 7, 1057, doi:10.1029/2002GC000451, 2003

ABSTRACT

One of the most persistent questions regarding the phase equilibria of mid-ocean ridge basalts (MORB) pertains to the petrogenesis of the anorthitic plagioclase phenocrysts (>An_{90}) that are characteristic of the more primitive members of such suites. Anorthitic phenocrysts are present in many if not most MORB suites in spite of the fact that no naturally occurring MORB glasses have ever been discovered to be in equilibrium with plagioclase more calcic than An_{85}. We have addressed this paradox by attempting to saturate natural basalts with anorthite in a series of 1 atm experiments using three different natural basaltic starting compositions: an N-MORB, an E-MORB, and a continental high-alumina basalt. To ensure duplication of the olivine and anorthite saturation observed in natural anorthite-bearing basalt, the experiments were run in An_{93-6} capsules with Fo_{92} olivine added to the starting glass. The compositions of experimental liquids are generally colinear with the trends observed in the lava suites used as the source material for the starting glasses. Significantly, aluminous spinel (Al_2O_3 contents of 61–68 wt%) was produced at 1290°C in all compositions and chromites (Al_2O_3 contents of 33–42 wt%) at lower temperatures in N-MORB-derived liquids despite no spinel having been added to the starting mixture. In addition, the experiments produced basaltic liquid in equilibrium with both >Fo_{89} olivine and >An_{85} feldspar at temperatures of 1230° and 1210°. These liquids have compositions with Mg# (at% Mg/Mg + Fe^T*100) that range from 63 to >85. The TiO_2-MgO correlation indicates large (~16–23%) amounts of crystallization for each percent decrease in MgO. These results suggest the possibility that dry, anorthite-bearing basaltic magmas are the product of the interaction between primary melt and Al-spinel-bearing upper mantle. In addition, the results indicate that MORB magmas can undergo a large amount (>50%) of crystallization prior to reaching 8% MgO. Further, although anorthite-bearing magmas have characteristics consistent with their being a significant volumetric component of MORB "parent" magmas, the reaction mechanism suggested for their petrogenesis indicates that they are not necessarily primary magmas.

INTRODUCTION

Anorthitic feldspars are present in many mafic rocks, including arc lavas (Marsh et al., 1990; Sisson and Grove, 1993; Danyushevsky et al., 1997), ophiolite sequences (Korenga and Kelemen, 1997), and mid-ocean ridge basalts (MORB) (e.g., Muir and Tilley, 1964; Ribbe, 1983; Natland, 1989; Allan et al., 1989; Nielsen et al., 1995, and references within). Despite their widespread occurrence, the petrogenesis of anhydrous anorthite-bearing basaltic magmas (MORB being the most common example) is not easily explained. It is generally accepted that the An content of feldspar can be increased either by increasing the H_2O content of the magma (Sisson and Grove, 1993) or by raising the Ca/Na or Al of the melt (Fisk, 1984; Panjasawatwong et al., 1995). Increasing pressure decreases the anorthite content of plagioclase at a rate of 1%An/kbar (Fram and Longhi, 1992), suggesting that anorthite phenocrysts in MORB have a shallow depth of origin. This depth has been placed as shallow as <3 kb by Nielsen et al. (1995), while Maclennan et al. (2001) report highAn feldspar that appeared to have formed at 8 kb pressure. While there are a few occurrences of anorthitic feldspar as quench phases in MORB glass (Natland et al., 1983), high-An (>An_{88}) feldspars have never been produced experimentally from any naturally occurring MORB glass under dry conditions. Although synthetic anhydrous magmas have crystallized equilibrium high-An feldspars, the compositions of these melts do not resemble any naturally occurring basaltic lavas (Panjasawatwong et al., 1995; Nielsen et al., 1995).

Most anorthitic feldspars in MORB are not in equilibrium with their host lava (Dungan and Rhodes, 1978; Natland et al., 1983; Sinton et al., 1993). In terms of phase relations, the composition of melt inclusions hosted in MORB high-An crystals, together with the presence of spinel and olivine inclusions indicate that the natural anorthite phenocrysts crystallized in primitive (Mg# up to 75) melts that are three-phase saturated (Nielsen et al., 1995; Sours-Page et al., 2002). Significantly, pyroxene is absent in these lavas. Knowledge of the phase equilibria of high-An feldspar is required in order to investigate the source and degree of melting responsible for the petrogenesis of anorthite-bearing MORBs. It is also needed to determine whether or not parent magmas of these

MORBs are primary in the sense of being an unmodified product of partial melting, or have been modified by reaction with the upper mantle and crust before eruption.

The petrogenesis of anorthite phenocrysts in MORB lavas has added significance in that they commonly contain large numbers of melt inclusions (Sinton et al., 1993; Nielsen et al., 1995). In order to interpret the composition of melt trapped in anorthite, it is necessary to establish whether the anorthite phenocrysts are crystallization products of primary melting of a high-Ca/Na_2O (refractory) source, primary melting of a high-Al source, or products of reaction between primitive melts and the mantle or crust. If either of the first two cases is valid for anorthite formation, then the crystals may potentially trap primary melt. If the last case is valid, then the melt trapped by anorthite may be primitive and parental to more evolved lavas, but not technically primary.

Some melt inclusion compositions suggest that high-An feldspar-bearing MORBs originate from refractory melts, i.e., those with low Na and Ti contents (Natland, 1989; Johnson et al., 1995). However, other examples of melt inclusion data from high-An feldspars in MORB are not simultaneously low in Na and Ti (Nielsen et al., 1995; Sours-Page et al., 1999, 2002). In addition, Sours-Page et al. (2002) report that compositions of plagioclase-hosted melt inclusions from the East Pacific Rise are more evolved than inclusions in coexisting olivine phenocrysts. The compositions of the feldspar-hosted inclusions overlap those of the more primitive olivine-hosted inclusions and more evolved host lava, indicating that the feldspar crystallized in a melt that was not primary, yet was parental to the erupted lava. Although many feldspar hosted melt-inclusions show compositional diversity that may be evidence for magma mixing between refractory and nonrefractory melts, the data of Sours-Page et al. (2002) reflect a more homogenous, nondepleted parent magma.

In addition, derivation of data from anorthite hosted melt inclusions have several advantages over olivine hosted melt inclusions. First is the slow rate of diffusion of major elements compared to olivine (Grove et al., 1984), which limits the potential modification by re-equilibration with the host magma, such as that observed in olivine-hosted inclusions (Gaetani and Watson, 2000). The depth of entrapment is also constrained by the pressure limitations of anorthite formation noted above. In contrast, because basaltic

magmas are saturated with respect to forsteritic olivine at all pressures (Elthon, 1989), we have no constraints on pressure from olivine hosted melt inclusions unless we obtain CO_2 measurements on the inclusions (Cervantes and Wallace, 2000). Even in that case, we must assume that the pressure estimates based on CO_2 are maximum values. Anorthite hosted melt inclusions then provide a means of sampling melts assumed to be from depths <10 km. In any case, an understanding of the phase equilibria of high-An plagioclase-bearing melts is critical to interpretation of those melt inclusions.

In this paper, we describe an experimental investigation of the question regarding the composition of basaltic liquids in equilibrium with high-An feldspar. This study is particularly relevant to the petrogenesis of those large, high-An (>85) feldspar phenocrysts present in many MORB lavas (Sinton et al., 1993; Nielsen et al., 1995; Sours-Page et al., 1999). Because it has been suggested that dry basaltic melts may be present in arcs (e.g., Nye and Reid, 1986; Sisson and Bronto, 1998), this study is also relevant to the petrogenesis of plagioclase-bearing arc basalts. We designed the experiments to produce an anhydrous, primitive (Mg# of 70–75) basaltic liquid that would crystallize $An_{>80}$ feldspars as an equilibrium phase. Ideally, one would start with naturally occurring glasses for this purpose, but basaltic glasses in equilibrium with high-An feldspar do not exist outside of melt inclusions. Instead, we chose to use natural basaltic glass and modify it by adding anorthitic components. This was achieved by melting the glass at high temperature while in contact within an anorthite capsule. The use of a feldspar capsule has several advantages over the typical procedure of doping glass with the desired component (in this case anorthite) and running in platinum crucibles. One is that the large crystal/melt ratio allows multiphase saturation without significantly affecting the average composition of feldspar that form as an equilibrium phase at run temperatures, and the capsule bulk reduces Na loss to furnace atmosphere. In addition, since the Pt suspension wire is in contact only with the capsule, Fe loss from the liquid is greatly reduced. We must emphasize that these experiments were not designed to model a natural process where basaltic magma reacts with plagioclase, nor should our results be interpreted in this context. The basaltic starting materials we used are not meant to represent a specific location or tectonic setting, but rather simulate three primitive basaltic magmas types of varying enrichment that are normally considered to be

derived from dry decompression melting. These experiments used run temperatures ranging from 1200° to 1290°C.

METHODS

Experimental Methods

To fabricate experimental capsules, we used phenocrysts of An_{93-6} plagioclase from Arenal Volcano, Costa Rica. The megacrysts were cut into ~5mm cubes and a hole ~2 mm in diameter and 3 mm deep was drilled into each capsule to hold the starting powder. The capsules were visually inspected to ensure that they did not have any glass from the feldspars' host lava. The starting powders consisted of ground glass from N-MORB, E-MORB, and continental high-alumina basalt (HAB). E-MORB starting materials were the least primitive, with Mg# averaging 59.98 and HAB materials were the most primitive (Table 1). HAB materials are also the lowest $CaO/NaO_2 = 3.79$ and were the most enriched, with a K_2O/TiO_2 ratio of 0.81 (Table 1). N-MORB starting glass was the least enriched and most refractory ($K_2O/TiO_2 = 0.04$, $CaO/NaO_2 = 5.6$; Table 1). However, it must be noted that these were the compositions of the glasses before being saturated in anorthite.

The N-MORB was sampled from Gorda Ridge lava (D9-2 -Davis and Clague, 1987), the E-MORB from the Endeavour segment of the Juan de Fuca Ridge (E-32-Karsten et al., 1990), and the high-alumina basalt from Medicine Lake in California (Giant Crater -Baker et al., 1991; Donnelly-Nolan et al., 1991). Kilbourne Hole olivine (Fo_{91-92}) was added to ensure olivine saturation. The rationale behind using whole olivine crystals is the same as that for using anorthite capsules, i.e., the bulk ensures allows multiphase saturation without significantly affecting the average composition of the olivine that form at equilibration run temperatures. In addition, 0.1 wt% ZrO_2 was added to distinguish the products of our experiments from any small amount of glass that may have escaped visual inspection of the capsule material. This was done in the event that any of our experimental glass flowed into cracks in the capsules, which had occurred in earlier experiments using feldspar capsules from a different source. In such circumstances, it would be necessary to distinguish, via the ZrO_2 dopant, the

TABLE 1: Starting Materials and EMP Error

Starting Materials

Glasses

	N-MORB		E-MORB		HAB	
	Avg	2σ	Avg	2σ	Avg	2σ
SiO_2	50.22	0.25	50.32	0.26	51.47	0.15
TiO_2	1.22	0.03	1.87	0.04	0.93	0.03
Al_2O_3	15.4	0.07	15.75	0.11	17.14	0.07
Cr_2O_3	0.03	0.02	0.05	0.02	0.02	0.01
FeO*	9.28	0.06	9.21	0.09	7.26	0.36
MnO	0.15	0.03	0.16	0.03	0.15	0.03
MgO	8.54	0.05	7.43	0.05	7.88	0.17
CaO	12.26	0.11	11.82	0.11	10.49	0.19
Na_2O	2.19	0.04	2.73	0.04	2.77	0.06
K_2O	0.05	0.01	0.59	0.01	0.75	0.02
P_2O_5	0.11	0.03	0.27	0.02	0.16	0.02
total	99.45		100.2		99.02	
n	35		20		20	
Mg#	62.11		59.98	0.31	65.93	1.54
CaO/Na_2O	5.6		4.53		3.79	
K_2O/TiO_2	0.04		0.32		0.81	

Capsule

	Arenal Feldspar	
	Avg	2σ
SiO_2	43.61	0.81
Al_2O_3	35.44	0.65
FeO*	0.44	0.05
MgO	0.06	0.05
CaO	19.32	0.47
Na_2O	0.47	0.19
K_2O	0.01	0.01
total	99.35	
n	61	
An	95.75	1.663

EMP Accuracy and Precision

	Glass Analysis		Feldspar Analysis		Olivine Analysis		Spinel Analysis	
	± error	2σ	± error	2σ	± error	2σ	± error	2σ
SiO_2	0.8%	0.08	0.6%	0.20	1.3%	0.07		
TiO_2	3.1%	0.04						
Al_2O_3	1.0%	0.07	0.5%	0.04			0.6%	0.02
FeO*	12.9%	0.12			0.2%	0.10	5.0%	0.13
MgO	2.3%	0.04			0.9%	0.07	7.0%	0.04
CaO	1.1%	0.08	1.5%	0.05				
Na_2O	2.7%	0.04	2.6%	0.04				
Cr_2O_3	-		-				1.1%	0.08

Maximum error reported for significant elements of each analyses routine

± error calculated for each analysis routine by [(measured)-true/measured]*100

Precision reported as 2σ

experimental glass from any natural glass in the cracks. However, with Arenal feldspar capsules the experimental liquids remained confined to the hole drilled into the capsule.

The charges were suspended by platinum wire in a Deltec vertical quench furnace and the oxygen fugacity was set at the QFM buffer using a mixture of CO_2 and H_2. An initial run temperature of 1300°C for two hours was used to saturate the melt in anorthite and olivine, this temperature will be referred to as the initial melting temperature. Re-

homogenization experiments of plagioclase-hosted melt inclusions (Johnson et al., 1995; Sinton et al., 1993; Nielsen et al., 1995; Sours-Page et al., 1999) show that most entrapment temperatures in MORB are below 1260°–1280°. Since this suggests that many high-An feldspar in MORB were crystallize at or below these temperatures, we selected 1300° as the point at which we saturate the melt in anorthitic components (i.e., raise the Al and Ca/Na levels). One experiment for each starting material was held at the melting temperature for 6 hours, then quenched. The purpose for this experiment was to observe the composition of the saturated melt prior to being lowered to the equilibration temperatures. Otherwise, after the initial heating to 1300°C, the experimental charge was dropped to run temperature for 24 hours; we will refer to this temperature as the equilibration temperature. At the end of the run time, the charges were drop-quenched in water.

The first set of experiments was done using only N-MORB glass (no forsterite) in anorthite capsules to provide baseline data melts saturated with feldspar only. This is similar to the approach used by Panjasawatwong et al. (1995). The second set of experiments added whole forsterite crystals to the glass and ran at equilibration temperatures of 1290°, 1260°, 1230°, and 1210° C. A single experiment run for two hours at 1300° showed no significant difference compared to the 6-hour run. The experiments in second set successfully produced mafic liquids that crystallized anorthite and forsterite at 1230°, and 1210° C. We then repeated these experiments using E-MORB and HAB starting powders.

To test the effects of changing the initial melting temperature and the degree of undercooling (ΔT = initial T-equilibration T), we conducted a third set of experiments. In these, the run temperature was fixed at 1210° C, which was found from the results of the second experimental set to be favorable for high-An feldspar crystallization. Initial melting temperatures of 1280°, 1250°, and 1220° C were used to reproduce the same amounts of undercooling as those in the second set of experiments. These experiments were run using only the N-MORB starting glass.

Analytical Methods

Run products were analyzed with the Cameca SX-50 electron microprobe at Oregon State University using a 15 kV, 30nA, 3 micron diameter beam for glass and feldspar, and 15 kV, 50 nA, 1 micron diameter beam for olivine. For glass, count times were 30s for Fe, 20s for Mg, Al, Si, P, K, Ti and Zr, and 10s for Na, Ca, Cr, and Mn. For feldspar, count times were 10 seconds for all elements. For olivine, count times were 20s for Fe, Si, and Ni, and 10s for Mg, Al, Si, K, Ti, Na, Ca, Cr, and Mn. To minimize the effects of Na migration, Na was analyzed first. Precision and accuracy measurements for the most significant elements in the glass, feldspar, olivine and spinel analyses routines are listed in Table 1.

RESULTS

Experiment Set 1: Anorthite Saturated Melt

The first experiments using N-MORB glass saturated with anorthite only (without added forsterite) produced $An_{76.9–79.7}$ feldspar at temperatures 1230° and 1200°. Feldspar only crystallized at temperatures below 1250° and feldspar compositions were never higher than $An_{79.7}$, although the composition of the reaction zone on the capsule rim was $An_{84.3}$ at 1250° equilibration temperature and $An_{92.7}$ at the 1300° melting temperature (Table 2, Figure 1). Predicted values for An content were calculated using equation (1) of Panjasawatwong et al. (1995) and the Ca# and An# of our experimental melts. Except for the 1230° run, neither the An content of the experimentally produced feldspars nor the reaction zones on the capsules were similar to the predicted values. While the An content of the feldspars and the MgO of the host liquid at 1200° and 1230° were similar to An content of some feldspars and their host glass reported by Natland (1989, Tables 1 and 5), the Al contents of the experimental liquids were higher. The liquids had Mg# (atomic% $Mg/Mg + Fe_T*100$) of 62.4–67.5, 1.7–2.31 wt% Na_2O and 15.43–19.73 wt% Al_2O_3

TABLE 2: Summary of Experimental Results

Experiment Set 1: Anorthite Saturated

N-MORB Starting Material, 1300° C Melting Temp.

Equilibration Temp (°C)	Glass Mg#	Glass Ca#	Glass Al#	Capsule Rim An	Feldspar An
1200	67.5	49.1	28.8	84.3	77.6
1230	65.6	75.8	26.9	87.7	79.7
1250	67.5	68.1	28.1	84.3	none
1300	67.1	70.4	31.0	92.7	none

Experiment Set 2: Anorthite and Forsterite Saturated

N-MORB Starting Material, 1300° C Melting Temp.

Equilibration Temp (°C)	Glass Mg#	Glass Ca#	Glass Al#	Capsule Rim An	Feldspar An	Added Ol Rim Fo	Olivine Fo	Spinel Cr#
1210	69.4	81.8	27.0	85.4	84.1	none	89.0	0.34
1230	69.7	84.2	27.8	88.2	87.0	none	90.2	0.38
1260	76.9	89.8	29.9	92.7	none	none	92.2	0.31
1290	82.0	88.3	33.7	95.4	none	92.2	none	0.03
*1290	82.2	89.9	34.5	95.3	none	91.7	none	0.05
1300	83.4	94.1	31.7	95.2	none	90.9	none	none

*4 hour equilibration time

E-MORB Starting Material, 1300° C Melting Temp.

Equilibration Temp (°C)	Glass Mg#	Glass Ca#	Glass Al#	Capsule Rim An	Feldspar An	Added Ol Rim Fo	Olivine Fo	Spinel Cr#
1210	63.2	81.3	27.2	87.2	86.1	none	86.7	none
1230	67.3	82.0	29.0	87.2	86.6	none	89.4	none
1260	81.3	83.7	31.7	92.3	none	none	93.7	none
1290	83.5	87.0	34.0	95.4	none	91.0	none	0.01
1300	85.4	87.7	30.8	95.1	none	none	none	none

HAB Starting Material, 1300° C Melting Temp.

Equilibration Temp (°C)	Glass Mg#	Glass Ca#	Glass Al#	Capsule Rim An	Feldspar An	Added Ol Rim Fo	Olivine Fo	Spinel Cr#
1210	63.2	81.2	27.2	84.9	81.5	none	86.9	none
1230	65.9	86.0	28.9	87.6	85.6	none	88.8	0.01
1260	76.2	82.6	32.1	90.4	none	none	none	none
1290	79.0	82.7	33.5	94.8	none	91.4	none	0.01
1300	84.4	90.8	35.3	95.6	none	none	none	none

Experiment Set 3: Variable Melting Temperatures

N-MORB Starting Material, 1210° C Equilibration Temp.

Melting Temp (°C)	Glass Mg#	Glass Ca#	Glass Al#	Capsule Rim An	Feldspar An	Added Ol Rim Fo	Olivine Fo	Spinel Cr#
1220	66.9	82.2	25.8	95.6	95.5	none	87.8	0.37
1250	67.4	83.8	25.5	92.3	92.8	none	88.7	0.38
1280	69.4	84.3	25.9	88.3	88.5	none	88.9	0.38

Mg#=at% Mg/(Mg+Fe^T)*100, Ca#=at% Ca/(Ca+Na)*100, Al#=at% Al/(Al+Si)*100

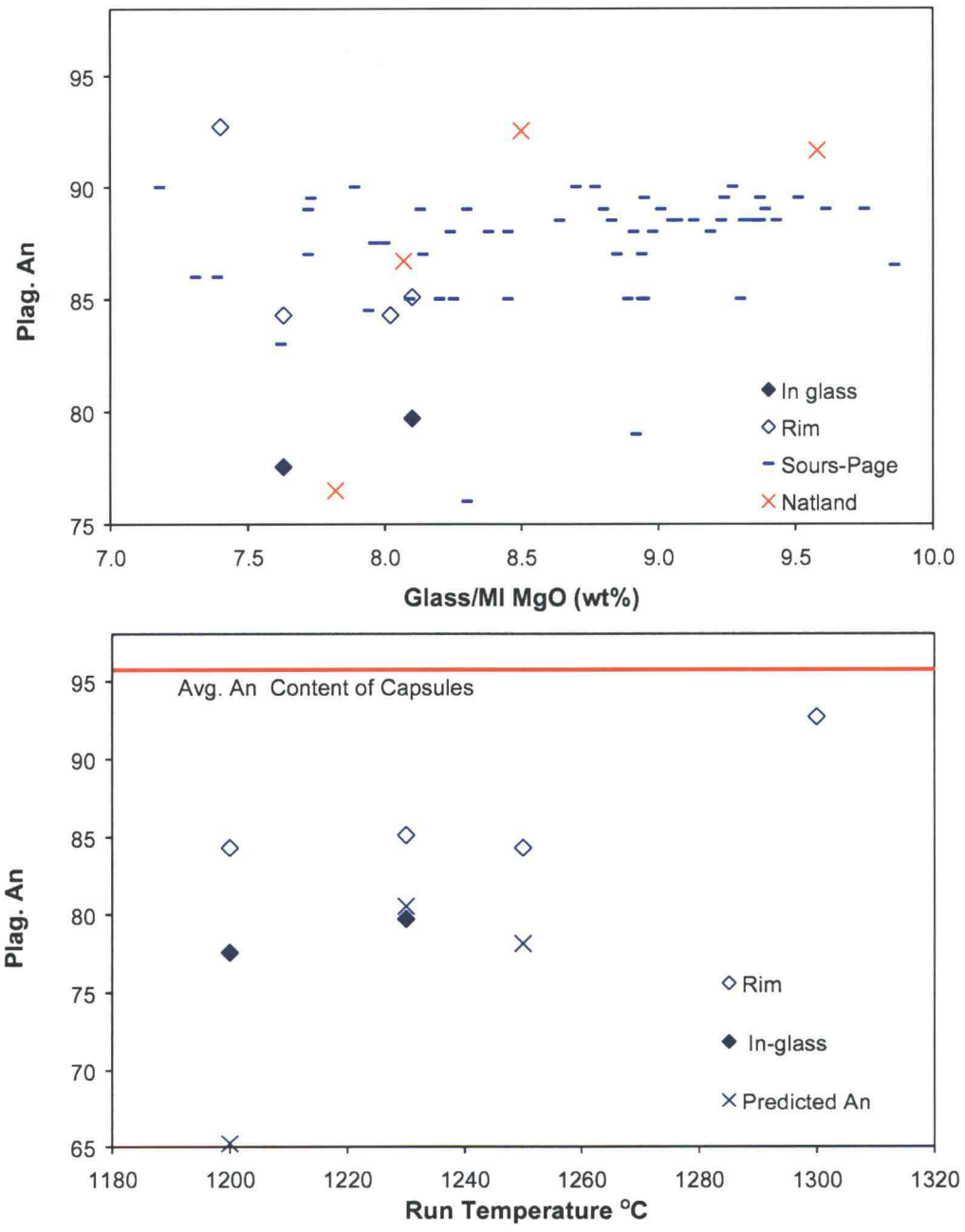

Figure 1

Figure 1-top: An content of feldspars from experiment set 1 vs MgO of host liquid. "Sours-Page" refers to host feldspar An and melt inclusion MgO from Sours-Page et al. (1999, 2002) and "Natland" refers to feldspar An and host glass MgO from Natland (1989). "Rim" refers to capsule rim reaction zone, "In-glass" are feldspars that crystallized within the melt.

-bottom: An content of feldspars and capsule reaction zones from experiment set 1 vs. equilibration temperatures. "Predicted" are the An values of feldspar predicted for the melt composition.

(Figure 2, Tables 2 and 3). No examples of MORB glass in the precompiled RIDGE petrologic database (available at http://petdb.ldeo.columbia.edu/readydata/MAR55S-52N_major_probe.csv) (hereinafter referred to as RIDGE PETDB) had Al_2O_3 as high as the glasses for these experiments and TiO_2 contents were lower than any glass in the database with MgO contents similar to the experimental liquids (Table 2, Figure 2). The glass compositions were similar to some of the refractory melt inclusions reported by Johnson et al. (1995), but the host feldspars in reported in that paper had higher An contents than our experimental feldspars. The major element contents of liquids for these experiments were similar to those of the Panjasawatwong et al. (1995) that produced plagioclase only, except that our glasses had higher Mg# and ~1–3 wt% higher MgO contents.

Experiment Set 2: Anorthite and Forsterite Saturated Melt

In the second set of experiments, we added whole olivine crystals to drive the melt to saturation with forsterite as well as anorthite components at high temperature (>1260°). As a result, the lower temperature experiments had melts that nucleated both feldspar and olivine. In addition, Al-rich spinel was present in the 1290° runs in this set of experiments, indicating that at higher temperatures the melt was in equilibrium with this third phase.

The Mg# of liquids decreased from 83.4 at 1300° to 69.4 at 1210° for N-MORB, from 85.4 to 63.2 for E-MORB, and 84.4 to 63.2 for HAB starting compositions (Table 2). At 1260°, the Mg# of glasses approximate those of hypothetical MORB parent magmas (assumed to be in equilibrium with mantle olivine), which range from 70 to 77 (Basaltic Volcanism Study Project (BVSP), 1981). At 1260°, the N-MORB-derived liquids Mg# averaged 76.9, E-MORB-derived Mg# were 81.3, and HAB-derived Mg# were 76.2 (Table 2), and the melts were in equilibrium with high-Fo olivine, as indicated by the presence of this phase in the run products. The glass compositions at 1230° were similar to natural, primitive basalts: the N-MORB-, E-MORB-, and HAB-derived melts have average Mg# of 69.7, 67.3, and 65.9 respectively (Table 2). Furthermore, the presence of high-An feldspar and high-Fo olivine indicates that the melts were in equilibrium with these phases at this temperature.

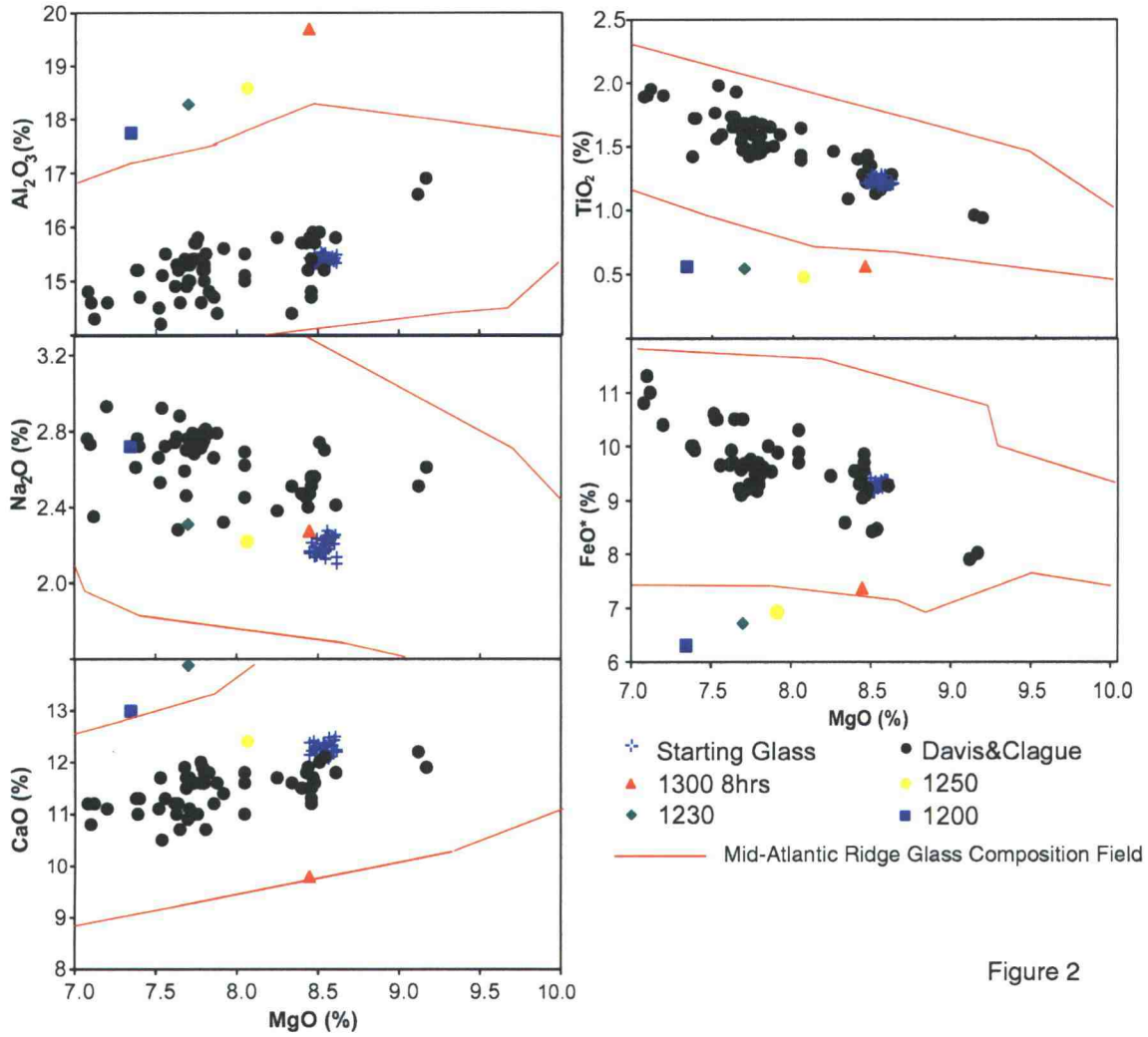

Figure 2: Al_2O_3, Na_2O, CaO, TiO_2 and FeO*, vs MgO of glasses for experiment set 1. Numbers refer to equilibration temperatures. Run times were 18 hrs except were noted. "Davis and Clague" refers to compositions from the Gorda Ridge in Davis and Clague (1987). Region outlined in red contains range of Mid-Atlantic Ridge glass compositions in the pre-compiled RIDGE petrologic database (RIDGE PETDB).

At all temperatures, the rims of the anorthite capsules adjacent to the liquids contained a reaction zone and the An content of these reaction rims decreased with run temperature (Figure 3). A reaction rim of ~10 μm was present at the capsule/glass interface for N-MORB and HAB starting materials at 1300°. This rim was $An_{92.6}$ for N-MORB and $An_{94.8}$ for HAB, while the rim in the E-MORB experiments was unchanged from the starting capsule composition (Table 2). At temperatures of 1230° and below the reaction zone included new overgrowth. This was also the highest temperature at which

plagioclase nucleated in the liquid. The An value of the reaction rims and liquid MgO at 1260° were similar to host feldspar An and melt inclusion MgO reported by Sours-Page et al. (1999, 2002), and somewhat similar to those of inclusions and feldspars in Natland (1989) (Figure 3). At 1230°, N-MORB-derived liquids crystallized An_{87} feldspar, E-MORB liquids produced $An_{86.6}$ feldspar, while HAB-derived liquids produced $An_{85.6}$ feldspar (Tables 2 and 4, Figure 3). The An contents of the feldspars at low temperatures and the reaction rims at higher temperatures were generally in good agreement with the values predicted using Panjasawatwong et al. (1995, equation (1)) (Figure 3). The An contents of the feldspars at 1230° and 1210° and the MgO values of the liquids they formed in were also similar to those of feldspars and their melt inclusions reported by Sours-Page et al. (1999, 2002).

New olivine nucleated in liquids from all starting compositions at temperatures of 1260° C and below. Remnants of the Kilbourne Hole forsterite added to the starting glass were present in all 1290° melts of experiment set 2, and at 1210° as well for the HAB composition. The compositions of olivines that crystallized in the liquids were consistently greater than Fo_{86} (Tables 2 and 5). The olivines produced at 1230° in N-MORB-, E-MORB-, and HAB-derived melts were $Fo_{90.2}$, $Fo_{89.4}$, and $Fo_{88.8}$ respectively. Equilibrium FeO/MgO ratios of olivines were predicted using Roeder and Emslie's (1970) FeO/MgO melt-solid partitioning coefficient of 0.3. Overall, the FeO/MgO ratios of olivines produced during experiments with E-MORB-derived liquids were closer to the values predicted than those in N-MORB- and HAB-derived liquids (Figure 4). At 1230°, olivines in both the N-MORB- and HAB-derived melts were further from equilibrium compared to the 1210° experiments.

In experiments run at 1290°, Al-spinel crystallized in the liquid adjacent to the capsule wall (Figure 5). At this temperature, the spinels in the N-MORB liquids had Al_2O_3 contents of 57-67.8 wt% and Cr# (Cr/Cr+Al) of 0.02–0.11 (Table 6). Those in the E-MORB liquids had an average Al_2O_3 content of 68.35 wt% and Cr# of 0.01 and those in HAB liquids had an average Al_2O_3 content of 67.21 wt% and Cr# of 0.01 (Table 6). The formations of Al-spinels in bands suggests the presence of a compositional gradient in the melt, but none was observed in EMP traverses across the glass, even in the

TABLE 3: Glass Analyses

Experiment Set 1: Anorthite Saturated

N-MORB Starting Material, 1300° C Melting Temp.

	1300° Melt T.		1250° Equil. T.		1230° Equil. T.		1200° Equil. T.	
	Avg	2σ	Avg	2σ	Avg	2σ	Avg	2σ
SiO_2	51.77	0.11	50.65	0.44	50.10	0.55	51.71	0.03
TiO_2	0.56	0.03	0.48	0.02	0.54	0.05	0.56	0.05
Al_2O_3	19.7	0.12	18.58	0.10	18.28	0.09	17.74	0.09
Cr_2O_3	0.02	0.02	0.01	0.02	0.03	0.02	0.03	0.02
FeO*	7.37	0.02	6.91	0.09	6.71	0.20	6.30	0.04
MnO	0.19	0.05	0.20	0.03	0.20	0.02	0.08	0.04
MgO	8.45	0.07	8.07	0.07	7.70	0.19	7.35	0.05
CaO	9.8	0.09	12.40	0.48	13.87	0.33	12.98	0.13
Na_2O	2.27	0.05	2.22	0.03	2.31	0.10	2.72	0.03
K_2O	0.07	0.01	0.09	0.01	0.06	0.04	0.07	0.04
P_2O_5	0.09	0.02	0.07	0.01	0.08	0.04	0.08	0.02
total	100.3		99.68		99.88		99.62	
n	10		10		5		10	
Ca/Na	4.32		5.59		6.00		4.77	
K/Ti	0.13		0.19		0.11		0.13	

Experiment Set 2: Anorthite and Forsterite Saturated

N-MORB Starting Material, 1300° C Melting Temp.

1300° Equil. T.		1290° Equil. T.		*1290° Equil. T.		1260° Equil. T.	
Avg	2σ	Avg	2σ	Avg	2σ	Avg	2σ
46.83	0.12	46.79	0.20	47	0.28	48.97	0.12
0.38	0.01	0.46	0.01	0.41	0.06	0.75	0.01
20.91	0.24	20.16	0.20	20.55	0.65	17.75	0.09
0.03	0.02	0.02	0.02	0.03	0.02	0.07	0.02
4.77	0.04	5.45	0.10	5.16	0.18	6.41	0.08
0.09	0.02	0.09	0.03	0.09	0.02	0.15	0.02
13.41	0.29	13.25	0.22	13.21	0.48	11.92	0.07
13.76	0.13	13.93	0.31	13.82	0.24	13.87	0.11
0.85	0.02	0.88	0.04	0.99	0.04	0.88	0.04
0.02	0.01	0.05	0.01	0.03	0.01	0.07	0.01
0.04	0.02	0.08	0.02	0.04	0.02	0.09	0.03
101.1		101.2		101.3		100.9	
5		15		31		16	

*Experiment with 4 hour run time

16.19		15.83		13.96		15.76	
0.05		0.11		0.07		0.09	

TABLE 3:continued

	E-MORB Starting Material, 1300° C Melting Temp.										HAB Starting Material	
	1230° Equil. T.		1210° Equil. T.		1300° Equil. T.		1290° Equil. T.		1260° Equil. T.		1230° Equil. T.		1210° Equil. T.		1300° Equil. T.	
	Avg	2σ	Avg	2σ	Avg	2σ	Avg	2σ	Avg	2σ	Avg	2σ	Avg	2σ	Avg	2σ
SiO_2	49.32	0.15	50.91	0.14	46.56	0.18	47.31	0.18	48.11	0.43	48.11	0.39	48.69	0.35	46.44	0.53
TiO_2	0.94	0.03	1.09	0.02	0.73	0.05	0.80	0.02	1.14	0.03	1.62	0.03	1.90	0.05	0.28	0.02
Al_2O_3	16.18	0.08	15.00	0.25	20.64	0.37	20.71	0.16	18.94	0.10	16.67	0.06	15.41	0.11	21.65	0.15
Cr_2O_3	0.08	0.02	0.11	0.04	0.02	0.03	0.02	0.03	0.02	0.02	0.03	0.02	0.03	0.03	0.01	0.02
FeO*	7.92	0.10	7.98	0.02	4.55	0.20	4.72	0.08	4.79	0.06	8.43	0.05	9.24	0.10	4.39	0.10
MnO	0.16	0.03	0.17	0.04	0.11	0.03	0.11	0.01	0.12	0.03	0.15	0.03	0.17	0.03	0.08	0.02
MgO	10.24	0.08	9.76	0.06	13.58	0.22	13.02	0.07	11.7	0.09	9.72	0.08	8.89	0.10	13.34	0.17
CaO	14.09	0.22	14.02	0.21	13.2	0.14	12.76	0.09	12.15	0.12	12.39	0.08	12.94	0.36	13.29	0.12
Na_2O	1.42	0.05	1.40	0.04	0.98	0.05	1.06	0.05	1.30	0.04	1.50	0.05	1.64	0.04	0.76	0.03
K_2O	0.08	0.01	0.08	0.01	0.25	0.01	0.21	0.01	0.31	0.01	0.45	0.01	0.47	0.02	0.15	0.01
P_2O_5	0.09	0.03	0.11	0.02	0.18	0.03	0.08	0.01	0.15	0.02	0.22	0.03	0.25	0.03	0.05	0.02
total	100.5		100.6		100.8		100.8		98.73		99.29		99.63		100.4	
n	22		8		15		6		21		12		13		18	
	9.92		10.01		13.47		12.04		9.35		8.26		7.89		17.49	
	0.09		0.07		0.34		0.26		0.27		0.28		0.25		0.54	

TABLE 4: Feldspar Analyses

Experiment Set 1: Anorthite Saturated

N-MORB Starting Material, 1300° C Melting T

	1230° Equil. T.		1200° Equil. T.	
	Avg	2σ	Avg	2σ
SiO_2	48.69	0.00	49.49	0.01
Al_2O_3	32.03	0.01	31.56	0.10
FeO*	0.50	0.00	0.62	0.18
MgO	0.23	0.02	0.63	0.25
K_2O	0.06	0.01	0.03	0.01
CaO	15.63	0.07	15.29	0.00
Na_2O	2.21	0.02	2.45	0.23
Total	99.34		97.62	
n	3		2	
An	79.74	0.19	77.55	1.87

Experiment Set 2: Anorthite and Forsterite Saturated

N-MORB Starting material

	1230° Equil. T.		1210° Equil. T.	
	Avg	2σ	Avg	2σ
SiO_2	46.81	0.42	48.12	0.55
Al_2O_3	33.82	0.22	32.99	0.39
FeO*	0.45	0.08	0.44	0.00
MgO	0.35	0.03	0.44	0.05
K_2O	0.01	0.01	0.06	0.01
CaO	17.78	0.17	16.4	0.13
Na_2O	1.47	0.07	1.72	0.23
Total	99.22		98.45	
n	12		5	
An	86.95	0.59	84.05	1.91

E-MORB Starting material

	1230° Equil. T.		1210° Equil. T.	
	Avg	2σ	Avg	2σ
SiO_2	46.49	0.30	45.54	0.35
Al_2O_3	33.34	0.42	32.81	0.87
FeO*	0.48	0.20	0.61	0.35
MgO	0.38	0.25	0.48	0.32
K_2O	0.08	0.02	0.08	0.02
CaO	17.28	0.13	17.03	0.35
Na_2O	1.48	0.09	1.52	0.15
Total	98.05		96.55	
n	10		10	
An	86.55	0.80	86.07	1.45

Experiment Set 2: continued

HAB Starting material

	1230° Equil. T.		1210° Equil. T.	
	Avg	2σ	Avg	2σ
SiO_2	47.16	0.47	47.68	0.50
Al_2O_3	33.47	0.47	32.36	0.27
FeO*	0.50	0.11	0.54	0.08
MgO	0.34	0.15	0.40	0.04
K_2O	0.09	0.02	0.13	0.02
CaO	17.39	0.37	16.19	0.25
Na_2O	1.62	0.18	2.03	0.13
Total	98.95		97.3	
n	7		8	
An	85.61	1.59	81.53	1.12

Experiment Set 3: Anorthite and ForsteriteSaturated Variable Melting Temperatures

N-MORB Starting Material, 1210° C Equilibration Temp.

	1280° Melt T.		1250° Melt T.		1220° Melt T.	
	Avg	2σ	Avg	2σ	Avg	2σ
SiO_2	46.25	1.77	42.35	2.92	43.53	0.41
Al_2O_3	33.51	1.59	36.14	2.54	35.33	0.40
FeO*	0.52	0.16	1.124	0.06	0.48	0.06
MgO	0.35	0.24	0.05	0.03	0.09	0.12
K_2O	0.01	0.01	0.00	0.01	0.01	0.01
CaO	18.05	1.19	19.21	1.12	19.3	0.23
Na_2O	1.29	0.63	0.93	0.07	0.5	0.10
Total	98.69		98.87		98.74	
n	28		17		23	
An	88.51	5.62	92.88	0.93	95.55	0.86

TABLE 5: Olivine Analyses

Experiment Set 2: Anorthite and Forsterite Saturated

N-MORB Starting Material, 1300° C Melting Temp.

	1260° Equil. T.		1230° Equil. T.		1210° Equil. T.	
	Avg	2σ	Avg	2σ	Avg	2σ
SiO_2	40.3	0.35	39.74	0.30	40.31	0.31
TiO_2	0.00	0.00	0.01	0.01	0.05	0.04
Al_2O_3	0.09	0.03	0.11	0.07	0.60	0.79
Cr	0.04	0.03	-	-	0.04	0.02
FeO*	7.6	0.43	9.50	0.45	10.55	0.10
MnO	0.09	0.02	0.14	0.01	0.18	0.01
MgO	50.13	0.55	48.85	0.38	47.69	1.11
NiO	0.35	0.05	0.32	0.04	0.22	0.01
CaO	0.31	0.09	0.40	0.03	0.90	0.58
Na_2O	0.01	0.01	0.01	0.01	0.03	0.06
Total	98.92		99.08		100.6	
n	18		16		5	
Fo	92.16	0.47	90.16	0.46	88.96	0.17

E-MORB Starting Material, 1300° C Melting Temp.

	1260° Equil. T.		1230° Equil. T.		1210° Equil. T.	
	Avg	2σ	Avg	2σ	Avg	2σ
SiO_2	40.77	0.37	39.91	0.10	40.4	0.40
TiO_2	0.02	0.01	0.04	0.01	0.02	0.01
Al_2O_3	0.18	0.15	0.09	0.02	0.06	0.04
Cr	0.03	0.02	0.02	0.01	0.02	0.01
FeO*	6.13	0.27	11.38	0.17	10.13	1.32
MnO	0.11	0.02	0.19	0.02	0.15	0.03
MgO	51.33	0.47	47.3	0.18	48.69	1.30
NiO	0.17	0.08	0.25	0.01	0.32	0.05
CaO	0.27	0.07	0.32	0.03	0.22	0.20
Na_2O	0.01	0.01	0.00	0.00	0.01	0.01
Total	99.03		99.51		100	
n	15		8		5	
Fo	93.7		89.4		86.7	

HAB Starting Material, 1300° C Melting T

	1230° Equil. T.		1210° Equil. T.	
	Avg	2σ	Avg	2σ
SiO_2	40.07	0.31	40	0.40
TiO_2	0.00	0.01	0.02	0.01
Al_2O_3	0.09	0.03	0.07	0.04
Cr	0.02	0.02	0.03	0.01
FeO*	10.84	0.91	12.23	2.19
MnO	0.16	0.02	0.19	0.05
MgO	48.18	0.77	47.56	1.82
NiO	0.31	0.06	0.31	0.04
CaO	0.25	0.06	0.28	0.15
Na_2O	0.01	0.01	0.02	0.02
Total	99.92		100.6	
n	10		7	
Fo	88.79	0.99	86.93	2.37

Experiment Set 3: Anorthite and ForsteriteSaturated Variable Melting Temperatures

N-MORB Starting Material, 1210° C Equilibration Temp.

	1280° Melt T.		1250° Melt T.		1220° Melt T.	
	Avg	2σ	Avg	2σ	Avg	2σ
SiO_2	39.00	0.24	39.33	0.24	39.34	0.26
TiO_2	0.01	0.01	0.02	0.01	0.02	0.00
Al_2O_3	0.22	0.52	0.07	0.01	0.09	0.01
Cr	0.08	0.02	0.06	0.03	0.10	0.04
FeO*	10.65	0.39	10.89	0.10	11.13	0.13
MnO	0.17	0.01	0.15	0.01	0.15	0.02
MgO	47.63	0.23	47.73	0.40	46.96	0.43
NiO	0.19	0.05	0.24	0.01	0.19	0.01
CaO	0.45	0.16	0.42	0.01	0.44	0.02
Na_2O	0.01	0.03	0.00	0.00	0.00	0.00
Total	98.41		98.91		99.1	
n	12		3		3	
Fo	87.80	0.32	88.65	0.16	87.79	0.67

TABLE 6: Spinel Analyses

Experiment Set 2: Anorthite and Forsterite Saturated

	N-MORB Starting Material										E-MORB Starting Material		HAB Starting Material			
	*1290° Equil. T.		1290° Equil. T.		1260° Equil. T.		1230° Equil. T.		1210° Equil. T.		1290° Equil. T.		1290° Equil. T.		1230° Equil. T.	
	Avg	2σ	Avg	2σ	Avg	2σ	Avg	2σ	Avg	2σ	Avg	2σ	Avg	2σ	Avg	2σ
SiO_2	0.05	0.12	0.01	0.03	0.08	0.07	0.56	1.22	0.00	0.00	0.00	0.00	0.15	0.07	0.14	0.05
TiO_2	0.03	0.04	0.08	0.02	0.22	0.06	0.26	0.11	0.19	0.01	0.06	0.03	0.04	0.02	0.07	0.02
Al_2O_3	63.50	0.26	61.47	1.90	41.51	4.98	32.95	1.34	31.62	0.39	68.35	0.56	67.21	0.45	67.97	0.26
Cr_2O_3	5.44	0.25	6.03	1.96	28.1	4.45	30.18	0.66	29.37	0.01	0.66	0.52	0.38	0.39	1.34	0.37
FeO*	5.61	0.25	7.46	0.08	10.5	1.68	16.27	2.06	18.73	0.02	4.94	0.22	7.49	0.77	5.81	0.12
Fe^{2+}	4.80	0.27	0.03	0.03	7.38	0.87	9.82	2.46	7.30	0.32	4.17	0.34	0.04	0.03	0.05	0.04
Fe^{3+}	1.07	0.40	7.76	0.08	3.44	0.85	6.77	1.66	14.95	0.02	1.01	0.20	7.83	1.02	5.96	0.13
MnO	0.00	0.00	0.00	0.00	0.04	0.02	0.15	0.02	0.12	0.08	0.00	0.00	0.04	0.02	0.04	0.01
MgO	24.13	0.38	23.98	0.28	20.24	1.01	17.35	0.42	17.19	0.10	25.02	0.32	23.15	0.35	24.62	0.31
ZnO	0.00	0.01	0.03	0.03	0.14	0.14	0.03	0.04	0.05	0.41	0.01	0.02	0.00	0.00	0.00	0.00
V	0.02	0.02	0.04	0.03	0.16	0.06	0.15	0.05	0.12	0.03	0.04	0.03	0.02	0.01	0.05	0.02
Total	99.03		99.43		101.3		98.22		100.9		99.32		98.86		100.2	
n	7		12		5		5		3		10		3		11	
Cr#	0.05	0.03	0.06	0.02	0.31	0.06	0.38	0.01	0.38	0.00	0.01	0.01	0.01	0.00	0.01	0.00
Mg#	0.90	0.01	0.91	0.01	0.83	0.02	0.76	0.05	0.78	0.00	0.91	0.01	0.86	0.01	0.90	0.01
Fe^{3+}#	0.01	0.00	0.01	0.00	0.04	0.01	0.08	0.02	0.08	0.01	0.01	0.00	0.01	0.00	0.01	0.00

*Experiment with 4 hour run time

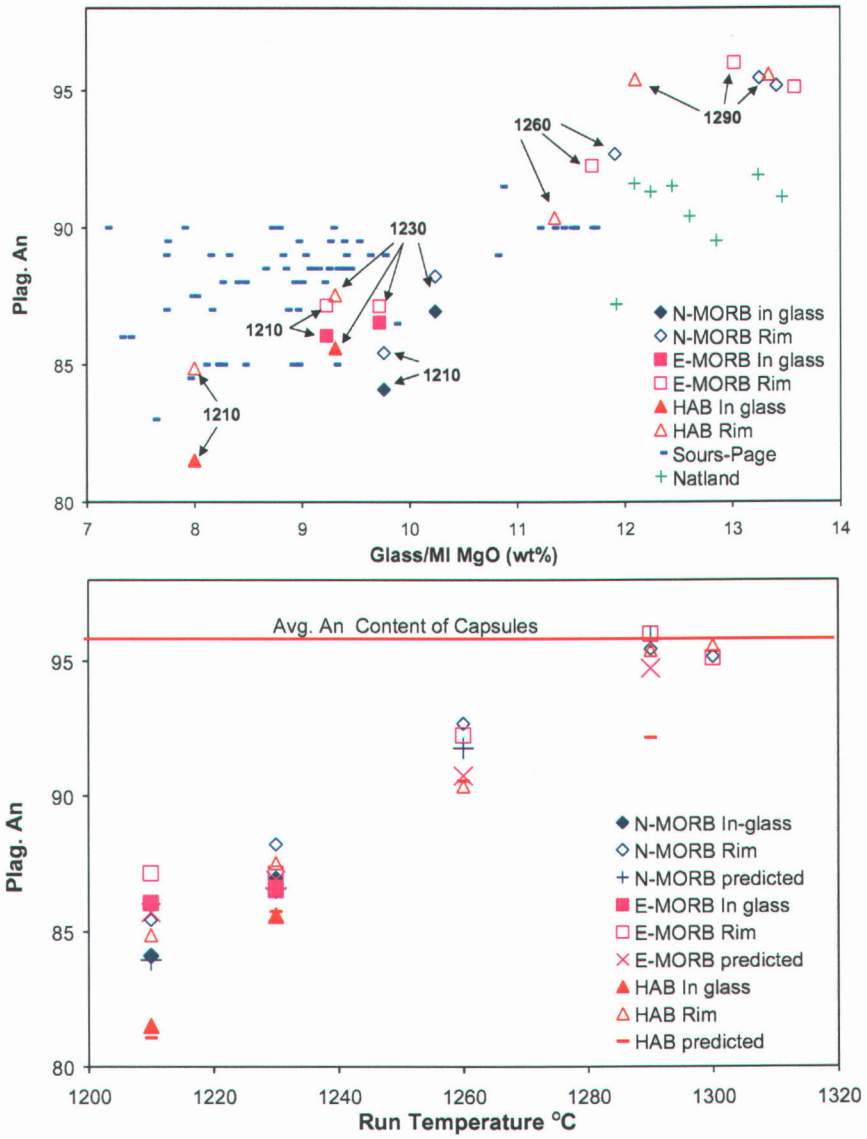

Figure 3

Figure 3-top: An content of feldspars from Experiment Set 2 vs MgO of host liquid. "Sours-Page" refers to host feldspar An and melt inclusion MgO from Sours-Page et al. (1999, 2002) and "Natland" refers to host feldspar An and MI MgO from Natland (1989). "Rim" refers to capsule rim reaction zone, "In-glass" are feldspars that crystallized from the melt.

-bottom: An content of feldspars and capsule reaction zones from Experiment Set 2 vs. equilibration temperatures. "Predicted" are the An values of feldspar predicted for the melt composition.

experiment with a 4-hour equilibration period. This indicates that any gradients or melt diversity had dissipated within four hours equilibration time. At the lower equilibration temperatures (1210°, 1230° and 1260°), the N-MORB-derived liquids produced chromite (Cr# of 0.31–0.38) with Al_2O_3 contents of 32.95–41.51 wt% (Table 6), but this phase was

not present in the E-MORB- and HAB-derived melts. At 1230°, the HAB-derived melt produced Al-spinel (Al_2O_3 of 67.97 wt% and Cr# of 0.01) within the An_{86} feldspar overgrowth on the rim of the capsule; this was the only occurrence of aluminous spinel noted at lower temperatures (<1260°C).

The compositions of our lower temperature spinels from N-MORB experiments were colinear with chromite compositions reported by Allan et al. (1989) for the Lamont seamounts (Figure 6). The spinels at 1260° were comparable in Cr# and Al content to the most Cr-rich spinels in abyssal peridotites (Dick and Bullen, 1984; Dick, 1989), spinel in lherzolite xenoliths (BVSP, 1981) and spinel observed as inclusions in MORB anorthite megacrysts (Fisk et al., 1982; Sinton et al., 1993), while those produced at 1290° were several wt% more aluminous than natural examples.

Glass compositions, with the exception of CaO, follow a liquid line of descent from the melting temperature of 1300°C through 1210°C with decreasing MgO (Table 3, Figures 7, 8, 9, 10, and 11). These trends were also colinear, i.e., parallel, to the trends of published data from the source suites of the starting glasses (Davis and Clague, 1987; Karsten et al., 1990; Donnelly-Nolan et al., 1991). Aluminum contents of liquids derived from all three starting glasses fall along a trend from the high-temperature to low-temperature compositions (Figure 7). The increase in the ratio of Al_2O_3 to MgO at higher temperature shows that Al-rich melts were present prior to feldspar crystallization due to the Al component being added through reaction with the capsule during saturation. The Al component decreases with temperature due first to reaction with the capsule through Al-Si cation exchange and the formation of Al-spinel, and then through crystallization of feldspar within the liquid.

For all starting compositions, Na was systematically low (Figure 8). This is possibly due to reaction with the capsule wall, and loss to the furnace atmosphere, although the amount of melt exposed to the atmosphere is small. CaO trends were distinctive for each starting composition and may in part reflect the effects of differing points of the onset of plagioclase crystallization. The CaO content in N-MORB-derived liquids remained nearly constant with decreasing MgO and temperature. The E-MORB-derived melts show a parabolic trend with a minima of 12.15% CaO at 1260° and 11.7%

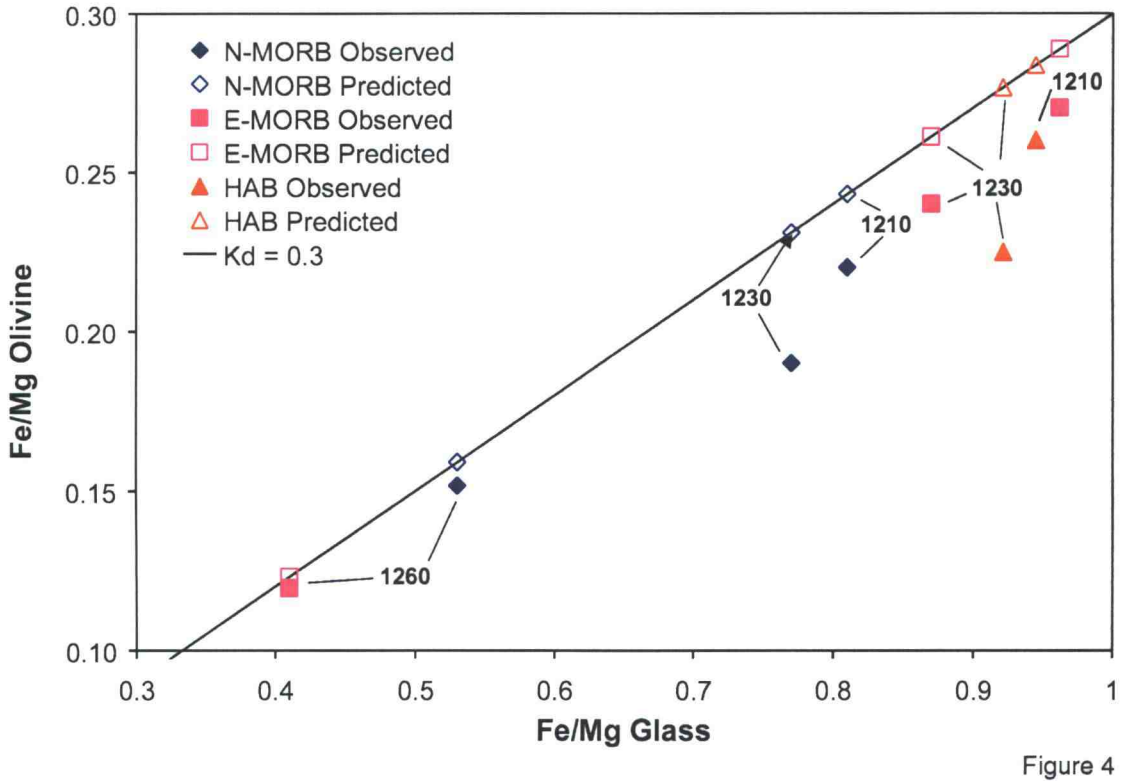

Figure 4

Figure 4: FeO/MgO of olivines that crystallized in the melt vs. melt FeO/MgO for Experiment Set 2. Kd line delineates where the points should fall for olivines in equilibrium with melt based on FeO/MgO partition coefficient of 0.3. Labels refer to equilibration temperatures.

MgO, while the HAB-derived liquids have a less pronounced parabolic trend with the minima of 11.1% CaO at 1230° and 9.31% MgO (Table 3, Figure 9). Although CaO trends do not describe LLDs from the 1300° melt to the starting glass and starting glasses lava suites, the CaO contents of the experiments that nucleated plagioclase (1230° and 1210°) do fall within the range of MORB glass compositions from the RIDGE data set for the Mid-Atlantic Ridge (Figure 9). The rate of TiO_2 decrease versus increased MgO was enhanced at higher temperature for N-MORB compositions (-0.3 to -0.8 between 1300° and 1290°). E-MORB showed the greatest decrease for each percent increase MgO between 1230° and 1210° C (-0.65), while HAB-derived liquids had a consistent value of a 0.17% decrease in TiO_2 for each percent increase in MgO (Figure 10). The Mg# of the glass remained relatively constant as a function of temperature (~69–80; Table 2), which may represent a buffering effect that was also observed in the linear trends of FeO*

versus MgO (Figure 11). The FeO* content of the melts increased with falling temperature and MgO; this trend was linear for N-MORB- and E-MORB-derived melts, while FeO* was relatively constant between 1230° and 1210° for HAB-derived liquids (Figure 11).

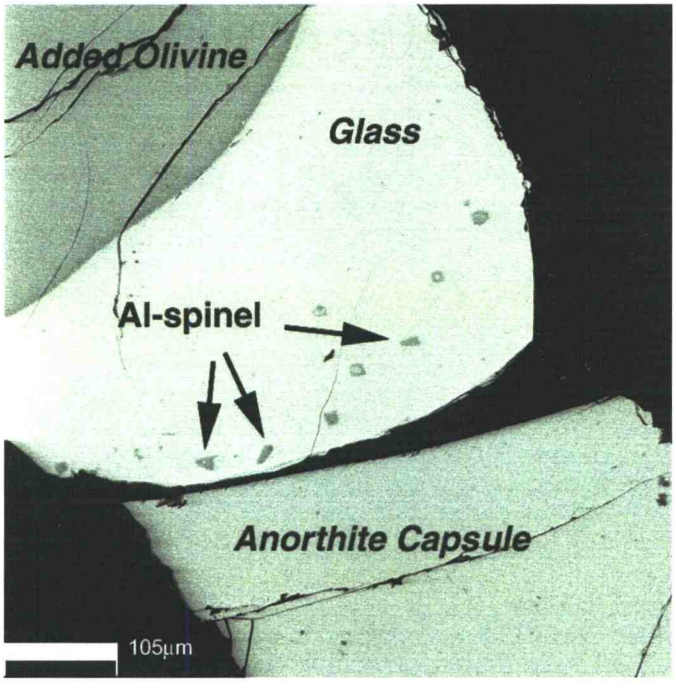

Figure 5: Backscattered electron image of experimental run with an equilibration temperature of 1290° C and equilibration time of 4 hours. Bands of Al-spinel have formed in the melt adjacent to the capsule rim. Anorthite capsule has separated from glass during mounting.

Experiment Set 3: Anorthite and Forsterite Saturated Melt, Variable Melt T

The third set of experiments separated the effects of equilibration temperature from potential effects of undercooling (ΔT). As described earlier, this was accomplished by keeping the equilibration run temperature fixed at 1210° and varying the initial melting temperatures, which were chosen to repeat the same amounts of undercooling used in experiment set 2.

There was diversity among the compositions of crystallization products. The feldspars from the 70° undercooling experiments had outer rims (~25 μm in the largest crystals) that were An_{81-83} and cores up to An_{96}. With 40° undercooling, the feldspars

had thin (~10 μm) An_{91} rims surrounding an An_{94-95} core. Although 10 degrees of undercooling produced the lowest glass Mg# of any forsterite saturated experiment (Table 2), the feldspars produced had the highest average An content of any experiment: $An_{95.5}$. These also had a ~5 μm An_{88} zone on the surface in contact with the melt. Figure 12 shows that moving the melting temperature closer to an equilibration temperature of 1210° (decreasing ΔT) increases difference between the expected and observed An contents of the plagioclase in the melts. This indicates that using an initial melting temperature within the plagioclase crystallization field can produce feldspars that have high-An contents, but are out of equilibrium with the melt. This observation supports our use of a melting temperature of 1300° in Experiment Set 2.

Although there was some diversity among glass compositions from Experiment Set 3, the compositions overall were similar to the 1210° compositions from Experiment Set 2, where the melting temperature was 1300° and ΔT was 90° (Figure 13). There was a systematic variation with MgO content, which decreased as the melting temperature decreased. However, even this variation was minor, from 9.77% with 70 degrees of undercooling (1280°C melting temperature) to 9.38% with 10 degrees undercooling (Table 3). Melt in this experiment also had higher CaO values than other experiments using N-MORB glass, but this was less than 1% compared to other experiments with a 1210° equilibration temperature. Melts with 10 and 40 degrees of undercooling had the lowest glass Mg# (66.9 and 67.4; Table 2).

With 70° of undercooling, euhedral prisms and laths of zoned feldspars were produced. Melt inclusions were common, as were large embayments on the prisms and hollow cores on the laths, with some resorbed faces (Figure 14). The experiment using 40° undercooling crystallized feldspars that were near equant prisms with rounded corners. The feldspars with 10° undercooling had disequilibrium textures, with resorbed faces and corners that resulted in anhedral crystals.

If the trends produced by Experiment Set 3 were over the same range of compositions as the Experiment Set 2, then any conclusions we reached about the control equilibration temperature has on composition would be questionable. Instead, the glass compositions from the results of Experiment Set 3 were similar only to the 1210°

experiment of set 2. Although decreasing the melting temperature did decrease the MgO content, this variation was minor. This confirms that equilibration temperature has a greater influence on melt composition than the amount of undercooling. However, the disequilibrium textures and zoning of the feldspars indicate that with low melting and saturation temperatures, the 24-hour run time we used was insufficient to achieve feldspar-melt equilibrium. In comparison, when an equilibration temperature of 1290° and a melting temperature of 1300° were used in Experiment Set 2 (which is the same amount of ΔT as the experiment with 1220° melt and 1210° run temperatures), four hours equilibration time was sufficient to produce the same results as 24 hours (Table 3). This indicates that the run temperature is a controlling factor in the speed of equilibration as well.

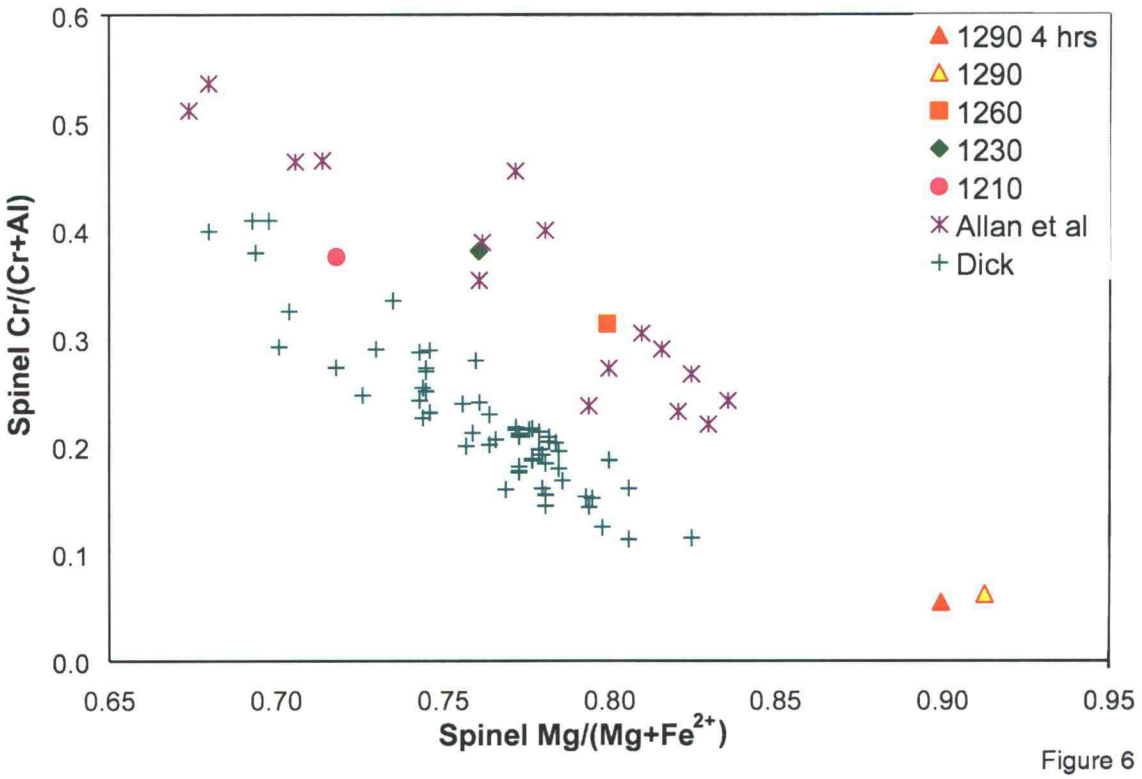

Figure 6: Cr# vs. Mg/(Mg+Fe^{2+}) for spinels crystallized from N-MORB derived liquids in Experiment Set 2. Label numbers refer to equilibration temperature in degrees C. "Dick" refers to the compositions of abyssal peridotite spinels in Dick (1989), "Allan et al," refers to compositions of spinels, naturally occurring in lavas of the Lamont Seamount Chain, reported in Allan et al., (1989).

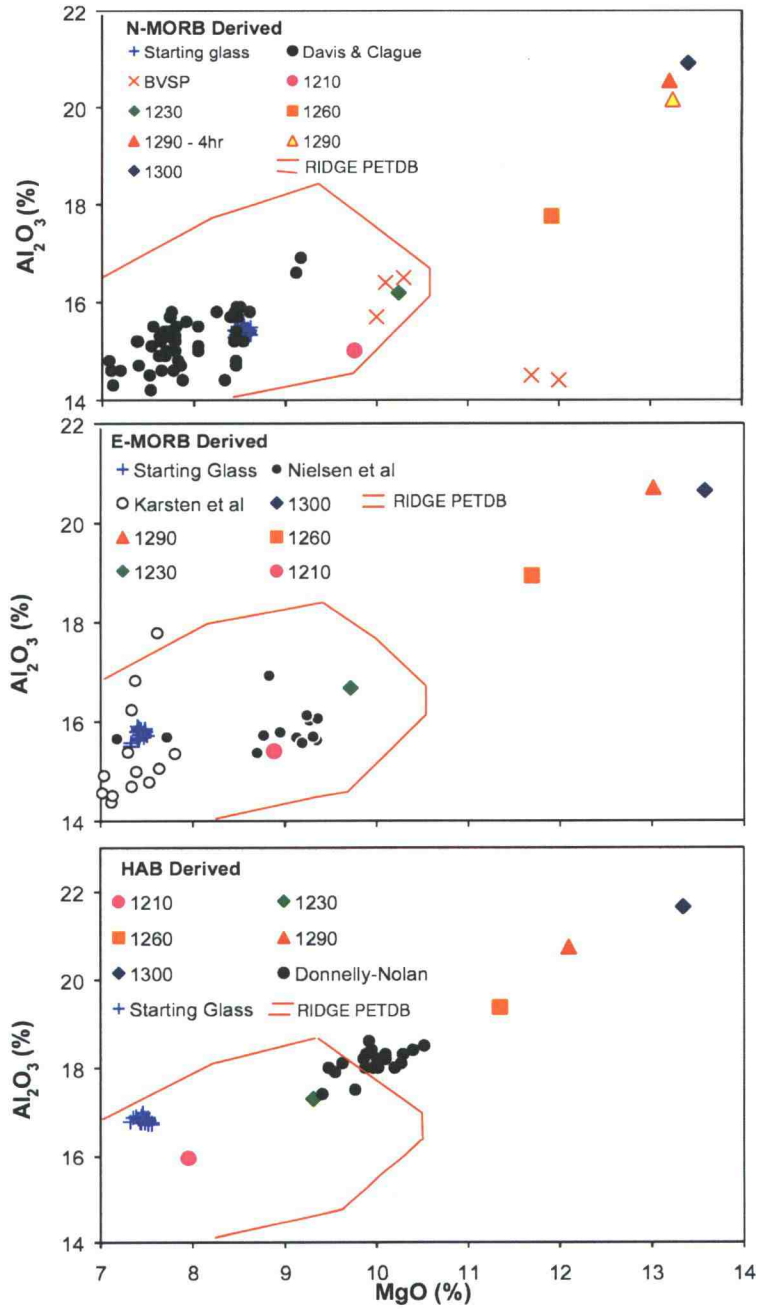

Figure 7

Figure 7: Al_2O_3 vs MgO for Experiment Set 2. Numbers refer to equilibration temperatures. BVSP refers to hypothetical primary MORB magma (BVSP, 1981). Davis and Clague refers to compositions from the Gorda Ridge in Davis and Clague (1987). Karsten et al. refers to Endevour Segment compositions in Karsten et al. (1990), Sours-Page et al. refers to melt inclusion compositions from the same segment in Sours-Page et al. (1999), Donnelly-Nolan refers to compositions from Giant Crater, Medicine Lake, CA in Donnelly-Nolan et al. (1991). Region outlined in red contains range of Mid-Atlantic Ridge glass compositions in the pre-compiled RIDGE petrologic database (RIDGE PETDB).

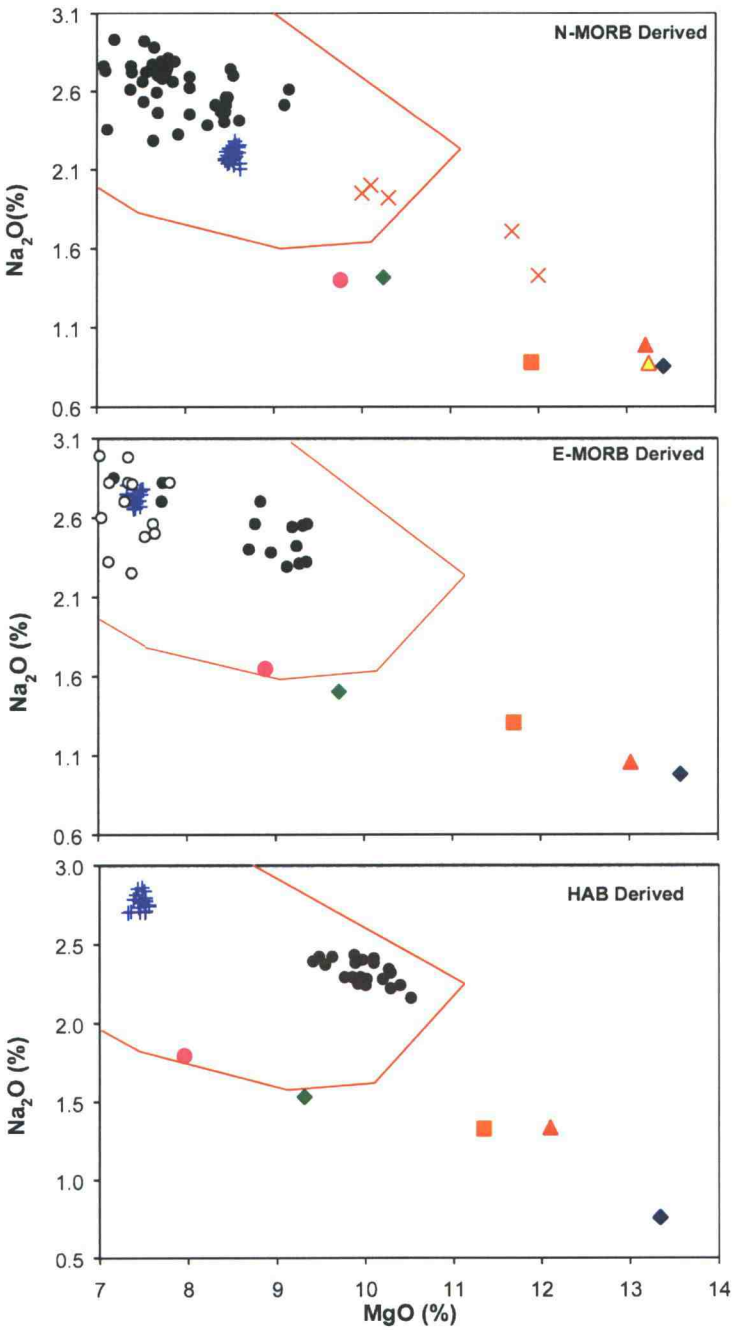

Figure 8

Figure 8: Na_2O vs MgO for Experiment Set 2. Symbols same as Figure 7.

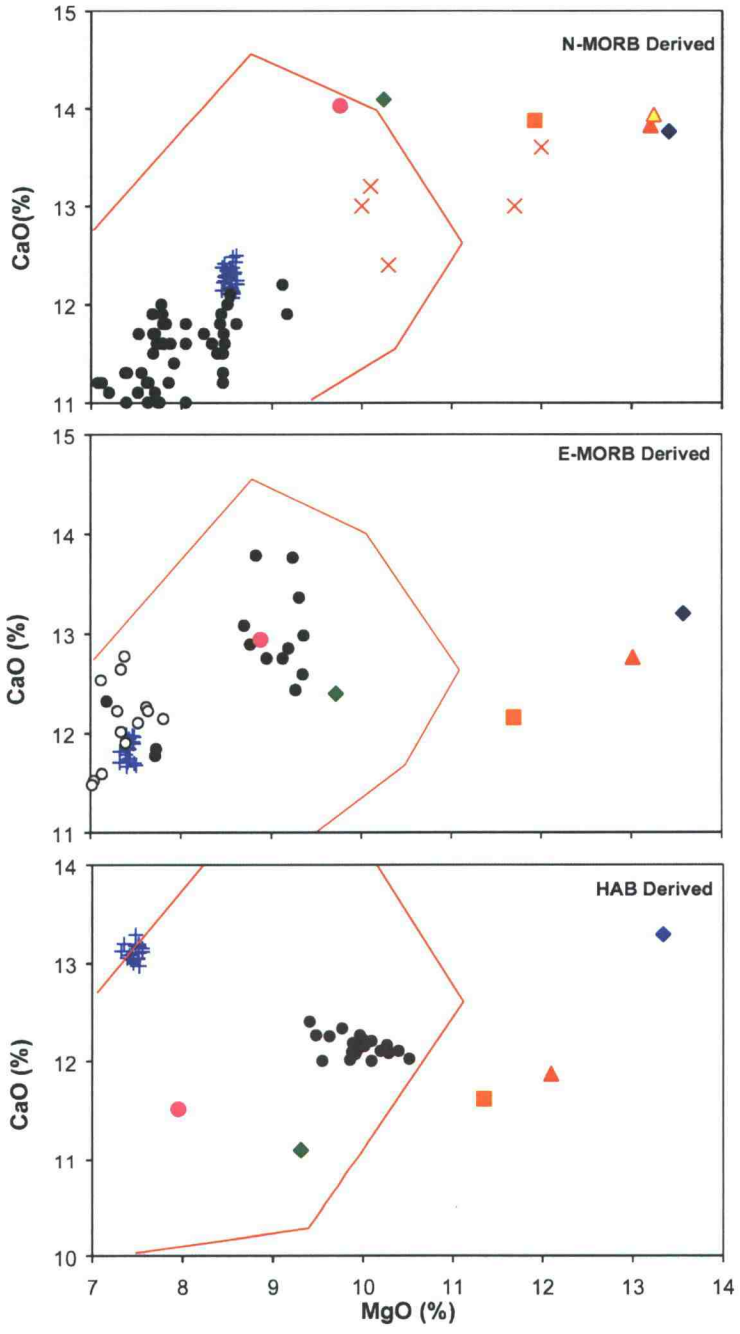

Figure 9

Figure 9: CaO vs MgO for Experiment Set 2. Symbols same as Figure 7.

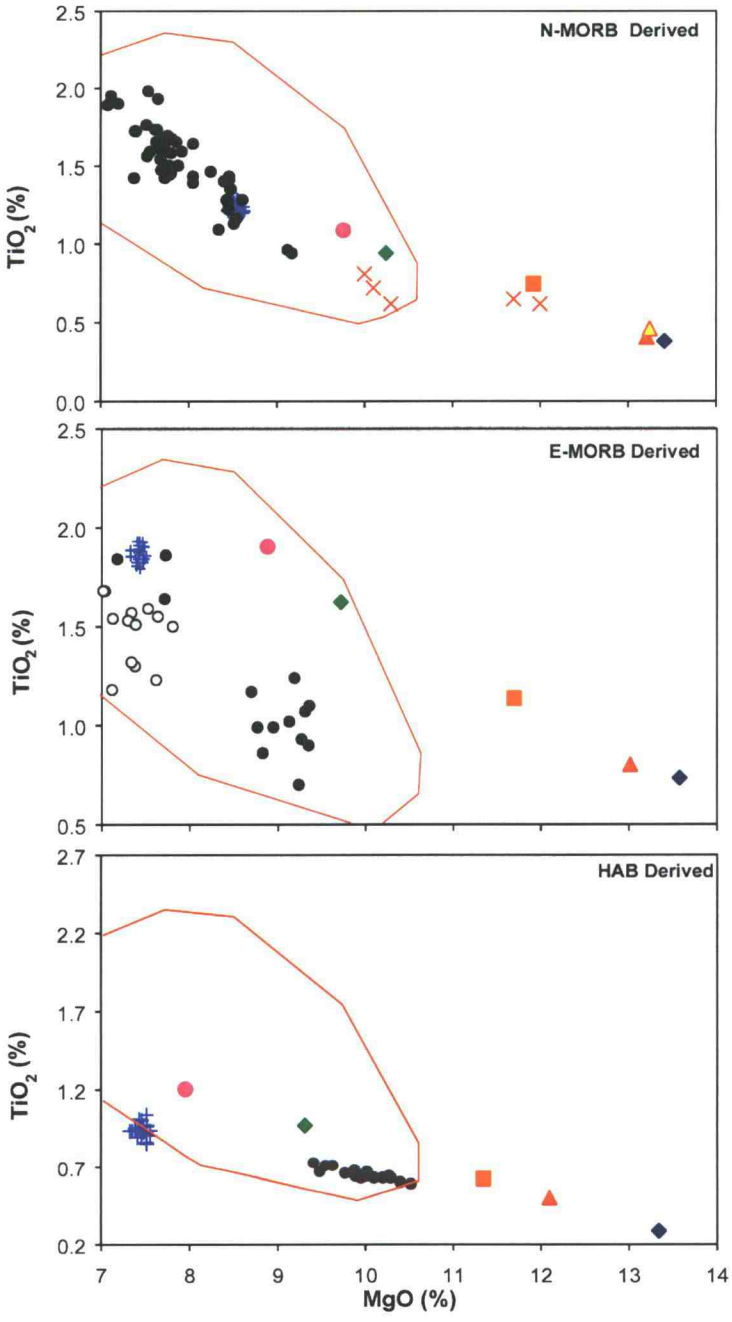

Figure 10

Figure 10: TiO_2 vs MgO for Experiment Set 2. Symbols same as Figure 7.

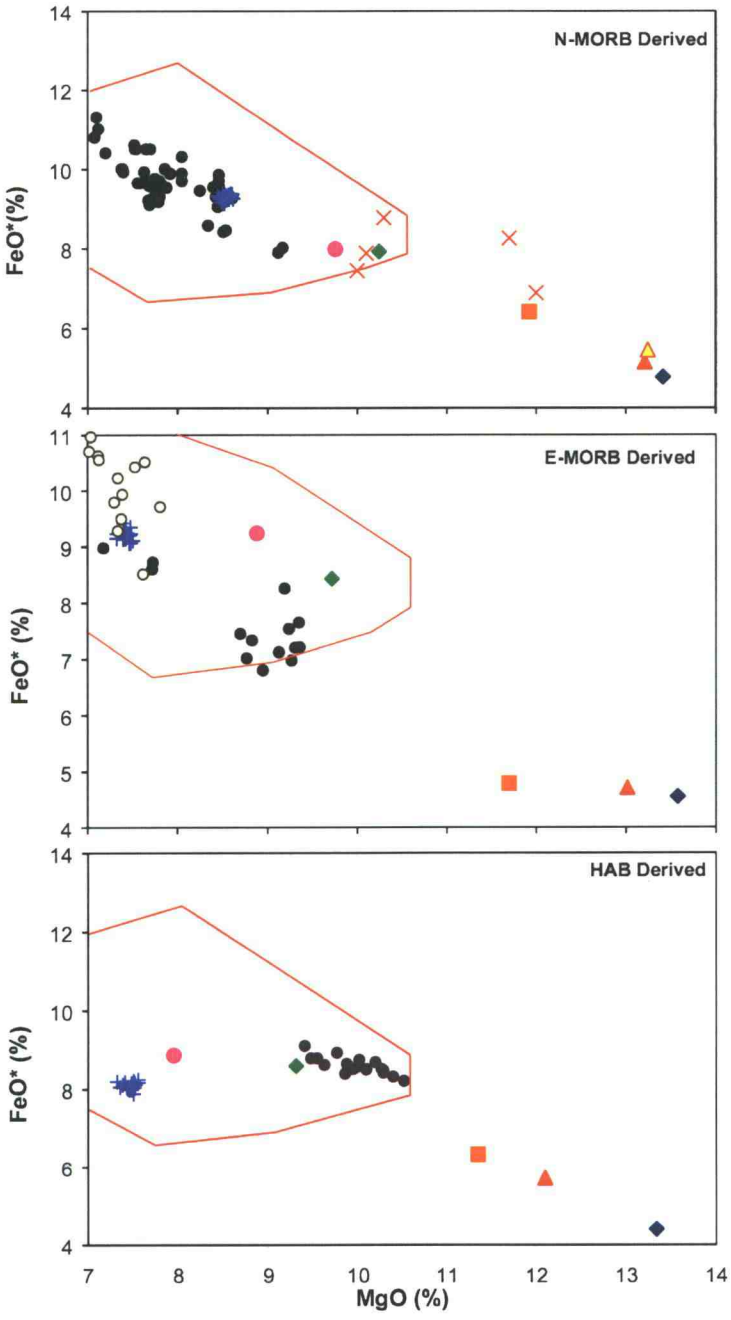

Figure 11

Figure 11: FeO* vs MgO for Experiment Set 2. Symbols same as Figure 7.

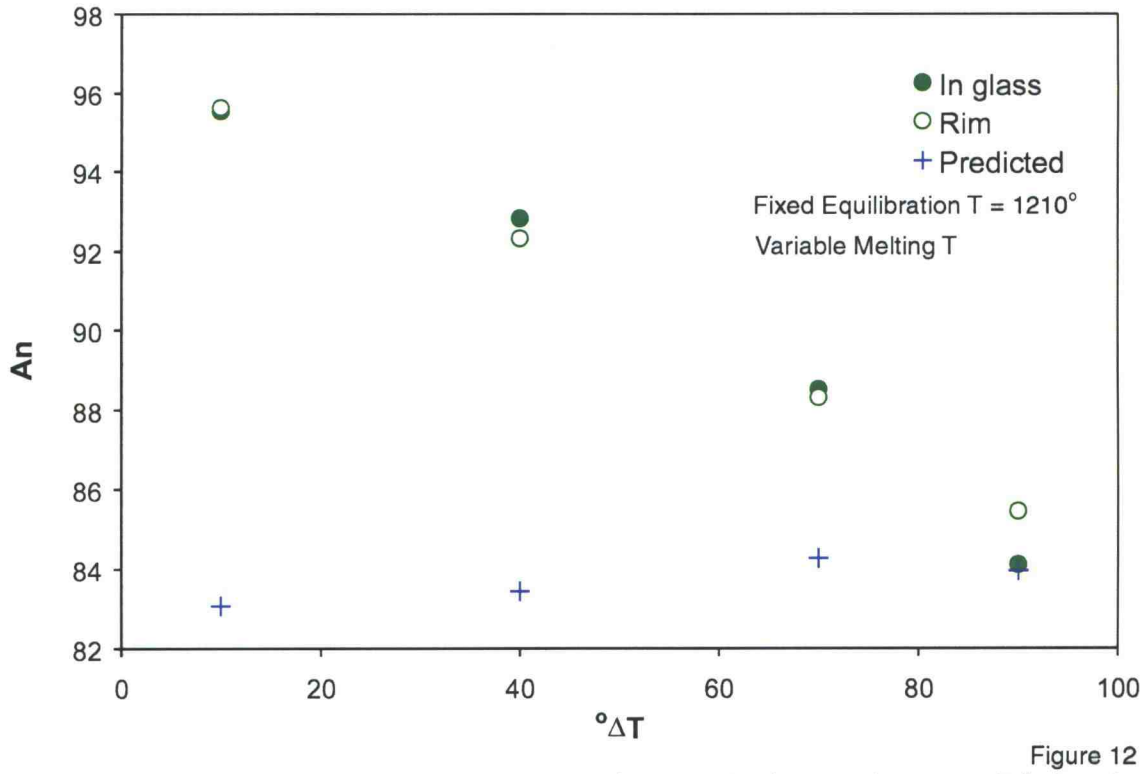

Figure 12

Figure 12: Comparison of observed An values for capsule rim reaction zone (Rim) and feldspar crystallized from the melt (In-glass) to the predicted equilibrium values for variable melting temperatures and ΔT and a fixed equilibration T of 1210°. Note that as the melting T and ΔT decrease, the feldspars are increasing out of equilibrium with the melt. All equilibration times are 24 hours.

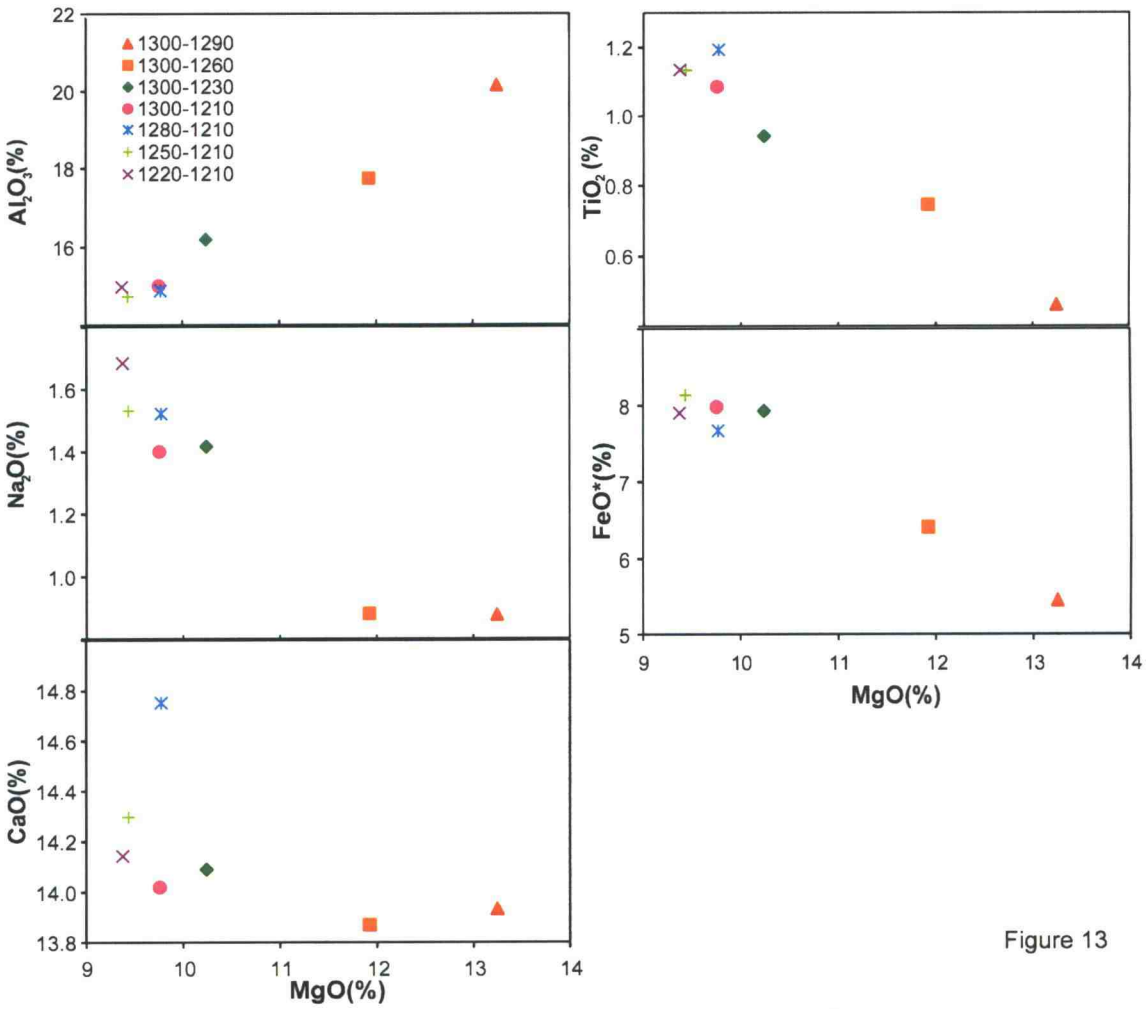

Figure 13

Figure 13: Comparison of the compositions of melts from Experiments Set 2 to Experiment Set 3. First number refers to melting temperature, second to equilibration run temperature. Set 2 experiments have 1300° melt T. Note that compositions from Set 3 are similar to the 1210° experiment from Set 2, showing that equilibration T has a greater influence on melt compositions than melt T or ΔT.

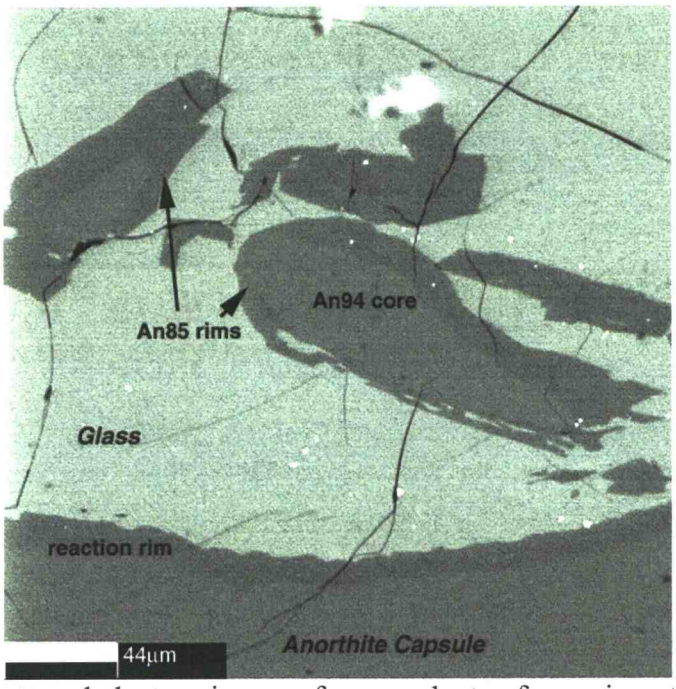

Figure 14: Backscattered electron image of run products of experiment with a melting temperature of 1280° and equilibration temperature of 1210° ($\Delta T=70°$). Dark gray is feldspar, light gray is quenched melt. Note zoning of the feldspars and disequilibrium texture of some faces on the crystals.

DISCUSSION

The primary goal of these experiments was to determine the composition of anhydrous mafic liquids in equilibrium with high-An feldspar. We must again emphasize that the design of our experimental apparatus should not be mistaken as an attempt to simulate a natural process where primitive melt reacts with plagioclase and we do not intend to propose such a model. Rather, our experiments were designed to saturate melts in anorthitic components at high temperatures, observe the composition of the melts and the phases that crystallize in the melt at lower run temperatures, and compare the results to natural examples. Only then do we propose a model.

In our initial runs (Experiment Set 1), we observed that anorthite saturation alone was not sufficient for producing $>An_{85}$ feldspar or melts that resembled natural lava suites in composition (Figures 1 and 2). The experimental liquids did resemble refractory melt inclusions observed by Johnson et al. (1995), but these natural examples occurred in feldspars with An > 85.

However, the results of our second set of experiments show that basaltic melt that is in equilibrium with both high-An feldspar and high-Fo olivine is generally similar to natural basalt glasses and melt inclusions hosted by high-anorthite feldspar. The composition of the starting materials (Table 1) may have had some effect in the ability to achieve equilibrium, but it is important to note that the compositions of all liquids once saturated with anorthite and forsterite during the melting period (1300°) were very similar despite the different starting glasses (Tables 1, 2, and 3). The saturated liquids all had high CaO/Na_2O values, and Al# above 30. E-MORB-derived liquids that crystallized plagioclase (i.e., those at 1210° and 1230°) were closest to natural glasses in composition for all major elements, while the olivines that crystallized in E-MORB-derived melts were closest to their predicted equilibrium values (Figure 4). It is possible that the modified HAB and N-MORB compositions would produce better equilibrium results using time-temperature profiles different from those of our experiments. The issues relating to the effects of cooling rate and the length of the equilibration period have been addressed in another group of experiments that also dealt with melt inclusion formation (Nielsen and Kohut, 2000; Kohut and Nielsen, 2002) and will be reported in full in a separate paper (E. J. Kohut and R. L. Nielsen, Melt inclusion formation mechanisms and compositional effects in high-An feldspar and high-Fo olivine in anhydrous mafic silicate liquids submitted to Contributions to Mineralogy and Petrology, 2003).

The similarity of the compositions our glasses that crystallized high-An feldspar from experiment sets 2 and 3 to the relevant starting glasses (Karsten et al., 1990; Donnelly-Nolan et al., 1991; Davis and Clague, 1987) and natural basalt arrays (RIDGE PETDB), is an important difference between our experiments and those of Panjasawatwong et al. (1995). While they also produced liquids in equilibrium with high-An feldspar, their glass compositions did not resemble natural basalt suites and due to their lower MgO contents do not fall within the limits of the data we present on Figures 7, 8, 9, 10, and 11. However, while Panjasawatwong et al. (1995) did raise the Al content and Ca/Na ratio of their melts, they did not saturate their liquids with forsterite. We observed that the melt saturated in forsterite as well as anorthite at high temperature when cooled produced $An_{81.5-87}$ feldspar in equilibrium with the melt; as noted earlier, the initial experiments saturated in only anorthite crystallized An_{76-79}

feldspars. The additional phase, high-Fo olivine, may limit the degrees of freedom in the system and constrain the phases to those on the forsterite-anorthite cotectic, which would favor plagioclase with a high-An content (Figure 15). It is significant that the liquids are constrained to this cotectic, as high-An and high-Fo olivine are the first crystallizing phases in most primitive MORB lavas (Sinton et al., 1993; Nielsen et al., 1995). However, no liquids with such high Mg# that follow this cotectic have been produced experimentally prior to now. In addition, the host glass MgO and plagioclase An contents of Experiment Set 2 are similar to feldspar An content and melt inclusion compositions described by Sours-Page et al. (1999, 2002). These similarities to natural systems suggest that our experiments are valid analogs for some magmas parental to anorthite-bearing anhydrous basalts.

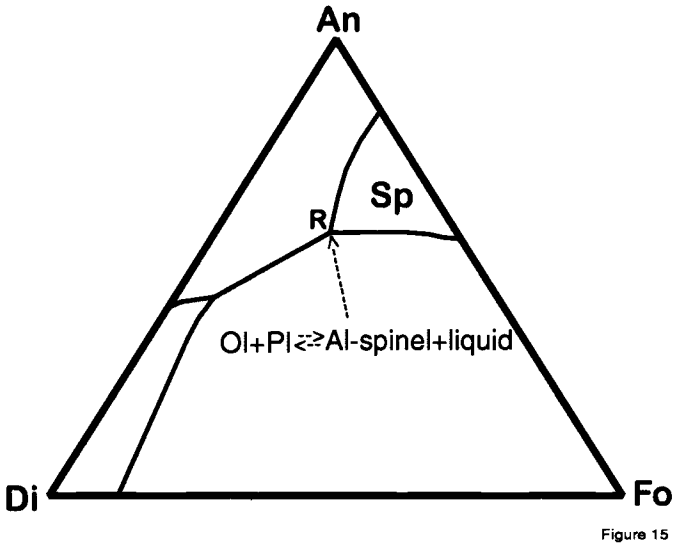

Figure 15: 1 atm An-Fo-Di ternary with spinel field (modified from Osborn and Tait, 1952). Aluminous spinel reacting with liquid at reaction point R produces high-An plagioclase and high-Fo olivine. Crystallization then proceeds along the olivine-plagioclase cotectic.

The mineralogy and composition of experimental run products at 1230° and 1210° are also similar to primitive lavas of the Sasha Seamount of the Lamont Seamounts. The significance of this is that the Lamont Seamounts occur off-axis and the similarity to our compositions indicates that the experiments are also applicable to anhydrous melts that do not originate at mid-ocean spreading centers. The Sasha Seamount lavas have MgO contents up to 9.7%, Mg# up to 72, and contain Fo_{85-91}

olivine, An_{70-91} plagioclase phenocrysts and Cr-rich spinel (Allan et al., 1989). The calculated normative phase relations of the most primitive Lamont Seamount lavas were reported by Allan et al. (1989) to be consistent with formation at shallow pressures (below 10 kb) and at temperatures of 1200°–1240° C. These suggested conditions of formation correlate well with our experimental parameters.

The observation of Al-spinel at 1290°, (anorthite/forsterite saturated experiments) despite no spinel having been added to the starting mixtures indicates that liquids that are in equilibrium with anorthite and forsterite at lower temperatures are in equilibrium with Al-spinel at this temperature. This is what the An-Fo-Di ternary diagram (Figure 15) would predict, and we suggest that our 1290° experiments fall within the spinel field of the ternary. As the run temperatures decrease, our experiments progress along the olivine-plagioclase cotectic of the ternary diagram with decreasing temperature. To reach the olivine-plagiclase cotectic, the liquid composition must pass first through point R (Figure 15), where Al-spinel will react with the remaining liquid to produce high-An plagioclase and high-Fo olivine. For our experiments, a ternary diagram with a larger spinel field may be appropriate, as the starting compositions contain small amounts of Cr (Table 3). Trace amounts of Cr will stabilize a larger Al-spinel field in ternary space at the expense of anorthite, and can move the reaction point to a lower temperature, e.g., ~1275°C (Onuma and Tohara, 1983). The An-Fo-Di ternary diagram of Osborn and Tait (1952), upon which Figure 15 is based, has the reaction point at a higher temperature (~1320°) than those used in our experiments.

The compositions of spinel and olivine in the run products are similar to those in natural, primitive mafic lavas. The compositions of olivines that crystallized in the liquids at run temperatures of 1260° (Table 2) demonstrate that our experiments were in equilibrium with high-Fo olivine, similar to mantle olivine (Dick and Fisher, 1983). The spinel compositions are a function of experimental temperature, with Al content decreasing and Cr/Al content increasing, with decreasing temperature (Figure 6). While, the high-Al spinels formed in bands, the chromites at lower temperatures in the N-MORB experiments formed throughout the liquid. This provides evidence that the liquid assimilates the Al-spinel with decreasing temperature, and the lack of Al-spinel at lower

temperatures indicates that the system has proceeded past the reaction point. The Al-spinel observed at 1230° for the HAB-derived melts may indicate that particular system is still at the reaction point at lower temperatures, or it may indicate that with the HAB starting composition, our time-temperature profile was not suitable for achieving true equilibrium results at 1230° run temperature and 70° ΔT.

One possible mechanism for producing the observed compositional trends is to buffer an evolving magma with Al-spinel, similar to those characteristic of the most primitive MORB and depleted seamount lavas and some abyssal peridotites (Dick and Bullen, 1984; Allan et al., 1989). The reaction of a primitive magma with the spinel would maintain high Al_2O_3 and MgO contents at the reaction point (R in Figure 15), where the melt is three-phase (anorthite-fosterite-spinel) saturated. As the Al-spinel is consumed, the reaction proceeds along the fosterite-anorthite cotectic (Figure 15). This would result in the reaction Al-sp + liquid →pl + ol ± chromite with decreasing temperature.

The third set of experiments illustrate that while moving the initial melting temperature close to the equilibration run temperature does not greatly effect the liquid composition, it does effect the chemistry of the crystallizing feldspars, and these are further from equilibrium with the melts as ΔT decreases (Figure 12). This indicates that the smaller the difference between the melt and equilibration temperature, the greater the amount of time required to achieve equilibrium. We suggest that the feldspars that formed early during the equilibration period may have had higher-An values and were out of equilibrium with the host liquid. As the equilibration period progresses, rims form on the early formed feldspars that have An contents closer to equilibrium with the melt and eventually the entire feldspar would equilibrate with the melt. Later formed feldspars would be in equilibrium with the melt. The length of the required equilibration period though, depends on both undercooling and the temperature of equilibration; the experiment with an equilibration temperature of 1230° from Set 2 also had a ΔT of 70°, yet the feldspars were in equilibrium with the melt. This indicates that while at any run temperature decreasing ΔT may require an increase in the length of the time required to achieve melt/crystallizing mineral equilibrium, this effect becomes more pronounced at

lower equilibration temperatures. With regards to the Al-spinel/liquid reaction just described, we suggest that the lower the temperature of the liquid reacting with the spinel, the longer the period of time needed for the liquid to react.

The amount of crystallization in our experiments as a function of temperature was estimated using the trend of TiO_2 versus MgO. For systems saturated with Al-spinel, plagioclase and olivine, Ti can be considered an almost completely incompatible element (D = 0). For any completely incompatible element, the Rayleigh distillation equation simplifies to $F \cong C_o^l/C^l$ (where F is the amount of liquid remaining, and C_o^l and C^l are the initial and current concentration of the trace element in the liquid respectively). If one then assumes a bulk D_{Ti} of 0 for this assemblage, the Ti content in the glass will vary only by the ratio of the liquid/solid fraction. Using the TiO_2 content correlated with MgO, we can calculate the percent crystallization for each percent decrease in MgO and correlate that with the temperature in our experiments.

The results of our calculations (Table 7) indicate large amounts of crystallization would occur for each percent decrease in MgO: these average ~27% for N-MORB-derived, ~16% for E-MORB-derived, and ~24% for HAB-derived melts. However, these averages cannot be extrapolated linearly, as the HAB- and N-MORB-derived liquids had higher calculated rates of crystallization per % decrease MgO at 1260° and 1290° (28–35% and 35–37% respectively) than at 1230° and 1210° (Figure 16). If our 1230° and 1210° experiments are valid analogs of natural primitive basalts (≥8% MgO), then even primitive MORB lavas may have undergone a large amount, 62–77%, of crystallization prior to eruption (Table 7). These amounts however, must be examined in the context of the buffering effect the added olivine crystal and anorthite capsule.

We attempted to produce numerical models for our data using the MELTS (Ghiorso and Sack, 1995) and MIXNFRAC (Nielsen, 1990) algorithms. Although neither program was able to produce a model that accurately reflected our results, the assimilation model provided trends that were similar to the experimental data. The predicted phase assemblages also concurred with our lack of pyroxene saturation in the experiments. Nevertheless, the results were even more illustrative of our need to recalibrate our models to these melt compositions. Currently, we are clearly not in a

position where we can adequately simulate magmatic processes for this abundant, very primitive precursor class of basaltic magmas.

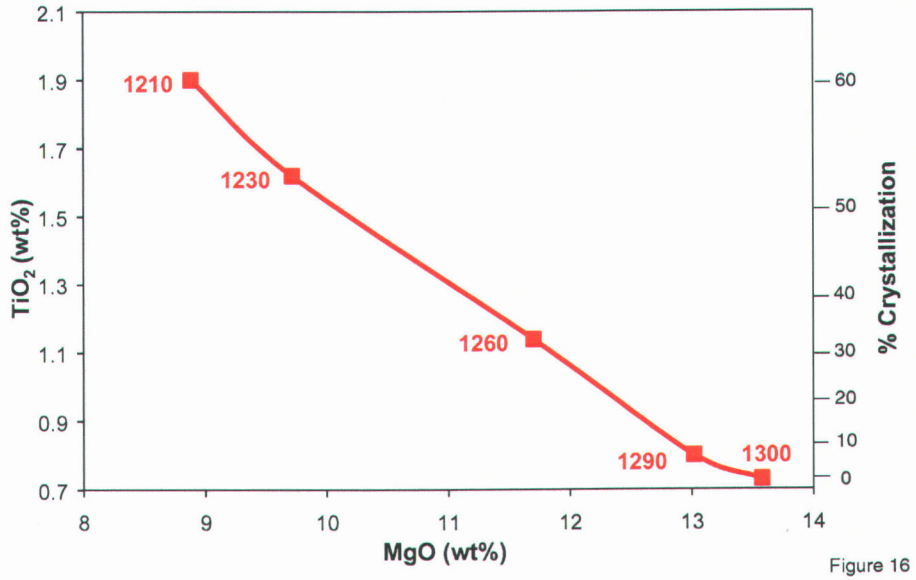

Figure 16: TiO_2 content and % crystallization as functions of MgO content of experiments using E-MORB starting compositions. Labels of points in plot refer to equilibration temperature.

TABLE 7: Calculated Crystallization

% Crystallization based on TiO_2 change

T Change	N-MORB	E-MORB	HAB
1300-1290	7.32	8.75	44.00
1300-1260	49.33	35.96	55.56
1300-1230	59.57	54.94	71.13
1300-1210	63.11	61.58	76.86

% Crystallization/per MgO% decrease

T Change	N-MORB	E-MORB	HAB
1300-1290	36.59	15.63	35.48
1300-1260	32.89	19.13	27.92
1300-1230	18.79	14.23	17.65
1300-1210	17.34	14.34	14.39
average	26.4	15.83	23.86

While we do not discount the fact that anorthite in MORB can originate from the primary melting of refractory material (Natland, 1989; Johnson et al., 1995), we propose that our results indicate that other mechanisms for producing high–An feldspar may also exist that explain other, more recent melt inclusion data (e.g., Sours-Page et al., 2002). We suggest that the evidence outlined above is consistent with a model wherein anorthite

in MORB may result from primitive, olivine saturated melt reacting with spinel in depleted material in the uppermost mantle prior to transport into the crustal magma system. As conceived here, this would take place above the melting regime, but below the crust (Figure 17) and would therefore not require primary melting of refractory material at depth. Percolation of magma through this spinel-bearing upper mantle (displaced into the plagioclase stability field in the upwelling asthenosphere) would result in the melt being driven to plagioclase saturation and away from pyroxene saturation (addition of Al, buffered Mg, Ca). Melt could react with spinel-bearing depleted material anywhere in the asthenospheric diapir, and could also react with spinel as it moved through fractures in harzburgite at the base of the crust. This process is similar to the one described by Dick and Natland (1996) for the origin of high alumina and calcic melts capable of producing the An_{99} feldspars they observed in gabbros from ODP Site 895. The major difference was that high-magnesium diopside were also present in the gabbroic segregations they examined, which indicates that those magmas were driven toward pyroxene saturation. Nonetheless, their observations do provide field evidence of a melt reaction at low pressure capable of producing melts that will crystallize high-An feldspar. We suggest that our hypothesis can be tested experimentally. Such experiments could be designed to react primitive liquids with Al-spinel over a range of temperatures, pressures and time. In this way the role of primary refractory melts versus reaction with refractory spinel in anorthite-bearing anhydrous basalts can be examined.

CONCLUSIONS

The results of our experiments indicate that it is possible to experimentally produce anorthite and Fo_{90} saturated primitive basaltic liquids close in composition to naturally occurring lavas. The experimental liquids are also saturated with Al-rich spinel that is similar in composition to spinels observed in naturally occurring anorthite megacrysts (Fisk et al., 1982; Allan et al., 1989; Dick, 1989; Sinton et al., 1993). This association suggests the possibility that primitive MORB basalts are high-An plagioclase saturated due to continued reaction with the upper mantle above the melting regime. Such a reaction of the rising basaltic magma with the spinel in the depleted upper mantle at depths less than 10 kb would drive the magma toward saturation with feldspar. In essence, high-An feldspar in MORB may be produced by a buffering reaction at the Sp +

liquid →Fo + An reaction point. Our experiments also indicate that this buffering reaction will result in an average of ~16–26 % crystallization for each percent decrease in MgO. These data suggest primitive MORB lavas (>8% MgO) have undergone ~62–77% fractionation and reaction with the uppermost mantle and lower crust before eruption.

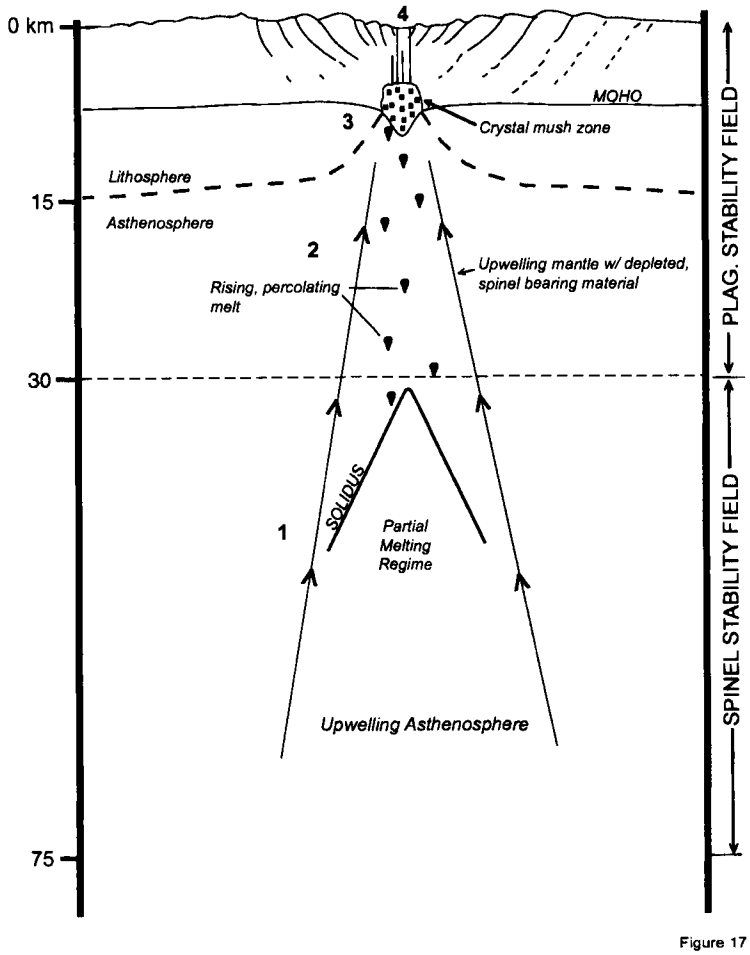

Figure 17

Figure 17: Possible scenario for the petrogenesis of anorthite bearing MORB. 1) Mantle upwelling leads to partial melting of lherzolite, producing a primitive melt. 2) Rising melts percolate through upper mantle, including spinel bearing residual mantle that is displaced into plagioclase stability field by upwelling. Melt reacts with Al-spinel and is driven towards plagioclase saturation. This can occur anywhere below the base of the crust, including fracture channels in harzburgite 3) Melt (now Al-rich due to reaction with spinel) accumulates prior to eruption in crystal mush zone/ conduit system below ridge. High-An phenocrysts form as crystallization proceeds along anorthite/fosterite cotectic. 4) Anorthite bearing MORB is erupted.

MELT INCLUSION FORMATION MECHANISMS AND COMPOSITIONAL EFFECTS IN HIGH-AN FELDSPAR AND HIGH-FO OLIVINE IN ANHYDROUS MAFIC SILICATE LIQUIDS

Edward Kohut
Roger L. Nielsen

This ms submitted to Contributions to Mineralogy and Petrology

In press

ABSTRACT

Important aspects of melt inclusion formation and potential compositional effects have been addressed through a series of experiments using anorthite and forsterite saturated anhydrous mafic liquids. Experimental charges were cooled from 1300° to 1230° and 1210° C at rates of 1°-10°/min., followed by 0-24 hours isothermal periods. Hopper and skeletal crystal morphologies with variable degrees of completeness developed during the cooling periods and isothermal periods <6 hours. Planar overgrowth of these textures during the longer isothermal periods led to the formation of inclusions, the majority of which formed after 6 hours isothermal run time. We suggest that the change in morphologies is related to a decrease in growth rates and changes in dominant growth mechanisms. In general, inclusion compositions were uniform and similar to the host glass, indicating that with the isothermal times required for most inclusions to form, a boundary layer was not entrapped that could be detected within the limits of our analyses.

INTRODUCTION

Glass inclusions in minerals are commonly presumed to represent entrapped samples of the melt from which the mineral formed (Anderson and Wright, 1972; Anderson, 1974; Watson, 1976; Roedder, 1984). Melt inclusions within early forming phenocrysts in lavas, are proposed to trap unmodified parental melts. High-An plagioclase and olivine phenocrysts in basalts commonly host melt inclusions that are preserve information on the diversity of mantle-derived parental magmas (Sobolev and Shimizu, 1993; Sobolev, 1996; Saal et al., 1998; Nielsen et al., 1995; Sisson and Bronto, 1998; Sours-Page et al., 1999, 2002; Gaetani and Watson, 2002). The observed diversity of these primitive magmas as a function of the level of differentiation can tell us much about the nature of early differentiation processes (Sours-Page et al., 1999).

Plagioclase phenocrysts >An_{90} that are common in MORB lavas can contain large numbers of melt inclusions, up to several hundred in a single 1 cm phenocryst (Sinton et al., 1993; Nielsen et al., 1995; Johnson et al, 1996; Sours-Page et al., 1999). These inclusions contain melts that are more Mg-rich than any reported MORB glass, and in many cases their major element compositions are consistent with a parental relationship with the host lava(Nielsen et al., 1995; Sours-Page et al., 1999). However, some inclusions in N-MORB phenocrysts are anomalously depleted or enriched in some major, minor or trace elements (Sinton et al., 1993; Nielsen et al., 1995; Saal et al., 1998; Sours-Page et al., 1999). For example, in a single sample from the Gorda Ridge, Nielsen et al. (1995) observed that La/Sm and Ti/Zr ratios in plagioclase-hosted melt inclusions that range from <0.25 to 0.83 and from 90 to 1600 respectively, while the Mg#s of the glass remained constant at 70-72. Sours-Page et al. (1999) report plagioclase hosted melt inclusions from N-MORB lavas of the Juan de Fuca Ridge that vary in K_2O contents from 0.01 to 0.4 wt% and Ti/Zr ratios ranging from <100 to 1300. Further examples are provided in a detailed description of compositional diversity in MORB high-An feldspar melt inclusions by McNeill and Danyushevsky (1996). The presence of such depleted, high Mg# melt inclusions in plagioclase phenocrysts has been interpreted to result from the entrapment process (Danyushevsky et al., 2002).

Before melt inclusion compositions can be interpreted, alternative means of producing such compositional diversity must be considered. We must establish whether

this variability reflects actual diversity in the melt, or results from either the entrapment process or post-entrapment modification. While the composition of some melt inclusions may be influenced by either mineral-melt reaction (Nakamura and Shimikita, 1998) or by diffusional processes (Michael et al., 2002), modification due to entrapment the not been adequately addressed.

While fluid and silicate melt inclusion formation have been examined experimentally (e.g. Bodnar and Sterner, 1984; Student and Bodnar, 1996, 1997, 1999), these studies did not address specific primary melt inclusion formation mechanisms for plagioclase in mafic liquids. Primary inclusions (i.e. those that form while crystals are growing) in high-An feldspar may reasonably be expected to develop from irregularities in crystal morphology (Roedder, 1984). Experiments on plagioclase morphology have been conducted by Lofgren (1974), Corrigan (1982), and Muncill and Lasaga (1987, 1988), but these workers did not make a specific connection between morphology and melt inclusion formation. Melt inclusion formation experiments for plagioclase performed by Nakamura and Shimikita (1998) were able to produce secondary inclusions, or those formed by dissolution followed by new growth. In these experiments, An_{59} seed crystals were added to a hydrous melt in equilibrium with more calcic plagioclase, and it was observed that a reaction zone formed melt channels in the phenocrysts that were closed off by subsequently recrystallized feldspar. However, this work is not relevant to issues related to primary plagioclase-hosted inclusions formed during crystallization under anhydrous conditions. Furthermore, no satisfactory mechanism has been proposed for the bands of inclusions observed in plagioclase phenocrysts (Roedder, 1984).

In this paper, we describe a series of experiments to primarily investigate mechanisms for melt inclusion formation in high-An plagioclase in MORB. These experiments were designed to determine whether:

a) Primary melt inclusions will form during crystal growth, during either constant cooling or subsequent isothermal crystallization.
b) Inclusions formed in such a manner trap a liquid representative of the host melt.
c) In the case of anorthite, the specific mechanism responsible for the abundant inclusions can be determined.

Anorthite was chosen due to its widespread presence in basaltic lavas and the common occurrence of large numbers of melt inclusions in the mineral in naturally occurring lavas. MORB liquids in equilibrium with high-An feldspar are also saturated in high-Fo olivine (Sinton et al., 1993; Nielsen et al., 1995) and thus lie on the anorthite/forsterite cotectic of the basalt ternary (Osborn and Tait, 1952). For this reason we have configured our experiments to be in equilibrium with both minerals. This has additional benefit in that it also allows us to observe melt inclusion formation in olivine.

Our experiments were run in capsules fabricated from An_{92} feldspar to achieve anorthite saturation and Fo_{92}olivine crystals were added to ensure forsterite saturation. Glass separated from lava sampled from the Gorda Ridge (D9-2 Davis and Clague, 1987) was used as the starting material. Run temperatures of 1230° and 1210° C were chosen as these were found to be favorable for producing An>85 feldspar and high Fo olivine in the liquid in our previous phase equilibria experiments (Kohut and Nielsen, 2003). Although these earlier experiments provided compositional data on the melt and mineral phases, they were not configured to examine the dynamic effects of undercooling and cooling rate.

THEORY

Roedder (Chapter 2-1984) defined inclusions that are formed by crystal growth around and enclosing a surface imperfection as primary inclusions, and described six formation mechanisms. These are: rapid dendritic growth covered by solid growth; partial dissolution yielding a re-entrant that is covered by renewed growth; inclusions trapped in growth spirals; subparallel growth of crystal blocks along fractures resulting in imperfect growth and inclusions; and a foreign object on the surface that becomes a solid inclusion that may entrap liquid with it. Secondary inclusions were described as those that develop after crystallization of the bulk of the host. The compositions of melt trapped in secondary inclusions by definition do not reflect parental melt compositions in equilibrium with the host crystal.

Crystal morphologies are functions of the controls on crystal forms, which are dominated by the growth rate of the crystal and the diffusion of rejected components away from it (Lofgren, 1974; Donaldson, 1976; Philpotts, Chapter 12-1994). The diffusion of rejected components away from the growing crystal is determined by Fick's

first law, which states that the rate of diffusion at any one time is controlled by the concentration gradient and the diffusion coefficient:

$$J_i = -D(\partial c_i/\partial s)$$

Where *Ji* is the flux of element *i*

D is the diffusion coefficient

$(\partial c_i/\partial s)$ is the concentration gradient of element i over dimension s

For basaltic magma, the bulk diffusion coefficient was derived from the Stokes-Einstein equation by Muller and Saxena (p. 268-270-1977) as:

$$D = kT/\eta\lambda$$

Where *k* is Boltzman's constant (1.38×10^{-23} JK^{-1})

T is temperature in Kelvins

η is the viscosity (~$10^{2.8}$ poise at 1573 K, 10^3 at 1500 K)

λ is the characteristic interatomic distance (10^{-8} cm)

The temperature dependence of diffusion coefficients can also be described by an Arrhenius equation:

$$D = D_o exp(-Q/RT)$$

Where D_o (distance^2/s) is D at 1/T=0

Q is the activation energy (J/mol)

R is the gas constant (8.314 J/K mol)

T is temperature in Kelvins

The Arrhenius relation shows that the effects of diffusion on crystallization and the formation of a boundary layer are compositionally dependent as well. The values of D_o and Q have been determined for many cations of interest through several media. The specific diffusion coefficients for cation species within a liquid can vary over several orders of magnitude, for example Ca in basalt has a D_o of 3.98×10^{-5} m^2/s, while the D_o for Na is 5×10^{-10} m^2/s (Freer, 1981). The temperature dependence of diffusion means that during undercooling, as T decreases, J decreases as well. Consequently, a boundary layer of rejected components (elements other than the equilibrium amounts of Ca, Na, Al, and Si needed for plagioclase growth and Mg, Fe and Si for olivine) forms around the

growing crystal. The more rapid the rate of cooling, the more difficult it would be for diffusion to supply the necessary elements and remove the rejected ones.

In addition, as a mineral crystallizes, it must release the latent heat of crystallization into the surrounding liquid (Hibbard, 1995; Muncill and Lasaga, 1988). With small amounts of undercooling, the crystal growth rate is limited by the surface nucleation on the crystal face and diffusion is sufficient to remove molecules rejected by crystal growth (Lofgren, 1974; Philpotts, 1994). Crystals formed when the amount of undercooling is low would be small and simple, but complete crystals with more equilibrium morphologies, which in the case of plagioclase would be tabular and equant crystals. With continued undercooling, the temperature of the melt constantly decreases and thus more heat can be transferred more rapidly into melt. The zone of rejected material surrounding the crystal boundary also increases. For growth to continue, the crystal must form a projection into the liquid to reduce latent heat and to penetrate the boundary layer (Philpotts, 1994). In these circumstances, growth rate exceeds the rate of diffusion of components rejected during growth (Lofgren, 1974), leading to the development of elongate crystals with varying degrees of incompleteness.

In the case of plagioclase, the release of latent heat through an increasing boundary layer is more efficiently accomplished by rapid growth preferentially along the *a* crystallographic axis (Muncill and Lasaga, 1988). As cooling progresses, the amount of undercooling increases and growth begins to increase parallel to the *a* axis. Such increased growth leads to tapering structures that are projection of the crystal sides, producing the swallowtail structure. Continued growth of the projections gives rise to skeletal crystals. The hoppers may result from supersaturation at the corners of the crystals as rapid growth that concentrates the cations needed for growth in those locations. This has the effect of producing enhanced stepwise growth that forms boxy embayments.

METHODS

Phenocrysts of An_{93-96} plagioclase from Arenal Volcano in Costa Rica were used for our experimental capsules. These were cut into ~1 cm cubes and a hole ~2 mm in diameter and 3 mm deep was drilled into each capsule to hold the starting powder. The starting powder consisted of ground glass sampled from a Gorda Ridge N-MORB lava

(D9-2 – Davis and Clague, 1987). Kilbourne Hole olivine (Fo_{91-92}) was added to ensure olivine saturation. In earlier experiments that used capsule fabricated from feldspar from a different source, the glass in the run products commonly infiltrated into the capsule through fractures and was difficult to distinguish from pre-existing natural glass. Because of this problem, 0.1 wt% ZrO_2 was added to distinguish the products of our experiment from glass derived from the capsule. However, this precaution proved unnecessary, as the glass in the run products remained confined to the hole in the Arenal capsules. The charges were suspended by 0.1 mm platinum wire in a Deltec vertical quench furnace and the oxygen fugacity was set at the QFM buffer using a mixture of H_2 and CO_2 gasses. The experimental charges were held at an initial melting temperature of 1300°C for two hours to saturate the melt in anorthite and fosterite. The temperature was then dropped at cooling rates of 1°/min, 5°/min and 10°/min to run temperatures of 1210° and 1230° C, or ΔTs of 90° and 70°. These run temperatures were chosen because observations of run products during phase equilibria experiments (Kohut and Nielsen, 2003) showed that equilibration temperatures of 1210° and 1230° (70° -90° ΔT) were the most suitable for producing melts in equilibrium with high-An feldspar and high-Fo olivine, and the crystals in the run products from these experiments also contained melt inclusions. For a ΔT of 90°, the isothermal run periods were zero hrs and six hrs. For a ΔT of 70°, the run periods were 0 hrs, 1 hr, 3 hrs, 6 hrs and 24 hrs. An additional experiment at 1230°C was run for 116 hrs with a cooling rate of 1°/min. At the end of isothermal run time, the experiments were dropped quenched in water.

Run products were analyzed with the Cameca SX-50 electron microprobe at Oregon State University using a beam current of 30nA for glass and feldspar, and 50 nA for olivine and an accelerating voltage of 15kV. For glass, count times were 30s for Fe, 20s for Mg, Al, Si, P, K, Ti and Zr, and 10s for Na, Ca, Cr, and Mn. For feldspar, count times were 10 seconds for all elements. For olivine, count times were 20s for Fe and Ni, and 10s for Mg, Al, Si, K, Ti, Na, Ca, Cr, and Mn. The basalt glass standard (USNM 113498/1 VG-A99) was run as an unknown and calculations of relative error were performed using measured-true/measured*100. These calculations indicated glass analyses were accurate within ±0.51% for SiO_2, ±0.05% for TiO_2, ±0.25% for Al_2O_3,

±0.17% for FeO*, ±0.03% for MnO, ±0.16% for MgO, ±0.19% for CaO, ±0.16% for Na_2O, ±0.04% for K_2O and P_2O_5.

We used the method of crystal size distribution to estimate growth rates of our crystals. This method is an empirical statistical technique used to determine the nucleation and growth rates of phases precipitating from a solution. We will only describe the procedure briefly here, full discussions of theory and applications to geologic problems are presented by Marsh (1984), Cashman and Marsh (1984), Cashman (1988), Cashman and Ferry (1988), Mangan (1990), Cashman (1993), Higgins (2000) and Garrido et al (2001). The population density (n) is the number of crystals per unit size per unit volume, and is estimated from the slope of the distribution curve dN/dL, where N is the cumulative number of crystals for each increasing size interval or bin (L). Typical CSD diagrams plot the crystal size interval or bin (L) versus the natural logarithim of the crystal population density (n) for each bin. The growth rate can be estimated from the slope of the CSD trend described by the data using the relation:

$$m = -1/Gt$$

where m is the slope,

G is the growth rate

t is the crystallization time.

The intercept of the trend is the nucleation density (n^o) which can be used to calculate the nucleation rate (J) by:

$$J = n^o G$$

This rate has units of number-distance^3/s.

To perform CSD analyses, crystal lengths were first measured from backscattered electron images (at magnifications of 200-400x) of the run products using the measuring tool in the NIH IMAGE software (available at http://rsb.info.gov/ij/index.html). The accuracy of measurements was a function of image resolution, which affected the ability to distinguish crystal edges. We determined that the edges could be resolved within 2-4 pixels, which corresponded to 0.5-1 μm. Crystal lengths were then corrected to 3-D lengths with the stereological method of Higgins (2000) using his CSD correction software (downloaded from http://wwwdsa.uqac.uquebec.ca / ~mhiggins/csdcorrections.html). The software was then used to produce to determine the

volumetric population density, n_v, with the bin size being determined automatically and the number of bins per decade adjusted to provide the smoothest curves. The data were then plotted and linear regressions used to obtain the slope. Trial runs that added or subtracted the small measuring error (described above) did not produce noticeable changes in CSD results.

TERMINOLOGY

We use the following terms in this paper to describe the morphology of plagioclase and olivine crystals. With the exception of the term intergrown texture for olivine, these morphologic definitions are modified from those used for plagioclase by Lofgren (1974) and for olivine by Donaldson (1976). In all experiments, more than one morphology for each mineral phase was observed. However, there were one or two predominant morphologies and these are the ones noted in Tables 1.

Plagioclase morphology:

Swallowtail (A-Figure18)- tabular crystals with tapering, bifurcated ends. Simple swallowtails may have two tapering projections from either one or both ends while more complex swallowtails may have multiple or very elongate projections or have a fan shape.

Skeletal (B-Figure18)- incomplete, enlongate crystals. Commonly have hollow cores with complete or nearly complete outer faces or an irregular, tapering outline.

Hopper (C and D-Figure18)- preferential growth from corners that results in a boxy cellular texture that includes indentations or hoppers in the crystals outer surface. This morphology is commonly observed in two dimensions as hook-shaped features. Simple hoppers appear as skeletal crystals with enhanced corner growth. Blocky hoppers show a combination of planar and hopper morphology. Complex hoppers have multiple re-entrants and a variety of forms, from angular to a combination of angular and rounded surfaces. Stepwise growth may also form hoppers along very large crystals or the capsule wall.

Equant and Tabular (E-Figure 18)- euhedral crystals that are equal or near equal in each direction are equant. Tabular crystals are elongated on one axis relative to the others. Inclusions may be present.

Olivine morphology:

Granular (Figure 19a)- anhedral, and subspherical crystals. Either complete or with round, oval or lobate inclusions.

Hopper (Figure 19b)- combination of planar faces, smooth curvilinear lobes and re-entrants. May be complete or highly skeletal. Simple hoppers are granular crystals with curvilinear or planar lobes or C-shape crystals. More elongate hoppers have a hook shape, while complex hoppers have multiple lobes, embayments and a variety of curvilinear and planar faces.

Polyhedral- euhedral equant or tabular crystals with planar faces. This may be either solid or with small inclusions.

Intergrown- small, ~5-15 m anhedral olivine intergrown with plagioclase.

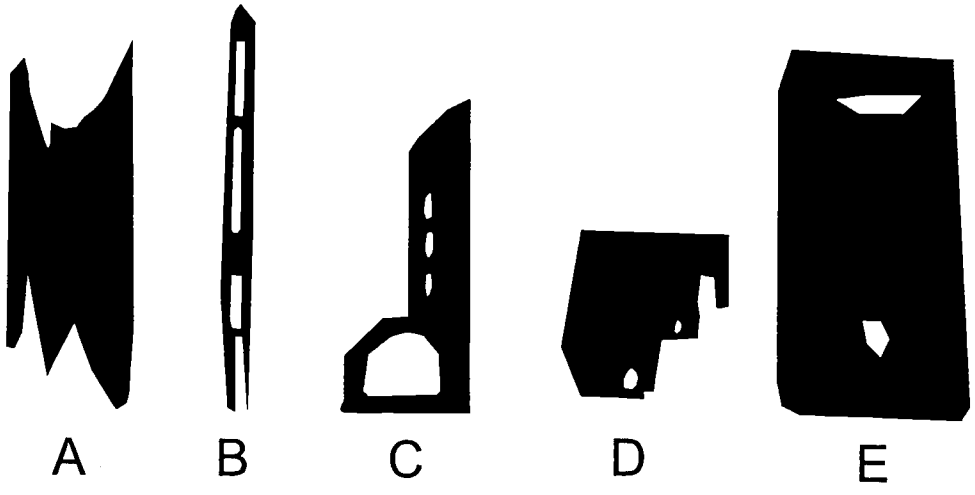

Figure 1

Figure 18: Drawings based on backscattered electron images for representative plagioclase morphologies. A-swallowtail, B-skeletal, C-simple hopper growing from skeletal crystal, D-blocky hopper with inclusions, E- tabular crystal with inclusions. See text for explanation.

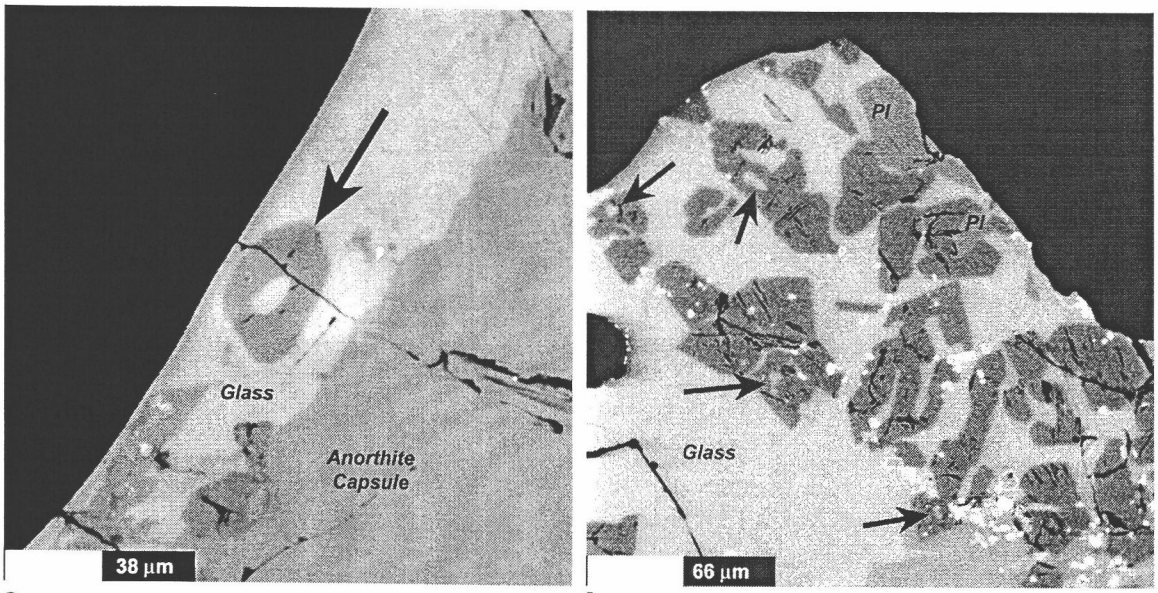

a. b.

Figure 19: (a. left) Backscattered electron image of granular olivine with central inclusion (arrow). **(b. right)** Backscattered electron image of a wide variety of olivine (dark gray) hopper crystals in the quenched run products from experiment with 1°/min. cooling to 1230° C (70° ΔT) and 6 hours isothermal period. Light gray crystals are plagioclase (Pl) and small white rounded objects are chromites. Note that several olivines host inclusions (arrows).

RESULTS

Crystal Morphology

Plagioclase

Feldspars that grew during cooling had skeletal and swallowtail morphologies, and these were more elongate and incomplete following cooling to 90° ΔT than to 70° ΔT . We observed a progression in plagioclase morphology from swallowtail and skeletal, to hopper followed by equant and tabular forms with increasing isothermal run time. (Table 8). Multiple forms were common in each experiment, and the occurrence of morphologies in the sequence overlapped. Duplicate cooling rate experiments to 70° ΔT produced similar textures. In experiments quenched at 6 hours isothermal time, feldspars in the melt were predominately hoppers and there were stepwise growths of feldspar on the capsule rim. These feldspar hoppers were best developed in experiments that had 5°/min. cooling (Figure 20a). At an isothermal period of 24 hours, feldspars were blocky hoppers and tabular crystals with small inclusions (Figure 20b). These morphologies were similar to those we observed in our phase equilibria experiments, which had run times of 24 hours. As the isothermal run time increased, inclusions rather than open

embayments were observed. This coincides with the progression from incomplete morphologies to those with planar faces, and indicates that embayments were enclosed as crystallization progressed. The one experiment with 116 hours isothermal time followed 1°/min. cooling and produced a few large (~203-358 x 50-85 μm) feldspar and olivine (~460 x 350 μm) crystals and smaller blocky feldspars.

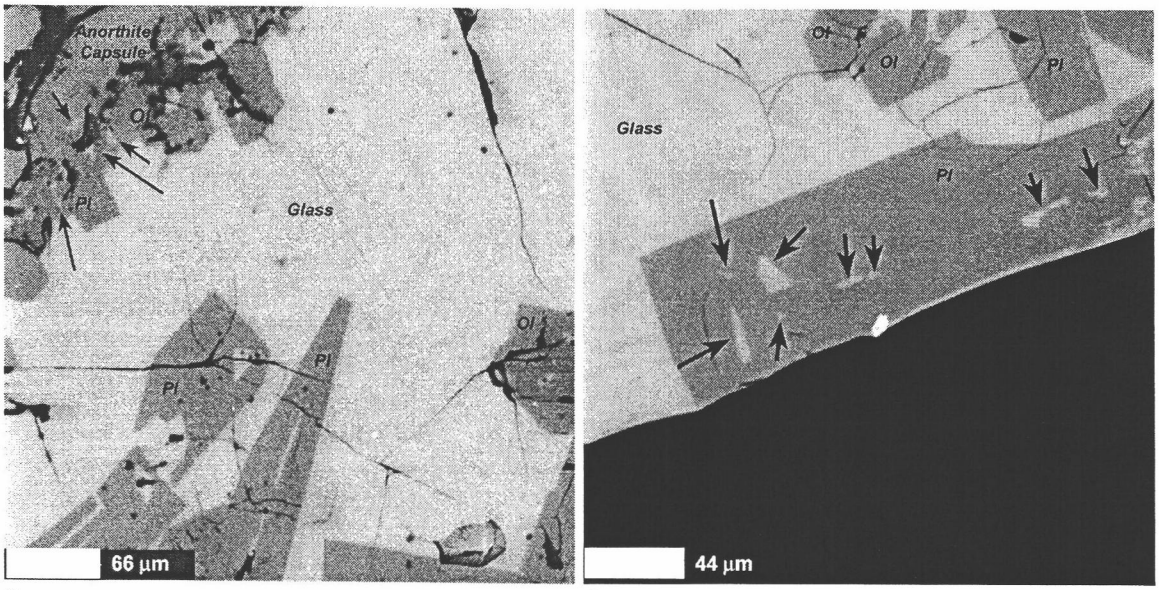

a. b.

Figure 20: (a. left) Backscattered electron image of plagioclase (Pl) hoppers in the quenched run products from an experiment with 5°/min. cooling to 1230° C (70° ΔT) and 6 hours isothermal period. Hoppers occurred both as free-floating crystals in the liquid and as overgrowth on the anorthite capsule rim. Note band of inclusions (arrows) in rim overgrowth. Growth of similar hoppers on natural feldspars may form the bands of inclusions observed in many plagioclase phenocrysts **(b. right)** Backscattered electron image of tabular plagioclase (Pl) containing melt inclusions (arrows). Experiment cooled at 10° /min to 70° ΔT (1230° C), held for 24 hours and quenched. We propose that such crystals initially developed hopper and skeletal morphologies during undercooling and isothermal crystallization of 6 hours or less. Growth became planar as isothermal crystallization progressed, and planar overgrowth trapped melt in embayments in the initial hopper and skeletal morphologies.

Olivine

As indicated by the lack of olivine in the run products from the cooling only experiments (i.e. 0 hours isothermal period), olivine did not nucleate during the cooling period and was not observed in any experiments with less than 6 hours isothermal time, except for the 3 hour experiment with 10°/min. cooling to a ΔT of 70°. Olivine morphology changes from granular to hopper to intergrown and polyhedral as the

Table 8. Plagioclase Morphology

ΔT=90°			
Run Time (hrs)	1°/min.	5°/min.	10°/min.
0	skeletal/complex swallowtail	simple swallowtail/tabular*	tabular-equant*
6	blocky hopper	skeletal	tabular/hopper
ΔT=70°			
Run Time (hrs)	1°/min.	5°/min.	10°/min.
0	simple swallowtail	skeletal/tabular	tabular/swallowtail
1	swallowtail/skeletal	skeletal	tabular/swallowtail
3	skeletal	skeletal/hopper	swallowtail/skeletal
6	skeletal/blocky hopper	complex hopper/skeletal	blocky/complex hopper
24	complex hopper/tabular*	tabular-equant*	blocky hopper
116	tabular-equant*/hopper	-	-

Olivine Morphology

ΔT=90°			
Run Time (hrs)	1°/min.	5°/min.	10°/min.
0	no olivine	no olivine	no olivine
6	simple, C-hopper	hook-hopper	intergrown
ΔT=70°			
Run Time (hrs)	1°/min.	5°/min.	10°/min.
0	no olivine	no olivine	no olivine
1	no olivine	no olivine	no olivine
3	no olivine	no olivine	hook, C-hopper/granular
6	granular/hopper	granular	granular/hook-hopper
24	intergrown/polyhedral***	hook and complex hopper	simple hopper/polyhedral*
116	polyhedral/simple hopper	-	-

*crystals have incipient hopper features
**tabular and/or equant crystals hosting inclusions
***inclusion hosting

isothermal increased past 6 hours (Table 8). We observed that the occurrences of granular and simple hopper morphologies in olivine overlapped. The hopper forms were similar to those described by Faure et al. (2003) for similar cooling rates and degrees of undercooling. The granular crystals are similar to polyhedral crystals produced by Faure et al. (2003) in the respect that their polyhedral crystals also commonly contained central inclusions. Complex hoppers were also observed that were similar to those described by Jambon et al. (1992) for 71° ΔT. It is probable that some granular crystals initially formed as C-shape hoppers in which the embayment became enclosed as planar, surface-nucleation controlled growth became dominant with increasing isothermal time.

Crystal Size Distribution and Growth Rate

Growth rates were examined to determine any correlation between morphology and growth rate that would provide evidence for the dominant growth mechanism. These rates were calculated from slopes of the linear regression lines through the CSD data for each experiment. Due to the small populations involved (15-25 crystals of each phase per experiment), the R^2 values for the trends ranged from 0.5278 to 0.9525, with an average of approximately 0.76. The data however was reliable enough to estimate growth rates and make relative comparisons. Growth rates were approximately the same during cooling to both 70° and 90° ΔT, but after 6 hours isothermal run times the rates were slightly slower at 90° ΔT compared to 70° ΔT (Table 9). Plagioclase growth rates were most rapid during cooling and became progressively slower as the isothermal periods increased (Figure 21). For example, plagioclase growth rates during 5°/min. cooling to a ΔT of 70° were 1.00×10^{-2} μm/s, but decreased to 2.01×10^{-3} μm/s by 6 hours isothermal run time, and to 9.1×10^{-4} μm/s by 24 hours. Similar decreases in growth rate with time were observed following 1°/ min. and 10°/min. cooling (Table 9, Figure 21). Overall, plagioclase growth rates were highest following 10°/min. cooling for all isothermal periods. This result corresponds to Cashman's (1993) observation that an increase in cooling rate will lead to an increase in growth rates. Estimated olivine growth rates were fairly constant, but were highest following 10°/min. cooling (Table 9). This implied connection olivine growth rate to cooling rate, despite the lack of olivine nucleation during cooling is addressed in the discussion. More rapid growth rates were associated with incomplete hopper and skeletal morphologies, and the decrease in growth

rates coincided with the change to more planar equilibrium morphologies.

Nucleation rates also decreased with increasing run time, since they are a function of the growth rate. For experiments quenched immediately following cooling, 10°/min. cooling produced the highest nucleation rates, which again corresponds to Cashman's (1993) finding that an increase in cooling rate increased the nucleation rate. Nucleation rates for experiments following 10°/min. cooling were consistently higher for all isothermal periods.

Inclusion size distribution

Inclusion sizes were measured using the same strategy as crystal sizes. To account for the 3-D size of the inclusions and the conversion of area to volume, size distribution data were corrected using the same correction software that we used for CSDs. Although inclusion shapes were variable and commonly asymmetric, most could be approximated as spheres and we had the CSD correction program treat the inclusions as spherical objects. The data produced were used only to compare relative population densities. These were fairly constant from experiment to experiment, although the size distribution in olivine-hosted inclusions was more consistent. The highest population density occurred in inclusions under 10 μm in plagioclase and 5 μm in olivine, (Figure 22). In the 116-hour experiment, the distribution was most heavily weighted towards small sizes. This may indicate that as smooth planar morphologies became more dominant with run time, fewer inclusions were produced and early-formed inclusions decreased in size by crystallization of the host along the inclusion walls. In such circumstances, the largest and most easily analyzed inclusions would be those that formed closest to the end of the experiment run time. An inclusion size decrease might also have resulted in the elimination of the earliest formed inclusions.

Inclusion Frequency

The frequency of inclusion occurrence was estimated by counting the number of inclusions observed in plagioclase and olivine crystals in the run products from each experiment, and the number of inclusions was divided by the total number of crystals observed. Due to the fragility of the capsules, we were not able to section them in a consistent manner and the amount of run product and the orientation of the exposed area varied from experiment to experiment. This introduces an uncertain amount of

Table 9: Growth rates and melt inclusion frequencies

ΔT	Cooling rate	Isothermal time	Plag. G	Plag. J	Olivine G	# Pl MI / # Pl Xtals	# Ol MI / # Ol Xtals
90°	1	0	1.02×10^{-2}	3.33×10^{-2}	-	0.136	-
90°	5	0	1.09×10^{-3}	4.37×10^{-2}	-	0.235	-
90°	10	0	1.12×10^{-3}	9.11×10^{-2}	-	-	-
90°	1	6	8.80×10^{-4}	7.11×10^{-3}	1.25×10^{-3}	0.462	0.348
90°	5	6	1.20×10^{-3}	5.68×10^{-2}	1.03×10^{-3}	0.559	0.324
90°	10	6	1.43×10^{-3}	7.23×10^{-2}	2.47×10^{-3}	0.467	0.500
70°	1	0	1.16×10^{-2}	8.77×10^{-2}	-	0.238	-
70°	5	0	1.00×10^{-2}	1.36×10^{-3}	-	0.286	-
70°	10	0	1.12×10^{-1}	8.30×10^{-1}	-	0.077	-
70°	1	1	6.45×10^{-3}	2.36×10^{-2}	-	0.222	-
70°	5	1	4.35×10^{-3}	8.92×10^{-2}	-	0.429	-
70°	10	1	1.60×10^{-2}	6.05×10^{-1}	-	-	-
70°	1	3	3.59×10^{-3}	1.07×10^{-2}	-	0.286	-
70°	5	3	2.66×10^{-3}	7.56×10^{-2}	-	0.875	-
70°	10	3	6.58×10^{-3}	1.12×10^{-1}	3.30×10^{-3}	0.375	0.500
70°	1	6	2.39×10^{-3}	1.15×10^{-2}	1.10×10^{-3}	0.750	0.700
70°	5	6	2.01×10^{-3}	6.90×10^{-2}	1.14×10^{-3}	1.182	0.559
70°	10	6	3.88×10^{-3}	2.26×10^{-2}	1.17×10^{-3}	0.700	1.150
70°	1	24	5.69×10^{-4}	4.28×10^{-3}	5.67×10^{-4}	0.800	0.917
70°	5	24	9.10×10^{-3}	1.36×10^{-3}	5.83×10^{-4}	1.091	1.000
70°	10	24	1.07×10^{-3}	7.57×10^{-3}	7.22×10^{-4}	0.957	0.714
70°	1	116	2.04×10^{-4}	4.71×10^{-3}	3.49×10^{-4}	0.889	0.391

Cooling rate - °C/min.
Isothermal time - hours
G - growth rate in μm/s
J - nucleation rate in $\mu m^3/s$

inaccuracy into our frequency estimates. With the limited data we have, the firmest conclusion we can make is that the majority of inclusions formed with 6 hours or more isothermal time.

A ΔT of 70° appeared to be more favorable for inclusion development than a ΔT of 90°, but cooling rate combined with isothermal run time seemed to have exhibited the greatest control on the frequency of melt inclusion occurrence (Table 9). Few

plagioclase-hosted inclusions formed during the cooling period (0 hours isothermal time-Table 9). For all isothermal times, the greatest frequency of plagioclase-hosted inclusions followed 5°/min. cooling and increased with longer isothermal periods, peaking at six hours isothermal run time (Table 9). However, the number of plagioclase hosted inclusions following 1° and 10°/min cooling was greatest with a 24-hour isothermal period. Since only 0 and 6 hours isothermal periods were used for 90° undercooling, the data for this ΔT were less detailed (Table 9).

As noted earlier, no olivine crystallized during the cooling period and with the exception of 3 hours isothermal time after cooling 10°/min. to 70° ΔT, none appeared with less than 6 hours isothermal time. Consequently, the data on olivine-hosted inclusion frequency are limited to isothermal periods greater than 6 hours. With 6 hours, the greatest number of olivine-hosted inclusions followed 10°/min. cooling to both 70° and 90° ΔT (Table 9). Olivine melt inclusion frequencies at 24 hours isothermal time were fairly similar following cooling at all rates.

Host glass, Inclusion, and Mineral Compositions

In general, liquids quenched during isothermal run periods have compositions that fall along trends towards the natural lava suite (Davis and Clague, 1987) for the starting glass and the starting glass itself. The most notable exceptions are from experiments quenched immediately after cooling; liquids quenched thus had the lowest MgO contents (8.18-9.32%) and had compositions off the general trend (Table 10 and 11, Figures 23-25). Al_2O_3 and MgO contents decreased with isothermal time regardless of cooling rate to the run the run temperature, and these data likely reflect the increasing amount of crystallization with increasing isothermal time. Na_2O, FeO* and TiO_2 contents were similar between experiments with greater than 3 hours isothermal time. The CaO contents were lowest in experiments with 6 hours isothermal time following all cooling rates. The 1 and 3 hour experiments (Table 11) also showed compositional departure from the CaO trend of the natural lava suite. These data are the probable result of the system not yet being in chemical equilibrium and consequently the melt was still reacting with the capsule and added olivine. The observation that experiments with less than 6 hours isothermal time had not yet crystallized olivine (except for the 3 hour experiment with 10°/min. cooling)

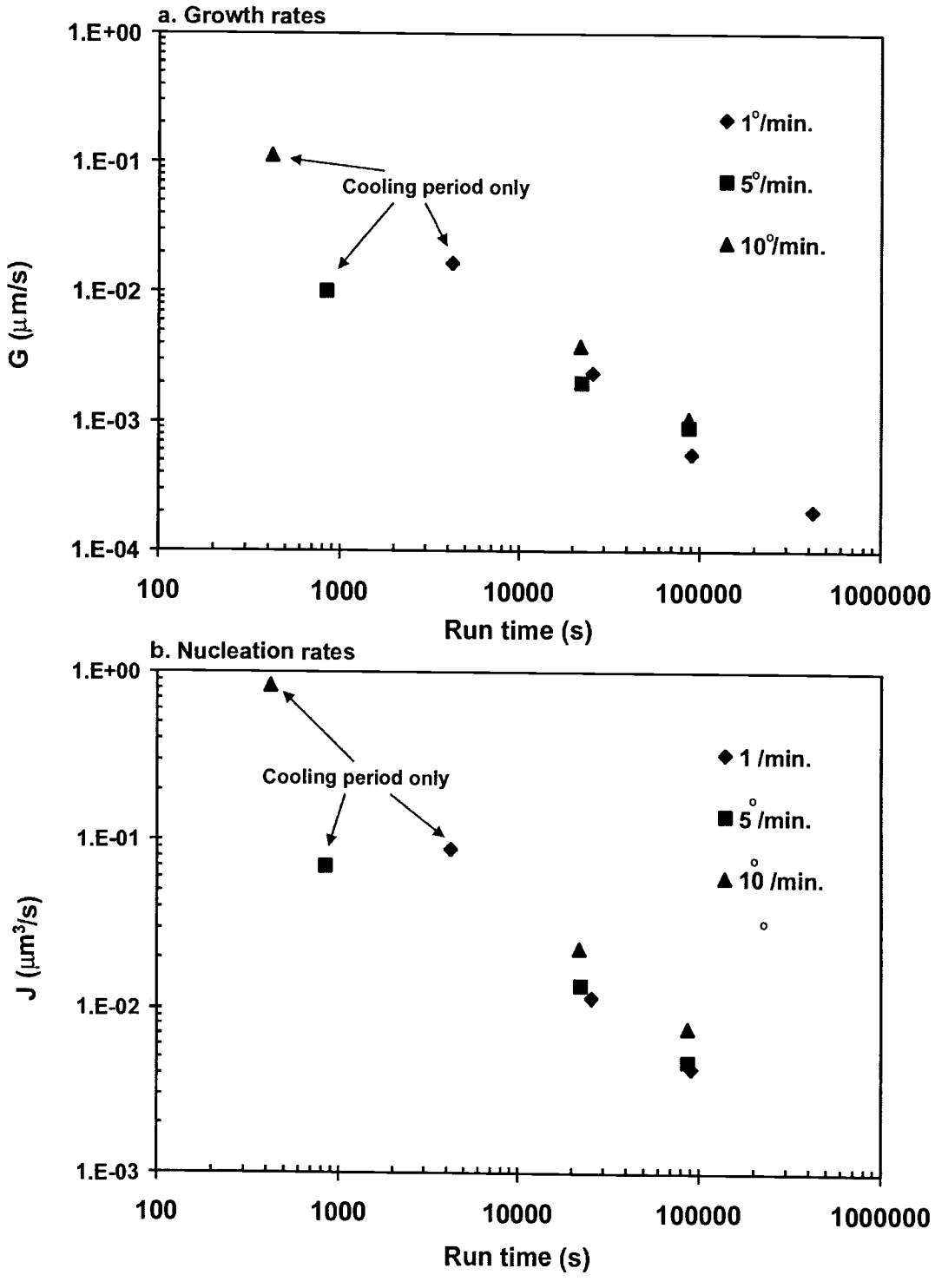

Figure 21: Representative growth and nucleation rates for experiments with 70°ΔT calculated using CSD methods. Run times are the sum of cooling and isothermal times. G was fastest during cooling and decreased with lengthening isothermal period. G and J were highest during 10° /min. cooling. The decrease in G and J coincided with the change to more complete crystal morphologies with smooth, planar faces.

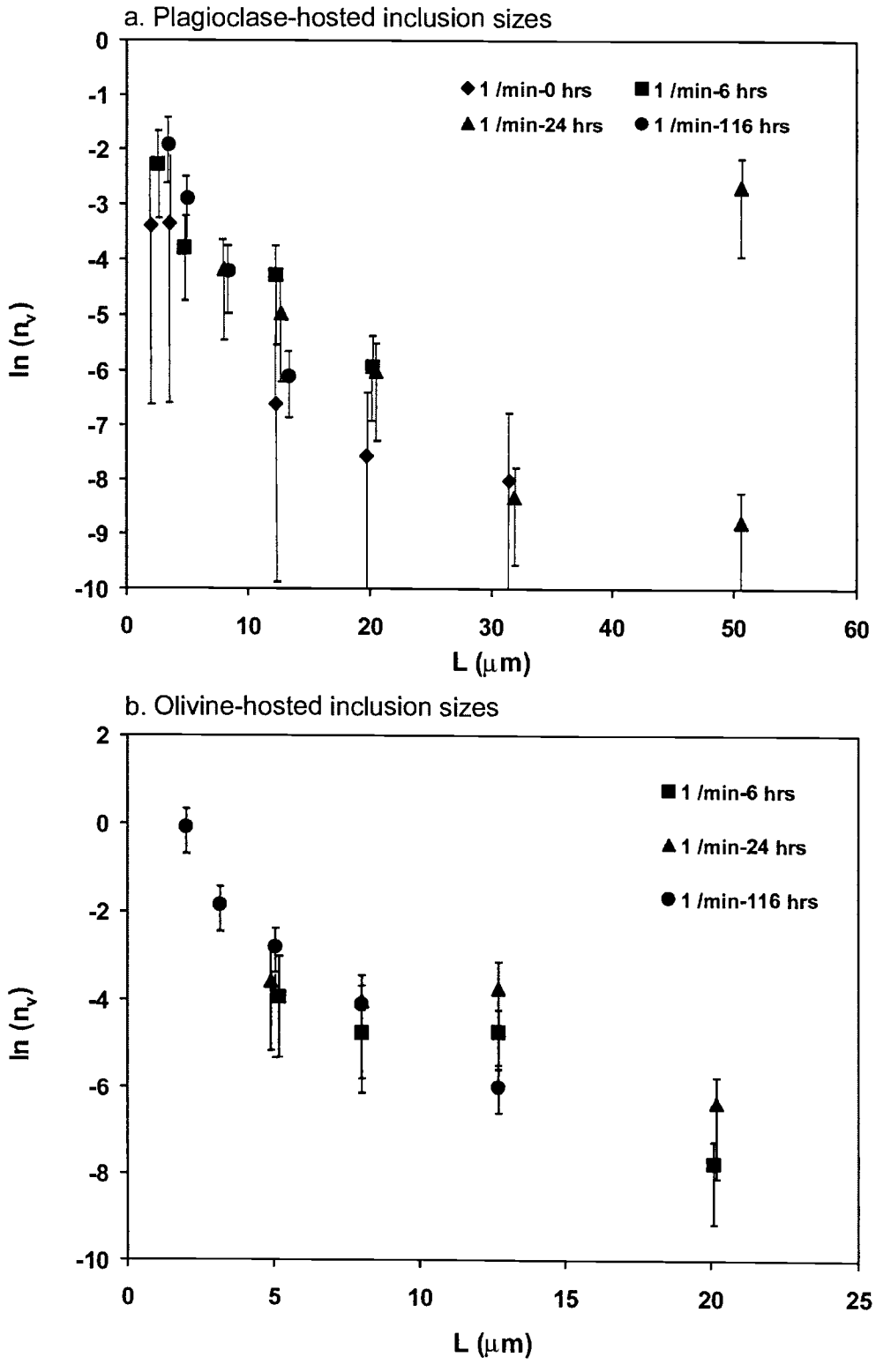

Figure 22: Representative melt inclusion size distributions for experiments with 1°/min. cooling to 70° ΔT. Size distribution curves remained fairly constant and weighted towards smaller inclusion sizes, especially for the 116-hour experiment.

is further evidence that the system had yet to achieve equilibrium and the point of multiple saturation. However, the longer period experiments had more time to equilibrate and the glass compositions of all 24-hour experiments regardless of cooling rate were similar (Figure 23-25). The results of the 24-hour experiments also correspond with the 1230° compositions from our phase equilibria experiments (Kohut and Nielsen, 2003).

Due to the use of a 3 μm beam size for glass analyses, many inclusions were not suitable for EMP analysis. As a consequence, the number of inclusions we have data from (Table 10 and 11) are less than the number of inclusions observed. The average inclusion compositions for an experiment are also identical within 2σ and analytical error to the host glass compositions (Table 10 and 11, Figures 23-25). Slow cooling (1°/min.) produced the greatest difference between average melt inclusion and melt compositions: there is a ~0.5-2% difference in Al_2O_3 contents and 0.2-1.2 % variability in MgO between average compositions of host glass and plagioclase-hosted melt inclusions formed during 1°/min. cooling. This diversity may indicate that inclusions in the slow-cooling experiments entrapped melt over a wider time interval and sampled melt at different stages of equilibration (Table 11, Figure 23).

Even though the amount of compositional difference between host and inclusion compositions was small and within analytical error, it is still possible that what minor diversity there was could be attributed to entrapped rejected components present within a boundary layer surrounding a growing crystal. To test this, we compared the sizes of the analyzed inclusions to their compositions. If a layer were entrapped, we would expect to see systematic increases in rejected components with decreasing inclusion sizes, as the smaller inclusions would contain a proportionately greater amount of the boundary layer. Figure 9 illustrates these comparisons, with CaO and Al_2O_3 representing rejected components in olivine-hosted inclusions and Mg# (at% $Mg/[Mg+Fe^T]*100$) and TiO_2 representing rejected species in plagioclase-hosted inclusions. Although some variability was observed, it was not systematic with size, indicating that the inclusions did not contain discernable boundary layers. Differences between individual inclusion compositions in a given experiment may instead be evidence of melt being entrapment at different stages in equilibration. Note that individual olivine-hosted inclusions from 6- and 24-hour experiments with 5°/cooling had similar Al_2O_3 contents, even

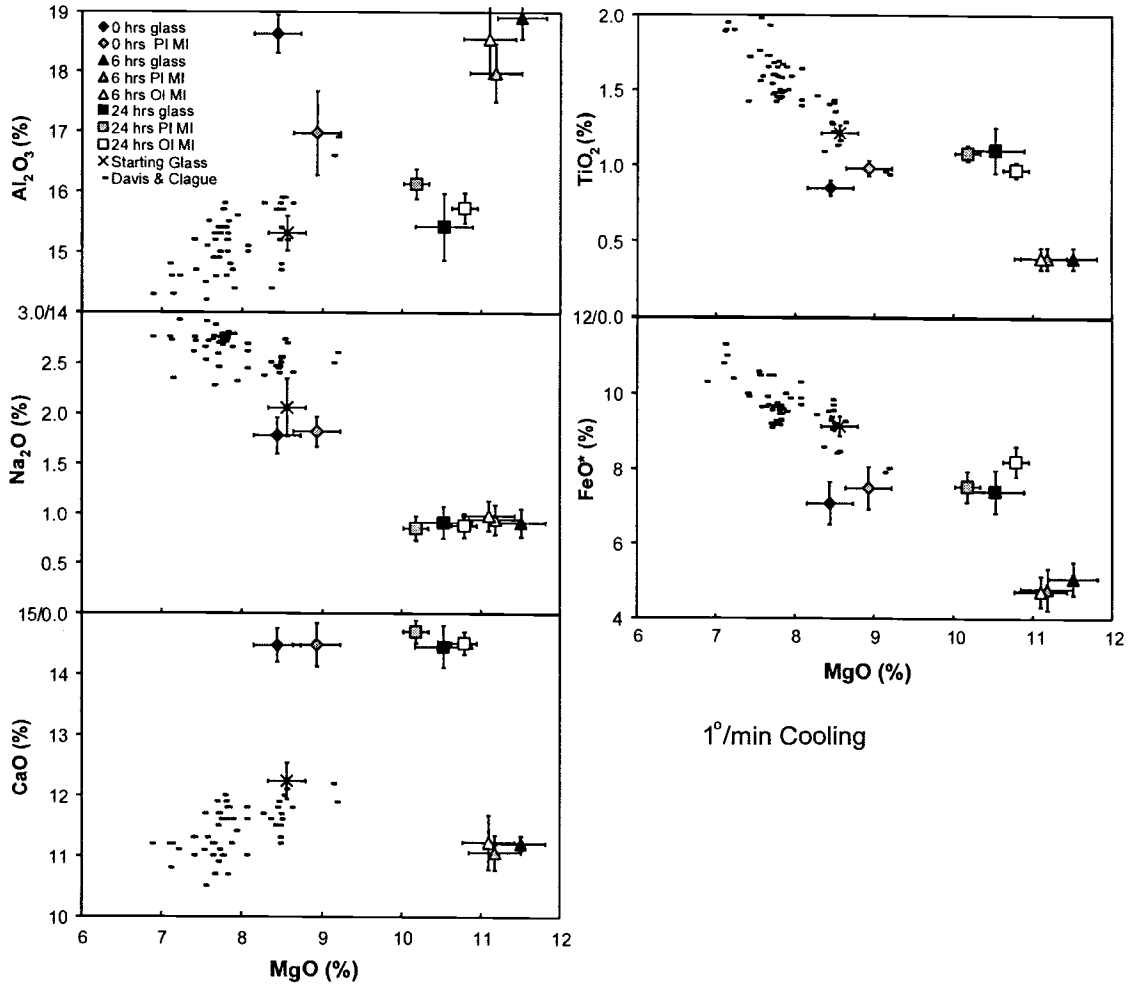

Figure 23 Variation diagram for major elements vs. MgO for representative experiments with 70° ΔT, and 1°/min. cooling. Points are average compositions. Davis and Clague refers to the lava suite from which the starting glass was sampled (D9-2 Davis and Clague, 1987). Error range includes 2σ from average (Table 4) and analytical error (see text).

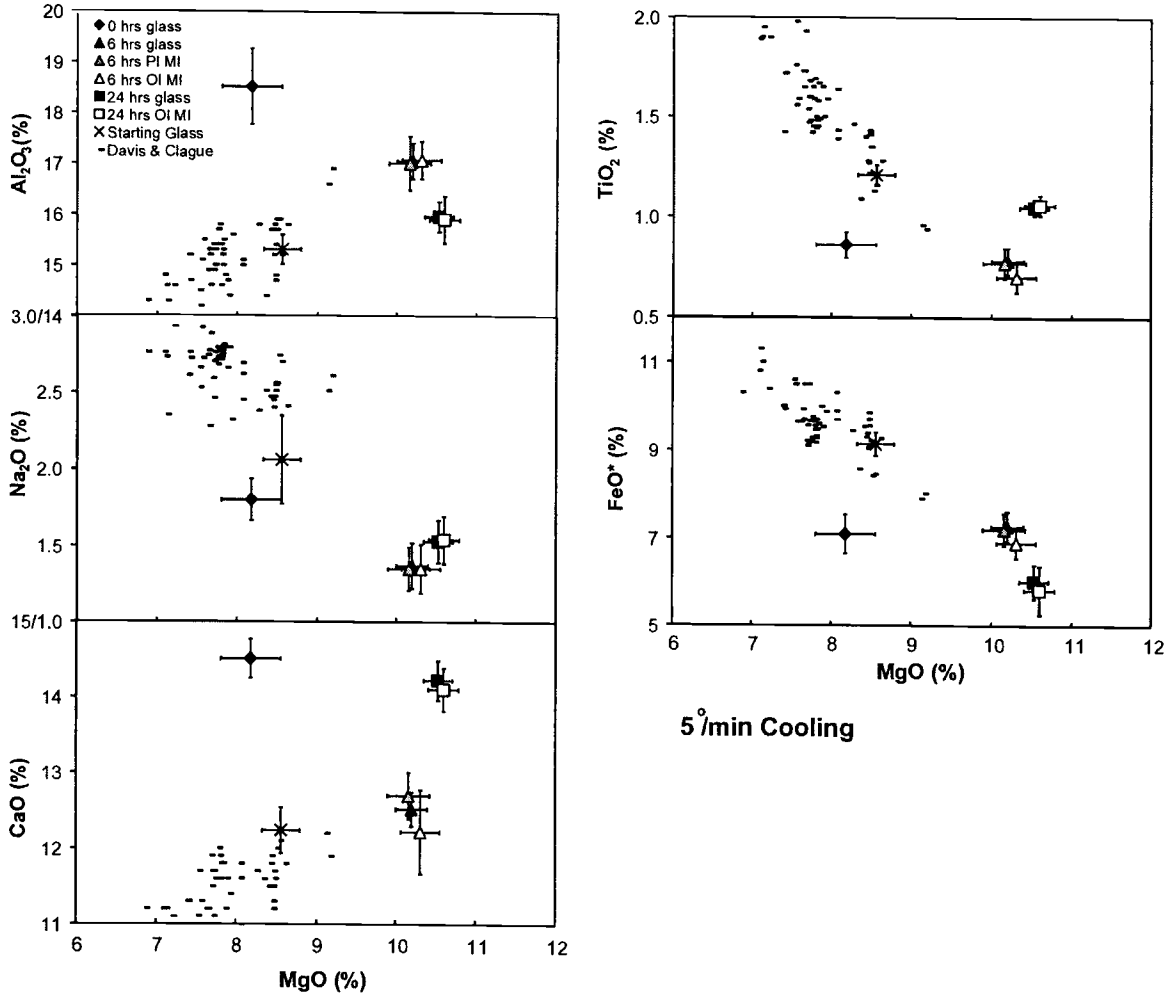

Figure 24: Variation diagram for major elements vs. MgO for experiments with 70° ΔT, and 5°/min. cooling.

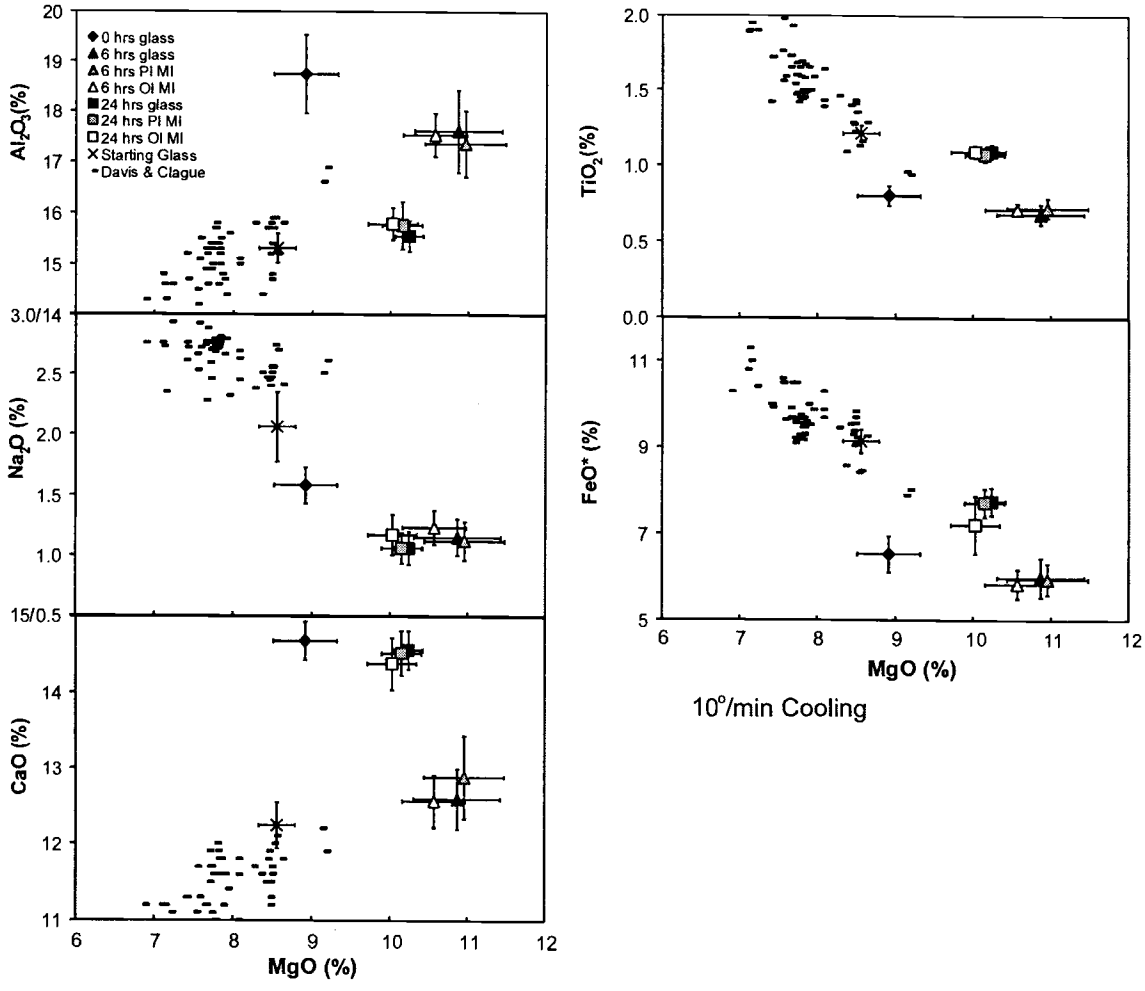

Figure 25: Variation diagram for major elements vs. MgO for experiments with 70° ΔT, and 10°/min. cooling.

though the averaged inclusion compositions from the experiments were dissimilar (Figure 24). Although inclusions<3-4 μm may have indeed contained compositions that reflected the trapping of a boundary layer, these were too small to be effectively analyzed using EMP. Differences in cations needed for growth by the host crystal were not examined relative to inclusion size due to the uncertainty that could result from the electron beam exciting the same elements in the host crystal, especially in the smallest inclusions. Although such errors would be small, they would be difficult to distinguish from the variability we would be attempting to determine.

The feldspars that crystallized in the run products overall ranged from $An_{83.5\text{-}97.1}$ and the olivines were $Fo_{89.6\text{-}93.8}$ (Table 12). Within each experiment, plagioclase compositions

were the most variable. The largest feldspars that crystallized during the cooling period or during shorter isothermal periods had 1-5 μm zones of lower An content surrounding a higher An core (Table 12). Zoning was not prevalent in feldspars in experiments quenched after 1 hours isothermal time following 1°/min. cooling, after 3 hours 10°/min. cooling. The predicted An content of feldspars in equilibrium with the liquid composition from each experiment was calculated using Equation 1 from Panjasawatwong et al., (1995) and with the Petrolog software program (available at http://www.geol.utas.edu.au/~leonid/Petrolog.html) using the Danyushevsky model and compared to the observed An contents (Table 12, Figure 27). The results suggest that the feldspars that were not in equilibrium (as calculated) with the melt at quench time were also those with incomplete hopper and skeletal morphologies. With longer isothermal times, the prevalence of zoned feldspars diminished and most had overall An contents that were close to equilibrium values.

The compositions of the olivines in the run products were consistently similar to the olivine in the starting material (Fo_{91-92}) and range from $Fo_{89.6-93.8}$ (Table 12). Within each experiment, olivine composition varied only 0.3-0.75 Fo. Chrome spinels were also present in the run products, with Cr#s (at% Cr/[Cr+Al])of 0.32-0.41 and Al_2O_3 contents of 30.0-36.5 wt% . The presence of spinel indicates that liquid was three-phase (olivine, plagioclase, chromite) saturated at the run temperatures.

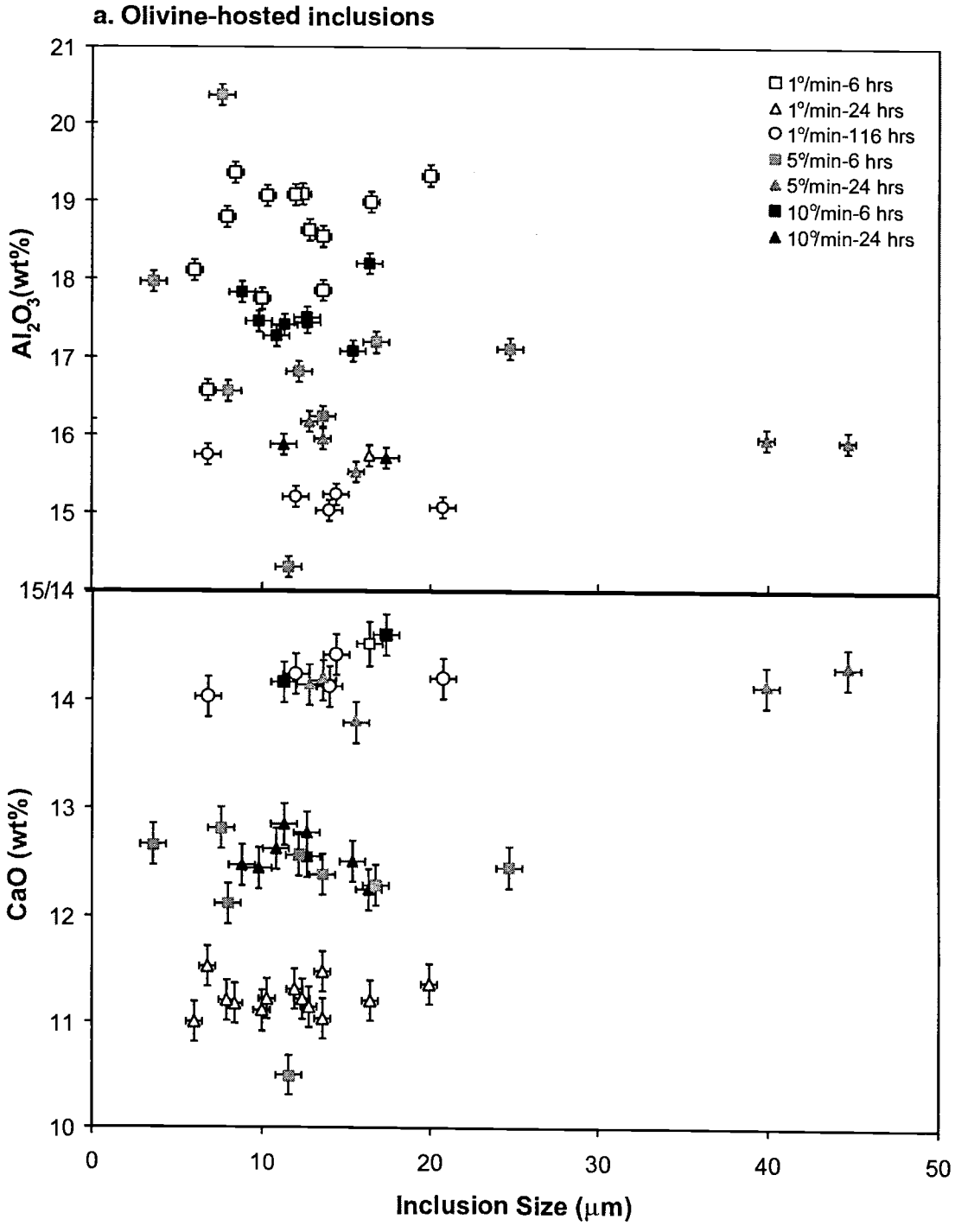

Figure 26: Inclusion size vs. representative compositions. Compositions chosen to represent cations rejected during growth that may be present in a boundary layer surrounding the crystal. CaO and Al_2O_3 are shown for olivine-hosted inclusions (a), Mg# and TiO_2 for plagioclase-hosted inclusions (b-next page). Note that there was no systematic variation with size, indicating that an entrapped boundary layer was not detected. Variation that was present may reflect melt trapped at different points in the experiment run time.

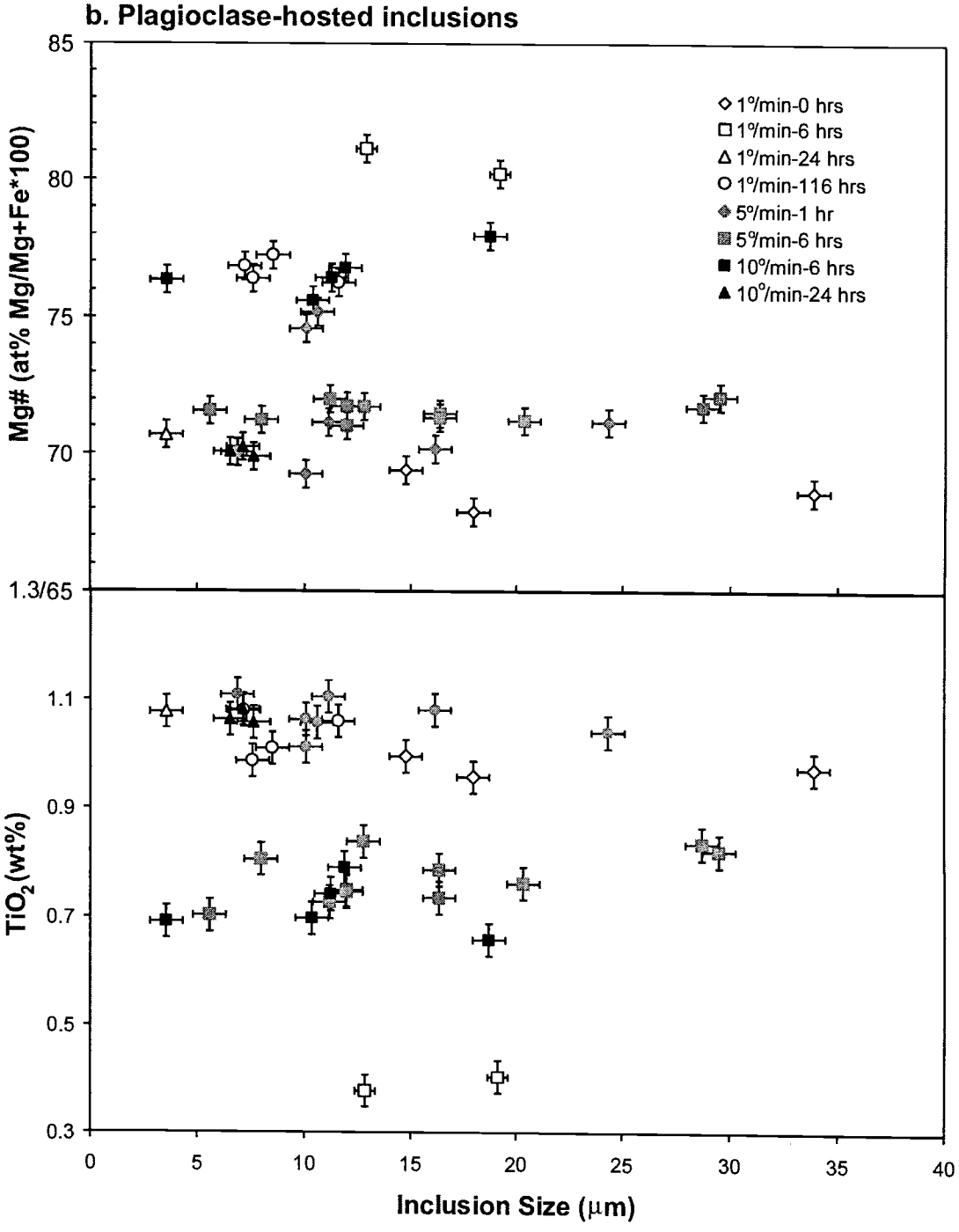
b. Plagioclase-hosted inclusions
Mg# (at% Mg/Mg+Fe*100)
85
80
75
70
1.3/65
1°/min-0 hrs
1°/min-6 hrs
1°/min-24 hrs
1°/min-116 hrs
5°/min-1 hr
5°/min-6 hrs
10°/min-6 hrs
10°/min-24 hrs
TiO2 (wt%)
1.1
0.9
0.7
0.5
0.3
0
5
10
15
20
25
30
35
40
Inclusion Size (μm)

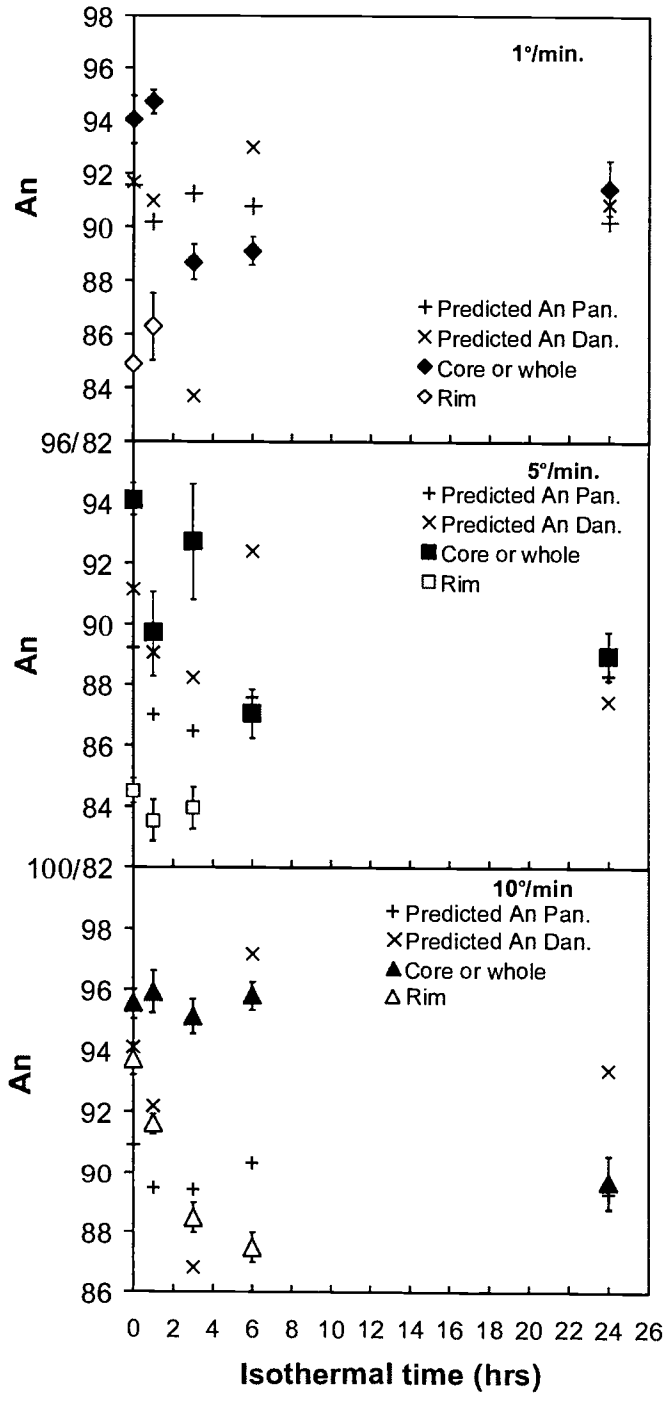

Figure 27: Calculated and observed An contents for feldspars vs. isothermal crystallization time. For unzoned feldspars, An numbers refer to averages for whole crystals. Errors are standard deviation from average. Predicted An Pan. points are expected An values calculated using Panasawatwong et al. (1995) equation 1, Predicted An Dan. are predicted An values using Danyushevsky's model in Petrolog software. Note feldspar compositions approached predicted equilibrium values with increasing isothermal time, which correlates with the change to more equilibrium, planar crystal morphologies.

Table 10: Glass and MI Compositions for ΔT=90°

Isothermal Period = 0 hrs.						
	1°/min Glass		5°/min Glass		10°/min Glass	
	Avg	2σ	Avg	2σ	Avg	2σ
SiO_2	47.99	0.56	48.85	0.45	49.35	0.34
TiO_2	0.83	0.06	0.75	0.06	0.78	0.06
Al_2O_3	17.51	0.69	18.33	0.89	18.69	0.98
FeO*	7.03	0.20	6.52	0.22	6.37	0.32
MnO	0.11	0.02	0.13	0.03	0.12	0.03
MgO	9.06	0.29	9.32	0.39	9.03	0.47
CaO	14.62	0.14	14.79	0.12	14.73	0.13
Na_2O	1.57	0.06	1.40	0.06	1.51	0.05
K_2O	0.07	0.02	0.06	0.02	0.07	0.02
P_2O_5	0.05	0.01	0.06	0.01	0.05	0.01
Cr_2O_3	0.10	0.03	0.07	0.03	0.07	0.02
ZrO_2	0.06	0.05	0.07	0.05	0.06	0.05
	99.00	n=31	100.35	n=32	100.83	n=20
	Plag MI		Plag MI		Plag MI	
	Avg	2σ	Avg	2σ	Avg	2σ
SiO_2	48.69		-		-	
TiO_2	0.95		-		-	
Al_2O_3	14.87		-		-	
FeO*	7.61		-		-	
MnO	0.12		-		-	
MgO	10.16		-		-	
CaO	14.58		-		-	
Na_2O	1.42		-		-	
K_2O	0.06		-		-	
P_2O_5	0.03		-		-	
Cr_2O_3	0.07		-		-	
ZrO_2	0.14		-		-	
	98.70	n=1		n=0		n=0

Isothermal Period = 6 hrs.						
1°/min Glass		5°/min Glass		10°/min Glass		
Avg	2σ	Avg	2σ	Avg	2σ	
55.85	0.40	53.77	0.97	50.24	0.15	
0.63	0.06	0.80	0.20	1.19	0.04	
16.14	0.22	15.72	0.37	14.32	0.11	
5.58	0.39	6.12	0.57	7.41	0.12	
0.13	0.04	0.12	0.02	0.14	0.02	
9.71	0.15	9.82	0.13	9.56	0.13	
11.27	0.23	12.12	0.32	15.24	0.13	
0.88	0.02	0.92	0.10	1.19	0.03	
0.06	0.02	0.06	0.03	0.11	0.01	
0.07	0.05	0.08	0.01	0.09	0.01	
0.06	0.03	0.06	0.02	0.07	0.05	
n/a	n/a	n/a	n/a	n/a	n/a	
100.38	n=5	99.59	n=12	99.56	n=5	
Plag MI		Plag MI		Plag MI		
Avg	2σ	Avg	2σ	Avg	2σ	
55.32	0.41	53.71	0.71	-		
0.68	0.10	0.76	0.27	-		
16.12	0.26	15.45	0.45	-		
5.56	0.51	6.21	0.54	-		
0.11	0.03	0.11	0.02	-		
9.8	0.28	10.16	1.27	-		
11.43	0.33	11.93	0.57	-		
0.83	0.03	0.88	0.09	-		
0.08	0.02	0.07	0.02	-		
0.05	0.02	0.07	0.00	-		
0.05	0.03	0.07	0.02	-		
n/a	n/a	n/a	n/a	-		
100.03	n=7	99.42	n=6		n=0	

Table 10 continued

Isothermal Period = 6 hrs.		
	1°/min Ol MI Avg	2σ
SiO_2	56.09	0.73
TiO_2	0.65	0.04
Al_2O_3	16.57	0.23
FeO*	5.64	0.54
MnO	0.12	0.03
MgO	9.81	0.21
CaO	11.6	0.13
Na_2O	0.84	0.03
K_2O	0.04	0.02
P_2O_5	0.06	0.01
Cr_2O_3	0.07	0.03
ZrO_2	0.04	0.04
	101.53	n=9

Table 11: Glass and MI Compositions for $\Delta T=70^{\circ}$

Isothermal Period = 0 hrs.

	1°/min Glass		5°/min Glass		10°/min Glass	
	Avg	2σ	Avg	2σ	Avg	2σ
SiO_2	48.82	0.35	49.35	0.42	49.22	0.33
TiO_2	0.85	0.03	0.86	0.07	0.80	0.07
Al_2O_3	18.63	0.36	18.51	1.00	18.74	1.07
FeO*	7.07	0.11	7.09	0.33	6.53	0.30
MnO	0.10	0.03	0.11	0.04	0.08	0.02
MgO	8.44	0.13	8.18	0.43	8.92	0.49
CaO	14.48	0.14	14.51	0.32	14.68	0.13
Na_2O	1.78	0.12	1.80	0.16	1.58	0.06
K_2O	0.05	0.01	0.06	0.01	0.05	0.01
P_2O_5	0.06	0.02	0.06	0.02	0.06	0.02
Cr_2O_3	0.09	0.04	0.11	0.03	0.07	0.02
ZrO_2	n/a	n/a	n/a	n/a	n/a	n/a
	100.37	n=15	100.64	n=17	100.73	n=16
	Plag MI		**Plag MI**		**Plag MI**	
	Avg	2σ	Avg	2σ	Avg	2σ
SiO_2	48.84	0.19	-		-	
TiO_2	0.98	0.02	-		-	
Al_2O_3	16.97	0.89	-		-	
FeO*	7.49	0.12	-		-	
MnO	0.15	0.02	-		-	
MgO	8.93	0.30	-		-	
CaO	14.49	0.34	-		-	
Na_2O	1.82	0.06	-		-	
K_2O	0.05	0.01	-		-	
P_2O_5	0.11	0.01	-		-	
Cr_2O_3	0.13	0.02	-		-	
ZrO_2	n/a	n/a	-		-	
	99.96	n=3		n=0		n=0

Isothermal Period = 1 hr.

1°/min Glass		5°/min Glass		10°/min Glass	
Avg	2σ	Avg	2σ	Avg	2σ
49.51	0.19	50.61	0.29	50.11	0.55
0.94	0.02	1.06	0.03	0.89	0.07
16.7	0.09	16.54	0.11	17.99	1.05
7.54	0.19	6.56	0.63	6.75	0.30
0.1	0.24	0.14	0.03	0.08	0.02
9.93	0.16	9.82	0.19	8.88	0.48
14.77	0.16	14.68	0.29	13.80	0.13
1.41	0.04	1.52	0.06	1.60	0.05
0.06	0.01	0.06	0.01	0.06	0.01
0.08	0.02	0.09	0.02	0.05	0.03
0.1	0.03	0.12	0.02	0.05	0.02
n/a	n/a	0.07	0.04	n/a	n/a
101.14	n=10	101.27	n=16	100.26	n=10
Plag MI		**Plag MI**		**Plag MI**	
Avg	2σ	Avg	2σ	Avg	2σ
-		50.51	0.52	-	
-		1.07	0.04	-	
-		16.36	0.50	-	
-		6.91	0.62	-	
-		0.13	0.03	-	
-		9.79	0.28	-	
-		14.39	0.34	-	
-		1.51	0.05	-	
-		0.07	0.01	-	
-		0.10	0.03	-	
-		0.13	0.02	-	
-		0.11	0.05	-	
	n=0	101.08	n=7		n=0

Table 11 continued

Isothermal Period = 3 hrs.						
	1°/min Glass		5°/min Glass		10°/min Glass	
	Avg	2σ	Avg	2σ	Avg	2σ
SiO_2	50.04	0.23	50.49	0.33	49.88	0.34
TiO_2	1.00	0.04	1.00	0.04	0.95	0.02
Al_2O_3	16.39	0.47	16.61	0.09	16.64	0.13
FeO*	7.65	0.20	6.93	0.17	7.37	0.13
MnO	0.13	0.03	0.14	0.02	0.12	0.03
MgO	8.95	0.20	9.70	0.07	10.26	0.13
CaO	13.12	0.26	14.12	0.28	13.99	0.27
Na_2O	1.98	0.06	1.61	0.03	1.72	0.04
K_2O	0.12	0.01	0.08	0.00	0.05	0.01
P_2O_5	0.09	0.03	0.10	0.02	0.06	0.02
Cr_2O_3	0.09	0.04	0.12	0.01	0.07	0.03
ZrO_2	0.03	0.03	0.06	0.03	0.14	0.04
	99.59		100.96	n=9	101.25	
	Plag MI		**Plag MI**		**Plag MI**	
	Avg	**2σ**	**Avg**	**2σ**	**Avg**	**2σ**
SiO_2	-		50.69	0.33	-	
TiO_2	-		1.02	0.04	-	
Al_2O_3	-		16.63	0.77	-	
FeO*	-		6.89	0.13	-	
MnO	-		0.15	0.03	-	
MgO	-		9.67	0.49	-	
CaO	-		14.41	0.31	-	
Na_2O	-		1.59	0.02	-	
K_2O	-		0.08	0.01	-	
P_2O_5	-		0.11	0.03	-	
Cr_2O_3	-		0.10	0.02	-	
ZrO_2	-		0.07	0.03	-	
		n=0	101.41	n=9		n=0

Isothermal Period = 6 hrs.						
	1°/min Glass		5°/min Glass		10°/min Glass	
	Avg	2σ	Avg	2σ	Avg	2σ
SiO_2	53.49	0.48	51.73	0.53	50.63	0.54
TiO_2	0.39	0.02	0.78	0.03	0.68	0.05
Al_2O_3	18.91	0.23	17.05	0.20	17.61	1.12
FeO*	5.07	0.13	7.27	0.14	5.99	0.37
MnO	0.12	0.02	0.13	0.03	0.11	0.04
MgO	11.51	0.30	10.2	0.08	10.87	0.80
CaO	11.21	0.09	12.52	0.07	12.59	0.42
Na_2O	0.91	0.05	1.37	0.06	1.15	0.06
K_2O	0.04	0.01	0.08	0.01	0.06	0.01
P_2O_5	0.04	0.02	0.07	0.02	0.08	0.03
Cr_2O_3	0.06	0.03	0.09	0.03	0.07	0.03
ZrO_2	0.03	0.02	0.03	0.03	n/a	n/a
	101.78	n=12	101.32	n=9	99.84	n=29
	Plag MI		**Plag MI**		**Plag MI**	
	Avg	**2σ**	**Avg**	**2σ**	**Avg**	**2σ**
SiO_2	54.92	1.17	51.73	0.29	51.01	0.53
TiO_2	0.39	0.02	0.77	0.05	0.72	0.05
Al_2O_3	17.98	0.47	17.01	0.55	17.36	0.79
FeO*	4.79	0.36	7.20	0.20	5.95	0.18
MnO	0.09	0.01	0.13	0.02	0.12	0.05
MgO	11.18	0.39	10.16	0.21	10.96	0.72
CaO	11.06	0.17	12.7	0.23	12.88	0.26
Na_2O	0.94	0.06	1.35	0.04	1.12	0.08
K_2O	0.04	0.01	0.08	0.01	0.05	0.01
P_2O_5	0.02	0.00	0.05	0.08	0.08	0.01
Cr_2O_3	0.06	0.00	0.08	0.02	0.06	0.02
ZrO_2	0.06	0.04	0.04	0.02	n/a	n/a
	101.53	n=2	101.3	n=11	100.31	n=5

Table 11 continued

Isothermal Period =24 hrs.						
	1°/min Glass		5°/min Glass		10°/min Glass	
	Avg	2σ	Avg	2σ	Avg	2σ
Si	49.15	0.51	50.35	0.27	49.19	0.16
Ti	0.95	0.34	1.05	0.03	1.09	0.02
Al	17.62	0.49	15.96	0.12	15.55	0.09
Fe	6.52	1.97	6.01	0.23	7.75	0.10
Mn	0.12	0.06	0.15	0.02	0.13	0.03
Mg	9.83	0.57	10.53	0.07	10.24	0.04
Ca	14.83	0.82	14.22	0.15	14.56	0.13
Na	0.89	0.08	1.53	0.04	1.06	0.03
K	0.05	0.02	0.10	0.01	0.07	0.00
P	0.09	0.05	0.08	0.02	0.10	0.03
Cr	0.06	0.04	0.07	0.03	0.1	0.02
Zr	0.05	0.06	0.05	0.04	0.09	0.03
	100.16	n=5	100.1	n=8	99.93	n=8
	Plag MI		Plag MI		Plag MI	
	Avg	2σ	Avg	2σ	Avg	2σ
Si	49.02		-		49.32	0.25
Ti	1.08		-		1.07	0.01
Al	16.13		-		15.76	0.42
Fe	7.53		-		7.72	0.12
Mn	0.12		-		0.16	0.04
Mg	10.18		-		10.15	0.19
Ca	14.71		-		14.52	0.21
Na	0.85		-		1.06	0.01
K	0.06		-		0.08	0.00
P	0.02		-		0.11	0.01
Cr	0.03		-		0.09	0.00
Zr	0.00		-		0.07	0.04
	99.73	n=1		n=0	100.11	n=3

Isothermal Period =116 hrs.		
	1°/min Glass	
	Avg	2σ
Si	51.41	0.21
Ti	1.08	0.03
Al	15.13	0.07
Fe	5.73	0.13
Mn	0.14	0.04
Mg	10.48	0.06
Ca	14.31	0.11
Na	0.88	0.03
K	0.10	0.01
P	0.06	0.03
Cr	0.08	0.03
Zr	0.07	0.04
	99.47	n=8
	Plag MI	
	Avg	2σ
Si	50.87	0.89
Ti	1.03	0.06
Al	16.56	0.93
Fe	5.73	0.21
Mn	0.14	0.01
Mg	9.89	0.44
Ca	14.31	0.20
Na	0.92	0.02
K	0.10	0.01
P	0.11	0.04
Cr	0.09	0.00
Zr	0.07	0.06
	99.82	n=2

Table 11 continued

Isothermal Period =116 hrs.		
	1°/min Ol MI	
	Avg	2σ
SiO_2	50.61	0.80
TiO_2	1.09	0.02
Al_2O_3	15.25	0.29
FeO*	5.98	0.27
MnO	0.15	0.02
MgO	10.74	0.38
CaO	14.2	0.15
Na_2O	0.96	0.18
K_2O	0.10	0.01
P_2O_5	0.11	0.03
Cr_2O_3	0.09	0.02
ZrO_2	0.10	0.05
	99.38 n=5	

Table 11 continued

Isothermal Period = 6 hrs.						
	1°/min Ol MI		5°/min Ol MI		10°/min Ol MI	
	Avg	2σ	Avg	2σ	Avg	2σ
SiO_2	54.23	0.81	50.48	1.19	50.96	0.54
TiO_2	0.38	0.05	0.70	0.09	0.71	0.04
Al_2O_3	18.26	0.97	17.07	1.71	17.53	0.35
FeO*	4.80	0.28	6.89	0.57	5.84	0.14
MnO	0.09	0.02	0.14	0.04	0.12	0.03
MgO	11.95	1.97	10.31	2.40	10.57	0.50
CaO	11.01	0.52	12.22	0.73	12.56	0.19
Na_2O	0.95	0.06	1.35	0.08	1.23	0.04
K_2O	0.03	0.01	0.08	0.02	0.07	0.01
P_2O_5	0.04	0.02	0.08	0.03	0.08	0.05
Cr_2O_3	0.10	0.03	0.08	0.03	0.07	0.03
ZrO_2	0.02	0.03	0.04	0.02	n/a	n/a
	101.86 n=16		99.44 n=8		1.45 n=8	

Isothermal Period =24 hrs.					
1°/min Ol MI		5°/min Ol MI		10°/min Ol MI	
Avg	2σ	Avg	2σ	Avg	2σ
48.73		50.39	0.87	49.47	0.68
0.97		1.06	0.05	1.09	0.01
15.73		15.90	0.24	15.79	0.12
8.21		5.81	0.38	7.21	0.80
0.17		0.16	0.02	0.1	0.00
10.79		10.60	0.17	10.03	0.01
14.52		14.10	0.19	14.38	0.31
0.88		1.54	0.07	1.17	0.09
0.02		0.10	0.02	0.07	0.00
0.10		0.09	0.03	0.12	0.01
0.09		0.09	0.03	0.08	0.03
0.07		0.06	0.02	0.03	0.05
	n=1	99.9 n=5		99.54 n=2	

Table 12: Mineral Compositions

ΔT	Cooling rate	Isothermal time	Predicted An[a]	Predicted An[b]	Plag core An*	Plag rim An	Olivine Fo
90°	1	0	86.36	89.05	97.11	83.72	-
90°	1	6	83.06	92.01	88.28		91.35
90°	5	0	88.13	89.55	97.02	86.41	-
90°	5	6	83.47	87.88	85.95		-
90°	10	0	87.83	98.25	96.68		-
90°	10	6	82.72	87.95	87.82		89.10
70°	1	0	91.56	91.68	94.04	84.89	-
70°	1	1	90.17	90.97	94.72	86.29	-
70°	1	3	91.26	83.69	88.67		-
70°	1	6	92.77	93.00	89.08		93.76
70°	1	24	90.21	90.87	91.46		89.64
70°	1	116	89.06	90.24	88.84		91.77
70°	5	0	89.22	91.14	94.10	84.50	-
70°	5	1	86.99	89.05	89.72	83.51	-
70°	5	3	86.46	88.22	92.72	83.95	-
70°	5	6	87.57	92.40	87.04		91.33
70°	5	24	88.31	87.46	88.97		91.62
70°	10	0	90.92	94.09	95.55	93.70	-
70°	10	1	89.45	92.18	95.91	91.62	-
70°	10	3	86.16	86.81	95.11	88.47	94.20
70°	10	6	90.33	97.16	95.82	87.49	92.47
70°	10	24	89.29	93.37	89.68		89.61

Values are averages

*when no rim values are listed, no zoning was present and core values refer to averages for whole crystals

a Expected An values calculated with equation 1 of Panjasawatwong et al., (1995)

b Expected An values calculated with Danyushevsky routine in PETROLOG

DISCUSSION

Inclusion formation mechanisms

The results demonstrate that primary inclusions in high-An feldspar and high-Fo olivine can result from changes in crystal morphology due to changes in growth mechanism in a process similar to that proposed by Roedder (1984). During the cooling and the initial isothermal periods, feldspars growth rates were several orders of magnitude greater than the estimated ability of diffusion to remove rejected cations or supply those needed for growth. For example, plagioclase grew immediately after cooling 1°/min. at a rate of 1.16×10^{-2} μm/s, while diffusion could only supply Ca at ~1.5×10^{-3} μm/s and remove Fe^{2+} at ~9.5×10^{-7} μm/s (based on diffusion coefficients in Freer, 1981; Cooper et al., 1996). Crystal growth (needed remove latent heat of crystallization during undercooling) could only occur on protuberances through the boundary layer,

resulting in swallow-tail and skeletal morphologies with elongate projections. As growth rate decreased with isothermal time and diffusion became more efficient at removing and supplying cations, the growth mechanisms became surface-nucleation controlled. This change initially resulted in hoppers formed by stepwise growth. As the growth rate continued to decrease with lengthening isothermal time, more planar crystal faces formed and tabular and equant morphologies were produced. Embayments in crystals that grew during undercooling were covered with overgrowth and melt was trapped within the growing crystal.

The results may also provide a potential explanation for the bands of melt inclusions that are commonly observed in plagioclase. During experiments with longer than 3 hours isothermal time, crystals of both olivine and plagioclase nucleated along the capsule rims. The plagioclase in these overgrowths grew in a stepwise fashion to produce hopper textures and these hoppers formed zones of inclusions parallel to the rim (Figure 20a). These zones in the capsule overgrowth may be similar to the bands of inclusions observed in natural anorthite phenocrysts, and we propose that in the case of the natural phenocrysts, the bands of inclusions may be created by the formation of hopper crystals attached to a pre-existing host feldspar. Bands of inclusions formed in such a way would record the melt composition after the phenocryst had been undercooled, and not the composition and condition under which the phenocryst's core nucleated.

The question arises whether or not the cells, or inclusions, we observed were truly enclosed on all sides. It was not possible to answer this with certainty using two-dimensional imaging techniques, but several observations led us to conclude that most inclusions we observed were likely enclosed. First, it was noted that when hollow core skeletal crystals were visible oriented both along and across their long axes in a single experiment, in both cases the core was enclosed on all sides. The same was observed with inclusions in plagioclase and olivine that were sectioned both along and across the long axis. Secondly, we limited the inclusions we examined to those with a more rounded appearance. Larger, more angular cells were considered to be possible open embayments and not true inclusions. Third, the average compositions of the inclusions were near-identical to the host glass, except for those formed during cooling. This is to be expected if the inclusions formed during cooling trapped liquid that was different from

the composition at run temperature. In addition, although average compositions for inclusions formed during longer isothermal periods were similar to the host glass for each particular experiment, minor variability was present. This diversity may have resulted from entrapment of melt at an earlier stage in the experiment (Figure 26), as described in detail in the results. Such compositional differences between inclusions and inclusions and host glass, although small, would not be observed if the cells were open embayments.

Our results suggest that most inclusions formed with cooling followed by a short (6 hours) isothermal period (Table 9). In the case of both minerals, the favored early texture had large numbers of embayments and re-entrants that could later become inclusions (Table 8). Significantly, few inclusions formed during cooling and isothermal times of less than 6 hours following all cooling rates. For our experiments, we suggest that 5°/min cooling resulted in more inclusions because with this cooling rate in our system, well-developed hopper textures were favored in both the feldspars in the liquid and within the capsule rim overgrowth.

The observation that cooling rate affected olivine morphology and inclusion frequency (the greatest frequency of olivine-hosted inclusions followed 10°/min. cooling) appears counterintuitive, since olivine did not crystallize until after 6 hours isothermal time, and olivine morphology would be not be expected to be influenced by cooling rate. However, Hort and Spohn (1991) have demonstrated that in small systems, thermal feedback from crystallization has the effect of extending small amounts of undercooling further into the cooling period. Plagioclase was crystallizing during the cooling periods and isothermal periods< 6 hours, with the nucleation rate at the beginning of the isothermal period dependent on the cooling rate (Table 9, Figure 21). As a result, the nucleation rate of plagioclase would controlled any thermal feedback, and thus the cooling rate could still influence the olivine morphologies that developed even after an isothermal interval.

Over longer isothermal times, the inclusion frequency could also be affected by Ostwald ripening in the system, an increase in grain size by dissolution of smaller crystals and a decrease in the number of crystals in a system at chemical equilibrium. This process (Joesten, 1991, Park and Hanson, 1999; Baldan, 2002) results in smaller crystals with greater specific surface free energy dissolving and larger crystals increasing

in size, which then must be fewer in number due to mass balance constraints (Erbel, et al., 1998; Snyder, et al., 1999; Baldan, 2002). Ostwald ripening has long been recognized as a process that controls coarsening of a phase scattered in a homogeneous matrix of another phase in both natural and synthetic materials (Joesten, 1991; Baldan, 2002), and substantial coarsening of fosterite in haplobasaltic melts (SiO_2-Al_2O_3-CaO-MgO) has been attributed to Ostwald ripening (Park and Hanson, 1999). In our experiments, the system approached chemical equilibrium as the isothermal time progressed. Although the number of crystals we observed did not follow any noticeable systematic variation with isothermal time, we did note some increase in grain size with run time, and very large olivine and plagioclase were observed in the 24 hour experiments and the116 hour experiment following 1°/min cooling. A complicating factor is the possibility that any temperature gradients, even small ones, in our system could cause additional mass transport that would obscure Ostwald ripening effects (Snyder, et al., 1999). Nevertheless, it must be considered that the Ostwald ripening process could have an influence on inclusion frequency in natural systems, and the longer a melt with phenocrysts remains at chemical equilibrium, the more likely coarsening and attendant decrease in the number of inclusions will take place. The possibility that Ostwald ripening could occur in crystallizing basaltic systems would have significant implications for olivine-hosted inclusions. Gaetani and Watson (2000, 2002) demonstrated that olivine-hosted inclusions might behave as open systems for major elements due to diffusive re-equilibration through the crystal lattice. If coarsening due to Ostwald ripening were to take place, then the radii of smaller host crystals would decrease and that of larger crystals would increase over time. Because diffusive re-equilibration is controlled in part by the relative radii of inclusion and host crystal (Qin et al, 1992), the rate of inclusion modification then would not be constant in a system at chemical equilibrium, but instead would increase or decrease depending on whether the host crystal was dissolving and shrinking or growing larger.

Compositional Effects

Nearly all experimentally produced inclusions in olivine and plagioclase in a given experiment- had average compositions near-identical to the surrounding glass. The experiments with inclusions formed only during cooling were exceptions, and these were

not likely to be in equilibrium with the host glass at the quench time (Table 10 and 11, Figures 23-25). The lack of a systematic variation in composition with melt inclusion size (Figure 26) indicates that a boundary layer or diffusive profile was not entrapped during the formation of the melt inclusions in the experiments. The isothermal run times required for the formation of the majority of inclusions were long enough to limit the trapping of a boundary layer. However, the diffusion coefficients in basalt for cations such as Ca, Na, Mg, and Fe^{2+} (Donaldson, 1975; Freer, 1981; Cooper et al., 1996) constrained cation transport in basalt liquid due to diffusion to 10^{-3}-10^{-7} μm/s at our run temperatures, slower than our estimated growth rates. In our small system with rapid cooling, it is possible that advective transport of cations aided in the dissipation of any boundary layer before the inclusions were sealed. Although growth in natural systems that produces incomplete morphologies with embayments and re-entrants would to also be more rapid than diffusion in the liquid, it is not during the development of the incomplete morphologies that inclusions are necessarily formed. Rather we suggest it is during the return to slower equilibrium growth that that the embayments are sealed off and the majority of inclusions formed. During this period of slower growth diffusion then would be able to dissipate a strong boundary layer, as planar growth occurs when the diffusion/growth rate ≈ 1 (Lofgren, 1974).

In none of the experiments did we observe the formation of low-Ti inclusions in either olivine or plagioclase-hosted inclusions, suggesting that low-Ti inclusions found in natural MORB melt inclusions are not a product of the entrapment process. For all inclusions and host glass, there is none of the K_2O diversity observed in natural melt inclusions, and K_2O contents are identical to the starting glass (Table 10 and 11).

Host glass compositions change with increasing isothermal time, yet the average compositions of the melt inclusions remain within 2σ and analytical error to the host glass. This seemingly presents a paradox, since we observed that in the case of experiments with 5°/min. cooling, the majority of inclusions formed between three and six hours isothermal time and one would expect to observe that inclusion compositions would remain similar to the 6-hour compositions in the 24 hour experiment. One likely explanation is that the EMP data were biased towards the last-formed inclusions, which would have similar compositions to the host glass at the time of quenching. The melt

inclusion size distribution plots indicate that the size of the inclusions decreased with lengthening isothermal time (Figure 22) and the largest and most easily analyzed inclusions were likely those that formed closest to quench time. Also, our melt inclusion data sets for some experiments are small and may have missed the entire range of compositions. Figure 26 shows that while the mean compositions of melt inclusions from an experiment were similar to host glass, there was some variability. Since this variability was not related to inclusion size, it is not considered a boundary effect. It is likely then that this diversity reflected melt trapped at earlier stages in the experiment when the liquid had a different composition. Longer period experiments with trace element doped starting materials that produced more run products (and thus more inclusions and data points) could test these results.

Implications for natural inclusions

We suggest that primary inclusions could form in a natural system that operates along time-temperature profiles similar to those of our experiments, although not at the rates and times we used. Such circumstances could occur in nature when a crystal bearing magma ascends through a dike into cooler crust and undergoes a moderate amount of cooling. This then is followed by a short stagnation period before eruption. Under these conditions, cooling would take place much more rapidly than in the traditional magma body concept, e.g. ~0.1°/h in a dike compared to ~0.1°/yr in a magma chamber (Cooper et al., 2001). Although these cooling rates are slower than those used in our experiments, they do not preclude the development of the textures we observed, as skeletal and hopper crystals are observed in many dikes and sills (e.g. Ikeda, 1977, Philpotts, 1994, Hibbard, 1995, Cashman, 1993). Crystals may grow rapidly at rates of 10^{-6} cm/s or 10^{-2} μm/s (Ikeda, 1977; Cashman, 1993), comparable to growth rates in our experiments, with hopper/skeletal morphologies near the edge of a conduit. These crystals could later ascend into a larger upper magma body where growth rates would be several orders of magnitude slower (10^{-9} to 10^{-11} cm/s or 10^{-5} to 10^{-8} μm/s - Mangan, 1990; Cashman, 1993) and smooth, planar overgrowth would take place. In several igneous settings, this change from rapid crystal growth with incomplete textures to slower crystal growth with smooth, planar surfaces and the consequent entrapment of melt might occur. For mid-ocean spreading centers it has been suggested that melt in the crust rises through a series

of conduits (Sinton & Detrick, 1992; Kelemen et al., 1995) and collects in melt lenses (Kelemen et al., 1995; Garrido et al, 2001). In addition, crystals growing near the periphery of these bodies may cool much faster than in the center due to heat transport away from the sides of the melt lens by hydrothermal circulation (Phipps Morgan and Chen, 1993; Cherkaoui et al, 2003). Movement of the crystals to the center of the body would slow growth rate and result in the required change in morphology and entrapment of melt. For arc settings, models have been proposed in which melt propagates through fractures in the lithosphere and accumulates in the crust prior to eruption (Stern, 2002 and references therein).

If entrapment does not lead to the diversity we observe in inclusions from natural phenocrysts, then such diversity indicates other processes at work. Instead, the host liquid composition may change over time with increasing crystallization and different periods of growth entrap different liquids or that more complex inclusion formation processes, including reaction and diffusion are involved. In the case of sequentially entrapped evolving liquids, inclusions should exhibit a spatial relationship between the location in the host and their composition. In the cases of reaction and diffusion processes, inclusion compositional diversity should be more randomly distributed through the host crystal and there should be textural evidence (patchy zonation, sieve and fritted textures) for these processes. This reinforces the need for careful preliminary petrographic examination of the phenocrysts in a sample that will be separated for melt inclusion analysis. A combination of melt inclusion and CSD data could constrain the age of inclusions, and whether they formed before or after a change in crystallization conditions (Marsh, 1988; Roggensack, 2001).

CONCLUSIONS

The results of our experiments show that melt inclusions in high-An plagioclase and high-Fo olivine in low pressure, anhydrous mafic melts can arise from changes in growth mechanisms and crystal morphology due to undercooling and subsequent isothermal crystallization. Hopper and skeletal crystals occur when a combination of undercooling and cooling promotes growth controlled by dissipation of heat and impurities during undercooling. For our system, cooling rates of 5°/min. for plagioclase and 10°/min. for olivine were the most favorable for the formation of hopper crystals. A subsequent

period of isothermal crystallization will result in a change in the rate-limiting step in crystal from heat/impurity dissipation-controlled growth to surface nucleation and diffusion-controlled growth. The result of this change in dominant growth mechanism is planar overgrowth on the hopper and skeletal crystals and the entrapment of melt. Since this is the dominant inclusion formation mechanism, most of the experimentally produced inclusions form during isothermal crystallization following cooling.

The experiments with 6-hour and greater isothermal periods exhibited the highest frequencies of inclusions, and these times appear sufficiently long to preclude trapping a boundary layer or diffusive profile. For this reason, all experimentally produced inclusions in olivine and plagioclase have compositions identical to the surrounding glass, except in the case of the few inclusions formed during cooling. With a long isothermal period (116 hours), the frequency of inclusions decreased (Table 2) and the size of crystals increased. This may indicate that coarsening processes, such as Ostwald ripening occur during longer isothermal periods and such processes may reduce the number of inclusions over time. The implication of this is that longer crystal residence times could potentially eliminate most inclusions and thus MI compositions would record only short periods in a magma's evolution. Circumstances in nature similar to our experimental conditions may occur when a partial melt rises through a conduit into cooler crust and stagnates at low pressure (<10 kb) prior to eruption and quenching.

While our suggested mechanism may be valid for primary inclusions, it does not remove secondary inclusion formation and diffusional processes from consideration when dealing with natural samples. It is important to note that negative crystal shape alone (i.e. re-entrants and cellular texture) is not proof of primary origin (Roedder, 1984). This reinforces the need for careful preliminary petrographic examination of phases that will be separated for melt inclusion analyses.

THE ORIGINS OF PRIMITIVE LAVAS IN THE MARIANA ARC: EVIDENCE FROM OLIVINE-HOSTED MELT INCLUSIONS

Edward J. Kohut
Adam J.R. Kent
Robert J. Stern
Roger L. Nielsen
Sherman H. Bloomer
Matthew Leybourne

This ms submitted to the Journal of Petrology

ABSTRACT

Samples of very primitive (Mg# ~ 76) lavas have obtained from a small parasitic cone situated on the Mariana arc magmatic front, NW of Rota. These lavas can be classified by mineralogy as picrite and ankaramite and erupted 2.49±0.18 Ma. and 1.73±0.06 Ma. respectively. Whole rock compositions are 14.8-15.4 wt% MgO, 0.47-0.48 wt% TiO_2, and ~2% total alkalis. Isotopically the samples are similar to typical Mariana arc lavas ($^{87}Sr/^{86}Sr$ ~ 0.7033, εNd ~ +6.5). Phenocryst compositions are similar for both lavas: olivine phenocrysts are $Fo_{87.2-92.0}$ with 0.09-0.26 wt% NiO, CPX have compositions of $Wo_{41.4-47.9}$, $En_{43.8-51.7}$ and $Fs_{2.7-9.1}$, and chromites have Cr#s (Cr/Cr+Al) of 0.95-0.74 and Mg#s ($Mg/Mg+Fe^{2+}$) of 0.29-0.47.

The major and trace element compositions of melt inclusions (MI) within Fo_{89-92} olivine in the picrite represent samples of primitive mantle melts with Mg#s up to 81. The MI have up to 25% MgO and, 0.23-0.8% TiO_2, 43.2-51.0% SiO_2, and 1.66-3.43% total alkalis. Normalized trace-element concentrations have a typical subduction pattern, but are more depleted than most island arc tholeiites. Chlorine contents are typically ~100 ppm, and H_2O contents of 0.16-0.64 wt% in inclusions analyzed by FTIR indicate much of the melt was water-poor. A small number of MI have higher LILE, U, Na and Cl and we suggest these are samples of metasomatised mantle melt. Elevated levels of Th/Yb in most MI may indicate the mixing of sediment melt. High MgO (>18 wt%), depleted MI may represent samples of anhydrous decompression melt. Covariation of Nb and Yb suggest ~6 to 25% melting for the high LILE melt, and up to 60% melting of a depleted (2%<) mantle source for the high MgO melt. Estimated magmatic temperatures ranged from 1200-1500°C.

We propose that the genesis of the arc picrite can best be explained by a model in which an initial melt of metasomatized mantle rose vertically in a diapir and induced decompression melting as it ascended. The secondary decompression melt buffered high MgO contents while diluting the subduction signal and volatiles. Stagnation of the diapir at the base of the lithosphere with crystal accumulation was followed by eruption of crystal rich melt with little modification in the upper mantle and crust.

INTRODUCTION

Background

Investigation into the origins of magmas in subduction zones continues to be one of the most important areas of study in igneous petrology (Myers and Johnston, 1996; Lee and Stern, 1998; Hirschmann et al., 2000). Any understanding of the nature of subduction zone magmatism requires knowledge of the composition of the unmodified partial melt from the source region, which is commonly accepted to be peridotite in the mantle wedge. Primary magmas from this region would be expected to have compositions consistent with equilibrium melting of mantle peridotite and thus be magnesian with FeO/MgO<1. The chemistry of these melts can provide, through geothermometry, geobarometry and experimental reproduction, constraints on the compositional and thermal structure of sub-arc mantle (Myers and Johnston, 1996; Hirschman, 2000; Falloon et al, 2001). Presumably, primary magma compositions could be determined by examining samples of primitive lavas (MgO>8 wt% and Mg#s >70) that have suffered little modification between initial melting and eruption. Although arc lavas that record equilibrium with the mantle are exceedingly rare (Lee and Stern, 1998; Hirschmann et al., 2000), there are a few notable exceptions (e.g., Tonga-Hawkins et al., 2003; New Georgia, Solomons- Scuth et al. 2003; Monzier et al., 1997; Ramsay et al., 1984; Aoba,Vanuatu-Eggins, 1993; Epi, Vanuatu-Della-Pasqua and Varne, 1997; Okmok, western Aleutians-Nye and Reid, 1986). The crucial data on subduction zone magma-genesis that may be obtained from such high-MgO lavas coupled with their relative scarcity, provides compelling reasons for a detailed examination of any newly discovered example.

In this study, we present analyses of primitive picrite and ankaramite sampled from a previously unknown submarine volcano along the Mariana arc magmatic front. In contrast to most earlier studies of primitive arc lavas (an exception is Della-Pasqua and Varne, 1997), we also provide data from melt included in Fo_{88-92} phenocrysts in the picrite. These inclusions were particularly scarce in the less abundant olivine in the ankarmite and consequently we limit our discussion of that lava to bulk compositions. We chose to examine melt inclusions as a means to directly sample mantle melts and circumvent the shallow level modification that affects most basaltic lavas (e.g. Bacon et

al, 1992; Sobolev, 1996; Saal et al., 1998; Nielsen et al., 1995; Sisson and Bronto, 1998; Sour-Page et al., 1999; Gaetani and Watson, 2002; Kent and Elliot, 2002). Although presumably this method would be unnecessary for very primitive arc lavas (Mg#s>70), even these appear to have been modified between partial melting and eruption. To begin with, many high-MgO arc lavas are picrites and ankaramites with evidence for crystal accumulation which must be considered when interpreting the bulk compositions. Furthermore, inverse experiments using high-MgO lavas with low phenocryst contents (e.g., Tatsumi, 1982; Tatsumi et al., 1983, 1994; Gust and Perfit, 1987; Bartels et al., 1991; Draper and Johnston, 1992) produced results that did not agree with existing thermal models (e.g., Tatsumi, 1982; Tatsumi et al., 1983, 1994; Gust and Perfit, 1987; Bartels et al., 1991; Draper and Johnston, 1992). Although the experimentally produced liquids were in equilibrium with mantle mineral assemblages, temperatures were ~1290-1360°C at significantly lower pressures (9-17 kbar) than predicted by the models of subduction zone geotherms (Furukawa, 1993; Myers and Johnston, 1996; Peacock and Wang, 1999; Davies and Stevenson, 2001). Instead, it has been concluded that these conditions likely reflect those in a partially molten peridotitic diapir at its last low pressure point of equilibration with the mantle (Johnston and Draper, 1992; Tatsumi and Eggins, 1995; Stern 2000). In addition to providing a method of addressing this problem, melt inclusion compositions can also provide data regarding the amount of water in the parental melt, as well as the addition of any slab derived components.

Geological Setting

The Marianas subduction zone is the southern portion of an extended tripartite system that together with the Izu and Bonin subduction zones are collectively referred to as the Izu-Bonin-Mariana (IBM) system (Stern et al., 2003). This system extends over 2800 km from near Tokyo to south of Guam. The Marianas arc itself is subdivided into the Central Island Province (CIP), the Southern Seamount Province (SSP) and a number of seamount cross-chains that extend from the magmatic front towards an actively spreading back-arc, the Marianas Trough (Bloomer et al, 1989; Stern et al, 2003). Because the IBM system is an intra-oceanic convergent margin, which eliminates contamination by continental crust and continent derived sediment input that obscure the mantle signal (Dixon and Stern, 1983; Stern and Bibee, 1984; Bloomer and Hawkins,

1987; Bloomer et al., 1989), it is one of the focus areas of the NSF-MARGINS initiative (Hirschmann et al., 2000).

The lavas which are the focus of this paper were sampled from an arc-front seamount that we have named Chaife, from the god of the forge in Chamorro mythology. The Chaife seamount is a parasitic cone on the north flank of a larger volcanic edifice at the Mariana arc magmatic front northwest of Rota (Figure 28). Lavas were sampled by chain-bag dredge (D14) from R/V Melville during Leg 7 of the Cook Expedition, spring 2001 (Bloomer and Stern, 2001). Dredge depths for D14 were 1860-2188 meters. Dredges of the parent volcano (D11 and D13-Figure 28) recovered only thick Mn crust, indicating that it has been inactive longer than Chaife. There is a line of cross-arc volcanoes extending westward from the Chaife seamount approximately along 14° 35' N. Another line of seamounts begins at the magmatic front ~ 7 km. north of Chaife and extends to the SW, where it intersects the west-trending chain (inset-Figure 28). Many of the seamounts closest to the arc are also heavily Mn-encrusted. The existence of these chains indicates that magmatism in this portion of the Mariana subduction zone was not confined to the arc and back-arc spreading center. We have yet to determine a structural or tectonic control for the distribution of these volcanoes.

ANALYTICAL METHODS

Whole Rock Composition

Whole rock samples were prepared and analyzed at the University of Texas at Dallas. Samples (200 mg) were weighed into teflon beakers and digested using a four-acid cocktail under open beaker conditions. Dissolution utilized HF, $HClO_4$, HCl and HNO_3 acids, with the final solution at 250x dilution in ~10% HNO_3 (by volume). The final solution was diluted a further 10x prior to analysis, in 4% HNO_3. In a typical batch of 25 samples, 5-6 samples represent certified reference materials (CRM's), 1-2 procedural blanks and the remainder are sample unknowns. CRM's used include BIR-1 (Icelandic basalt), W-2 (diabase), BHVO-2 (Hawaiian basalt), BCR-2 (Columbia River basalt), AGV-2 (andesite), RGM-1 Glass Mountain rhyolite), GSP-2 (Silver Plume granodiorite), and G-2 (granite). Acids are distilled in-house or Baseline grade from Seastar Chemicals. All dilutions were prepared using 18.2 MΩ distilled water from a

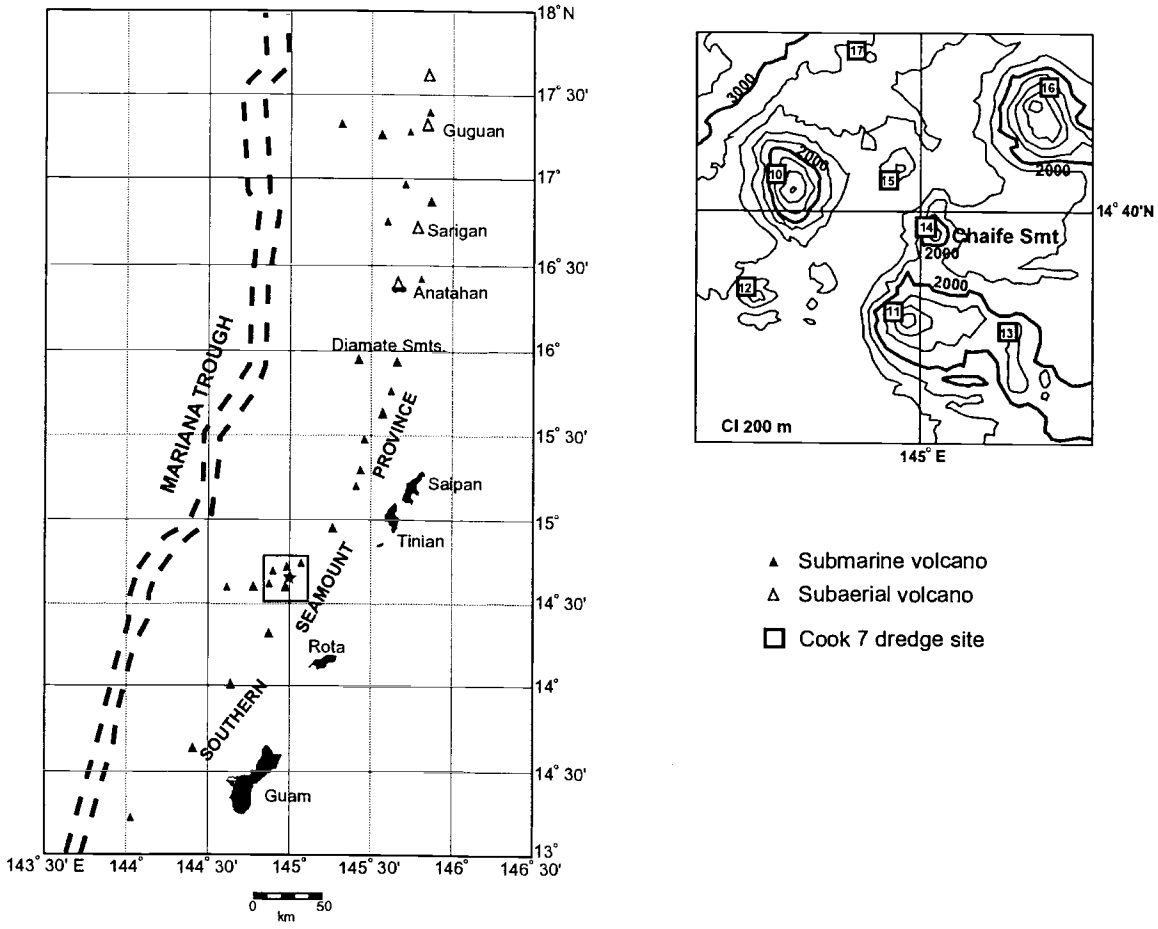

Figure 28: Map showing the location of the Chaife Smt. (star) in the Mariana arc. Inset shows bathymetry and locations dredged by Cook 7 expedition, Apr. 2001. Picritic and ankaramitic lavas sampled from Chaife Smt. by dredge 14 (D14). Note cross-arc chains of seamounts in the vicinity of Chaife.

Millipore system including an Elix reverse osmosis and electrodeionization unit and a Milli-Q Element final purification unit.

Trace and rare earth elements were analyzed on a Perkin Elmer—Sciex Elan 6100 DRC (dynamic reaction cell) inductively coupled plasma mass spectrometer (ICP-MS). External calibration standards were prepared from SCP multi-element ICP-standards. Samples were introduced to the ICP via an auto-sampler at a flow rate of 1 ml min^{-1}. Samples were nebulized using a cross-flow nebulizer and ryton Scott spray chamber. Typical operating conditions are 0.90 L min^{-1} nebulizer gas flow, 1.30 L min^{-1} auxiliary gas flow, 13 L min^{-1} plasma gas flow at an operating RF voltage of 1100 W. The ion lens is optimized at the start of each run and the voltage is dynamically modified by the

instrument software to optimize analyte signal for masses of In and lower. To monitor for drift, a calibration standard and a CRM are run after every five unknowns. Procedural blanks are typically near or below detection for the operating conditions.

$^{87}Sr/^{86}Sr$ was determined using the Finnigan MAT 261 solid-source mass spectrometer at UTD. Reproducibility of $^{87}Sr/^{86}Sr$ is ± 0.00004. During the course of this work the UTD lab obtained a mean $^{87}Sr/^{86}Sr = 0.70803 \pm 3$ for several analyses of the E &A $SrCO_3$ standard; data reported here have been adjusted to correspond to a value of 0.70800 for the E&A standard. $^{143}Nd/^{144}Nd$ was also determined using the UTD Finnigan-MAT261 in the dynamic multicollector mode. Calculations of εNd using values of εNd for the UCSD standard (-15.2) and BCR (-0.16)(Pier et al., 1987). A total range of ± 0.00002 observed for $^{143}Nd/^{144}Nd$ of the standard (mean value = 0.511868) is taken as the analytical uncertainty for the samples. Pb was separated using the technique of Manton (1988) and isotope ratios were also determined at UTD using the MAT 261 in the static multicollector mode and corrected for fractionation using our lab's results for the NBS-981 standard analyzed under the same conditions. Total processing blanks for Sr, Nd, and Pb are <0.1, <0.3, and <0.3ng, respectively. Hf isotopes were analyzed by ICP-MS-MC at Washington State University. Over the period of the past year the $^{176}Hf/^{177}Hf = 0.282146 \pm 0.000010$ (2 standard deviation, n=63). This number is without any bias factors applied other than the standard exponential mass bias correction. Standards within single days reproduce within a total range of about 0.000010.

Phase and Melt Inclusion Compositions

The compositions of phases observed in thin-section were determined using the Cameca SX-50 EMP at Oregon State University. Beam conditions were 1 μm spot size, 50 nA at 15 kV for olivine, clinopyroxene and spinel and 3 μm, 30 nA and 15 kV for feldspar and glass. Pyroxene analyses used count times of 10s for Na, Mg, Al, K, Ca, Ti and Mn and 20s for Si, Cr, and Fe, while olivine analyses used count times of 20s for Ni and 10s for Na, Mg, Al, Si, Ca, Ti, Cr, Mn and Fe. Spinel analyses had count times of 10s for all elements Count times for groundmass glass were 10s for Na and Ca, 15s for Cr, 20s for Mg, Al, Si, K, Ti, Mn, and Fe, 30s for P and S and 1000s for Cl. Accuracy and precision were determined by analyzing standards as unknowns. These standards were USNM 133868 and 122142 for feldspar, USNM 2566 for olivine, USNM 122142

for pyroxene, USNM 113498/1 VG-A99 for glass, and USNM 117075, 6575, and 114887 for spinel.

For melt inclusion analyses, we used whole olivine phenocrysts separated from the bulk rock and heated to eliminate any post-entrapment recrystallization. The separated olivine grains were heated within Pt "boats" suspended in a Deltec vertical quench furnace. Olivine grains were first pre-heated at 1000° C for 45 minutes, then at the desired re-homogenization temperatures of for 15 minutes. After heating, the samples were drop quenched in water. Re-homogenization temperatures were determined using the Fo contents obtained from EMP analyses of olivines in thin-sections and the equation $T_{rehom.}$= Fo/0.0496-571.6734 derived by Danyushevsky et al (2002). Oxygen fugacity was set at the QFM buffer using CO_2-H_2 gas mixing. Olivines were then mounted in epoxy and polished to expose inclusions.

Major elements, Cl and S were analyzed with the Cameca SX-50 EMP at Oregon State University using the glass analysis routine just described. Accuracy and precision were determined as before for the phase chemistry analyses. Trace elements concentrations were determined by laser ablation ICP-MS at Oregon State University. Ablation was performed by a Lambda Physik Compex 102 Excimer laser operating at 193 nm with a 10 μm spot size and analyses by a PQ ExCell ICP-MS. Calibrations were done using NIST 620, NIST 612, BCR-2G and BHVO-2G standards. Concentrations were corrected using MI CaO contents from EMP analyses. Due to the small size of many of the melt inclusions, many analyzed by EMP and FTIR lacked sufficient material to obtain good LA-ICP-MS data.

We used the Fourier Transform Infrared spectroscopy method (FTIR) to determine water content of a select number of inclusions. The host grains and inclusions were doubly polished to thicknesses of 90-160 μm. Analyses were performed with the Thermo Nicolet 670 FTIR operated by Omnic software at the University of Oregon under the direction of Paul Wallace. Water contents were measured using the 3530 nm OH peak and glass densities of 2022-2300 cm^3/mol. Densities were calculated from the composition using the parameters outline in Wallace (2002). Initial analyses were done on inclusions that had been re-homogenized and previously analysed by EMP. The results of the intial FTIR analyses indicated that most of the inclusions had lost volatiles

during re-heating. We then examined a number of olivine phenocrysts for inclusions that appeared to have little post-entrapment crystallization, i.e. naturally glassy. These phenocrysts were doubly-polished to expose the inclusions and analyzed with FTIR. These inclusions were subsequently analyzed by EMP for major elements.

Melt inclusion compositional data were corrected for over or under-heating by adding or subtracting olivine of the host crystal composition until melt/host FeO/MgO ratio agreed with the equilibrium olivine-liquid FeO/MgO k_D of 0.3 (Roeder and Emslie, 1973, Ford et al., 1983). Potential Fe loss in MI resulting in incorrect Mg#s may occur when reheating fails to melt post-entrapment Fe-enriched olivine that crystallized along the inclusion walls. We used the method of Danyushevsky et al., (2002) in a software algorithm to correct any Fe error due to this phenomenom.

RESULTS

Petrography

The Chaife lavas can be classified on the basis of mineral mode and texture as ankaramite (D14 type 1) and picrite (D14 type 4). The picrite was a medium gray vesiculated, porphyritic rock with a thin (~0.2 mm) veneer of Mn. Vesicles were round to lobate and ~0.6-2 mm in size. Rare ~80 mm crystal clots of olivine, pyroxene and spinel were also observed. The lava was determined to be 58 vol.% phenocrysts, 27 vol.% groundmass, and 16 vol.% vesicles. The groundmass was vitrophyric and varied from quenched crystals of plagioclase in glass to diabasic CPX and feldspar with minor interstitial glass. Phenocryst assemblages were 58 % olivine, 34% CPX, 6% spinel and minor plagioclase. Both olivine and CPX were 0.3 to 3 mm in size and present as euhedral crystals with smooth faces, which attests to a magmatic origin (Figure 29). Spinels were more common as inclusions than as phenocrysts and both olivine and CPX frequently included spinel. A few CPX inclusions in olivine were observed. Rare plagioclase phenocrysts (<1 vol%) were subhedral with albite twinning, and some fritted margins. Otherwise, plagioclase occurred only as a groundmass phase. Based on these observations we determined that the crystallization history was Ol→Ol+Cr-sp→ Ol+Cr-sp+CPX→groundmass.

Polycrystalline aggregates, or crystals clots, were rare and generally consisted of several adjoining olivine and CPX similar in size to the phenocrysts. One larger crystal

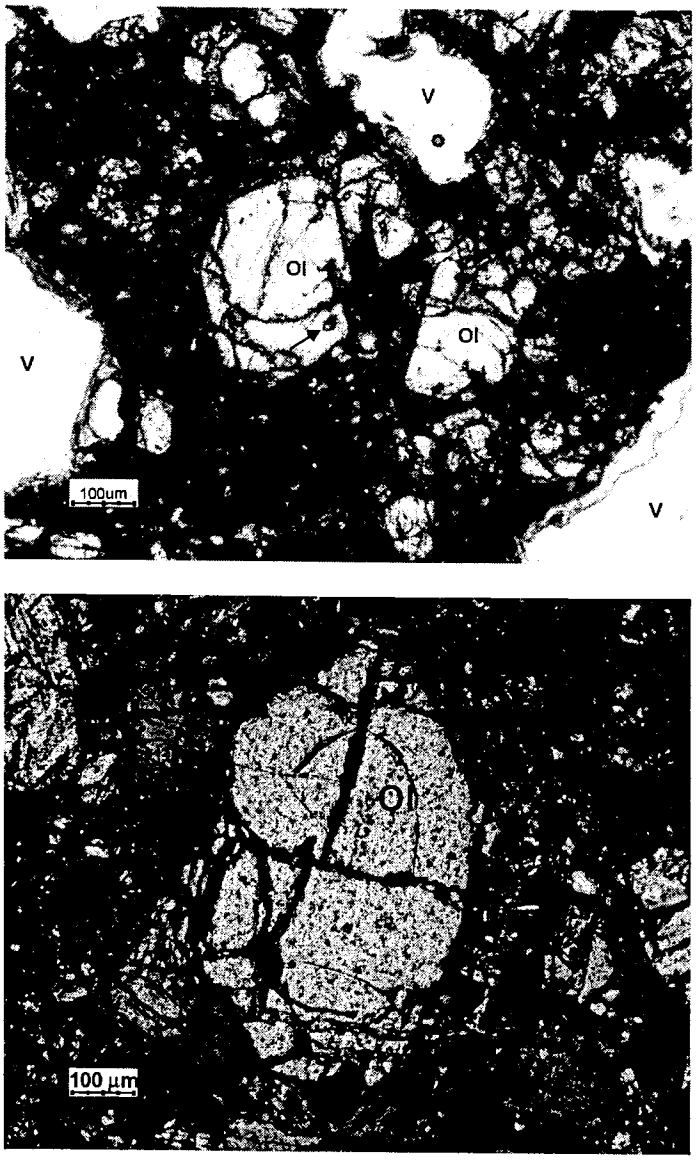

Figure 29: Photomicrographs showing euhedral olivine phenocrysts (Ol) in glassy vesiculated (v-vesicles) groundmass of picrite. Smooth faces, prismatic morphology and melt inclusions (arrow) attest to magmatic origin. Top-plane light, bottom-crossed polars.

clot examined was ~80 mm in diameter and consisted of ~90% 0.8-2mm olivine with a lesser amount of CPX and interstitial spinel. Glass was also interstitial along some grain boundaries. In the large crystal clot, the minerals differed from the phenocrysts in that they were subhedral, and CPX were usually smaller than the olivine. Melt and spinel inclusions were not present in the olivines in this clot. In both the small and large crystal clots, olivines and CPX were unstrained.

The ankaramitic lava was more phyric than the picrite: 65% phenocrysts, 25% diabasic groundmass and 10% vesicles. The latter were generally round and ~0.05-1 mm in size. The smaller size of these vesicles relative to those in the picrite indicate that the ankaramite erupted at a greater depth. Phenocryst assemblages were ~45 vol% CPX and 25 vol% olivine. The groundmass consisted of diabasic CPX and plagioclase with minor olivine and Cr-spinel. Crystal clots were absent. Clinopyroxene phenocrysts were 0.5-2 mm in size and were generally larger than olivine, which ranged from 0.1-1mm. The crystallization sequence was similar to the picrite, but without significant spinel crystallization and a shorter period of olivine only crystallization.

Whole Rock/Phase Composition and Age

The lavas we recovered were primitive with Mg#s (assuming all Fe as FeO) of ~76 (Table 13). Based on bulk composition, both lavas can be classified chemically as picrite using the IUGS classification scheme (LeBas, 2000), but we will continue to use the textural classification in this paper for clarity. In the picrite, MgO contents ranged from 14.80-14.95 wt% MgO, total alkalis were <2 wt%, Al_2O_3 contents were ~10.3 wt% and the concentration of TiO_2 was 0.5 wt%. The CaO/Al_2O_3 numbers were 1.35-1.36 (Table 13). The average composition of the groundmass glass was 7.97 wt% MgO (Mg# of 60.1), 15.26 wt% Al_2O_3, 0.71 wt% TiO_2 and 2.20 wt% total alkalis. The ankaramite was virtually identical in composition, with slightly higher Mg#s and CaO/ Al_2O_3 values of 1.55-1.41 (Table 13).

Overall, the lavas were isotopically similar to typical Mariana arc lavas. The $^{87}Sr/^{86}Sr$ values (Table 13) fell within the range of 0.7030-0.7040 for the IBM system, and were greater than that of N-MORB (0.7028-Ito, 1982) or Mariana Trough back-arc basin basalts (0.70304- Stern et al., 2000). The εNd values were +6.06-6.82, which is lower than MORB, but again typical for Mariana magmatic front lavas, which have a mean of +6.7 (Figure 30a). The Pb isotopes had $^{206}Pb/^{204}Pb$ values of 19.015-19.047, slightly more radiogenic than most Mariana arc lavas which plot near the IBM system mean of 18.85 (Figure 30c and d). The Δ7/4 and Δ8/4 values reported in Table 13 are deviations from the Northern Hemisphere Reference Line (NHRL), a trajectory devised by Hart (1984) that describes the Pb isotopic characteristics of non-subduction related oceanic volcanoes. Elevated levels of Δ7/4 and Δ8/4 in arc lavas from the region can be

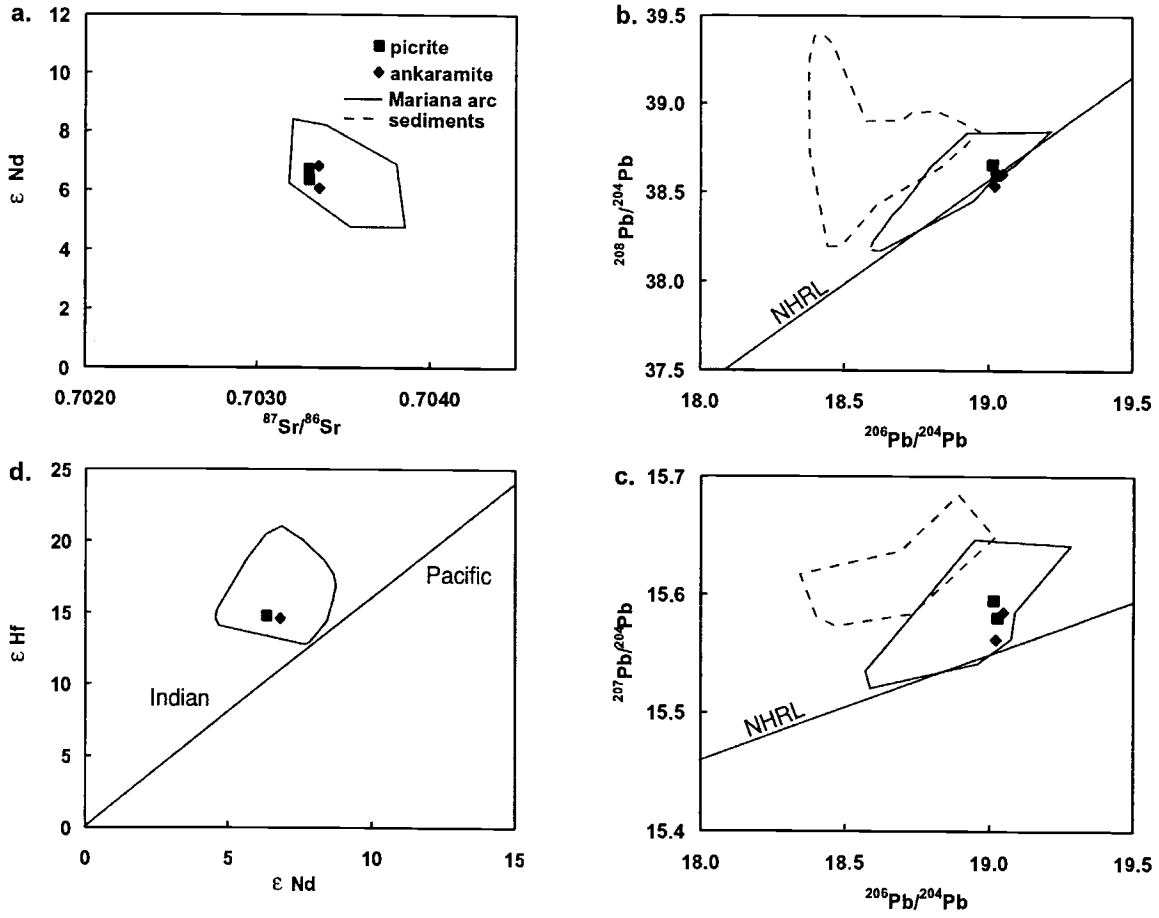

Figure 30: Isotopic characteristics of Chaife seamount lavas. Solid line encloses Mariana arc compositions and dashed line encloses sediment after Stern et al., 2003. NHRL is Northern Hemisphere Reference Line of Hart (1984) see text for explanation. Chaife lavas are isotopically similar to other Mariana arc lavas and tap an Indian Ocean type mantle.

Table 13. Chemical composition of Chaife Seamount Lavas

	D14-1-4 ankaramite	D14-1-5 ankaramite	D14-4-1 picrite	D14-4-2 picrite
SiO_2 %	48.24	47.94	48.52	48.70
TiO_2	0.47	0.47	0.48	0.49
Al_2O_3	9.09	9.94	10.29	10.30
FeO*	8.21	8.22	8.35	8.33
MgO	15.36	15.23	14.95	14.80
MnO	0.15	-	0.15	0.15
K_2O	0.52	0.53	0.42	0.42
Na_2O	1.43	1.41	1.38	1.28
CaO	14.09	14.04	13.90	13.98
P_2O_5	0.09	0.09	0.10	0.09
Total	97.65	97.87	98.54	98.54
Mg#	76.93	76.76	76.15	76.01
CaO/Al_2O_3	1.55	1.41	1.35	1.36
Sc ppm	55.00	54.00	54.00	54.00
V	230.00	229.00	231.00	235.00
Cr	-	808.25	874.96	-
Co	-	52.81	49.24	-
Ni	-	213.77	187.45	-
Cu	-	52.23	79.60	-
Zn	-	76.57	93.32	-
Rb	-	5.46	8.32	-
Sr	328.00	327.00	339.00	340.00
Y	9.00	9.00	10.00	10.00
Zr	24.00	22.00	25.00	21.00
Nb	-	0.84	0.87	-
Cs	-	0.24	0.30	-
Ba	86.00	87	89	87.00
La	-	3.76	3.98	-
Ce	-	8.58	12.6	-
Pr	-	1.17	1.23	-
Nd	-	5.73	5.92	-
Sm	-	1.64	1.68	-
Eu	-	0.59	0.56	-
Gd	-	1.94	1.91	-
Tb	-	0.32	0.32	-
Dy	-	1.77	1.75	-
Ho	-	0.38	0.39	-
Er	-	1.06	1.1	-
Tm	-	0.15	0.15	-
Yb	-	0.97	1.04	-
Lu	-	0.16	0.17	-
$^{87}Sr/^{86}Sr$	0.703362	0.703359	0.703306	0.703303
$^{143}Nd/^{144}Nd$	0.512938	0.512977	0.512952	0.512971
εNd	6.06	6.82	6.35	6.71

Table 13. Continued

	D14-1-4	D14-1-5	D14-4-1	D14-4-2
$^{176}Hf/^{177}Hf$	-	0.283185	0.283190	-
εHf	-	14.59	14.77	-
$^{206}Pb/^{204}Pb$	19.022	19.047	19.015	-
$^{207}Pb/^{204}Pb$	15.562	15.585	15.595	-
$^{208}Pb/^{204}Pb$	38.536	38.603	38.656	-
Δ7/4	0.902	2.931	4.277	-
Δ8/4	-8.8598	-5.1823	3.9865	-
Age	1.76±0.06 Ma.		2.49±0.18 Ma.	

interpreted as indications for the mixing of subducted sediments in the mantle source region, as western Pacific sediments have Δ7/4 > NHRL (Stern et al., 2003). The picrite had a Δ7/4 of 4.277, which was not substantially different than the mean Δ7/4 for the IBM system(4.4), while the ankaramite Δ7/4 numbers were significantly lower at 0.902-2.9377 (Table 13). The Δ8/4 values were also significantly different between the two lavas, with +3.9865 for the picrite and –8.8598 to –5.1823 for the ankaramite. The Δ8/4 numbers are less diagnostic in terms of subduction input, and might reflect differences in mantle domains. However, based on the parameters defined in Pearce et al. (1999) the $^{176}Hf/^{177}Hf$ and εHf data were consistent with Indian ocean type mantle. Pearce et al. (1999) placed the Indian-Pacific mantle boundary at εHf=1.6* εNd, and the Chaife lava's εHf data were equivalent to 2.14-2.33 * εNd values. These are well within the Indian domain (Figure 30d), which IBM magmas have tapped for at least 50 Ma. (Pearce et al., 1999). The differences in Δ7/4 and Δ8/4 between the two lavas may more accurately reflect a smaller subduction signal in the ankaramite rather than differences in mantle source domains.

In the picrite, olivine phenocrysts were $Fo_{87.8-92.0}$ (Table 14), CPX had compositions of $Wo_{44.5-47.9}$, $En_{43.8-51.7}$ and $Fs_{2.9-6.2}$ (Table 15), and chromites had Cr#s (Cr/Cr+Al) of 0.60-0.77 and Mg#s (Mg/Mg+Fe^{2+}) of 0.59-0.93 (Table 16). The rare plagioclase phenocrysts were very calcic with compositions of An_{90-92}. Olivine and CPX commonly had less magnesian rims, but these were typically only 5-30μm and the phencrysts were largely unzoned. The olivine and CPX observed in crystal clots or

clusters were chemically identical to the most primitive examples of these phases observed as single crystals. Concentrations of Mn and Ca increased and Ni decreased with decreasing Fo contents of the olivines. The Mn and Ni data plotted along continuous trends from the most primitive phenocrysts to groundmass, pointing to a magmatic origin (Figure 31). The variation of Ca vs. Fo shows that while most phenocrysts also fell along a continuous trend, there was a steep decrease in CaO at high Fo contents. Olivines with <0.1 wt% CaO included ones in the large crystal clot described earlier. These data suggest that that large clot was potentially xenocrystic. However, the NiO content of the olivines in the large polycrystalline aggregate are less than 0.2 wt% while olivines from abyssal peridotites have NiO of 0.28-0.41 wt% at Fo_{90-91} (Dick, 1989; Elthon et al. 1992) and the source rock was unlikely to be fertile peridotite. If the crystal clot was indeed xenocrystic, it would appear possible that some of the low-Ca phenocrysts came from disaggregated xenoliths. However, these particular olivines have identical morphologies to phenocrysts with higher Ca concentrations and display no evidence for resorption. Xenocrysts would be in disequilbrium with the melt that entrained them and would be expected to have morphological evidence for resorption such as fritted margins and rounded faces. It is also not likely that xenocrysts would have other minor element concentrations that co-vary with Fo along continuous trends to groundmass compositions. The few phenocrysts with >0.3 % NiO (Figure 31) do not have the lowest CaO concentrations, which would be expected if they were mantle xenocrysts. Instead it is likely that low-CaO olivines were phenocrysts formed at greater depths and/or temperatures, based on studies of olivine phase equilibria (Simkin and Smith, 1970; Ford et al, 1983). Even if some of the very low-Ca (>0.1 %) olivine were xenocrysts, it would not effect our interpretation of melt inclusion data as none were gathered from olivines <0.15 wt% CaO. The composition of olivine phenocrysts in the ankaramite were nearly identical to those in the picrite, although most had CaO contents <0.2 wt% (Table 14). CPX phenocrysts were also similar between the two lava types, with the exception of Cr, which was ~0.04-0.15 wt% higher at a comparable Mg# in the ankaramite (Table 15).

The lavas were dated using the $^{39}Ar/^{40}Ar$ method by John Huard and Robert Duncan at the Noble Gas Mass Spectrometry lab at Oregon State University. The groundmass for the picrite was found to have a plateau age of 2.49±0.18 Ma. while the

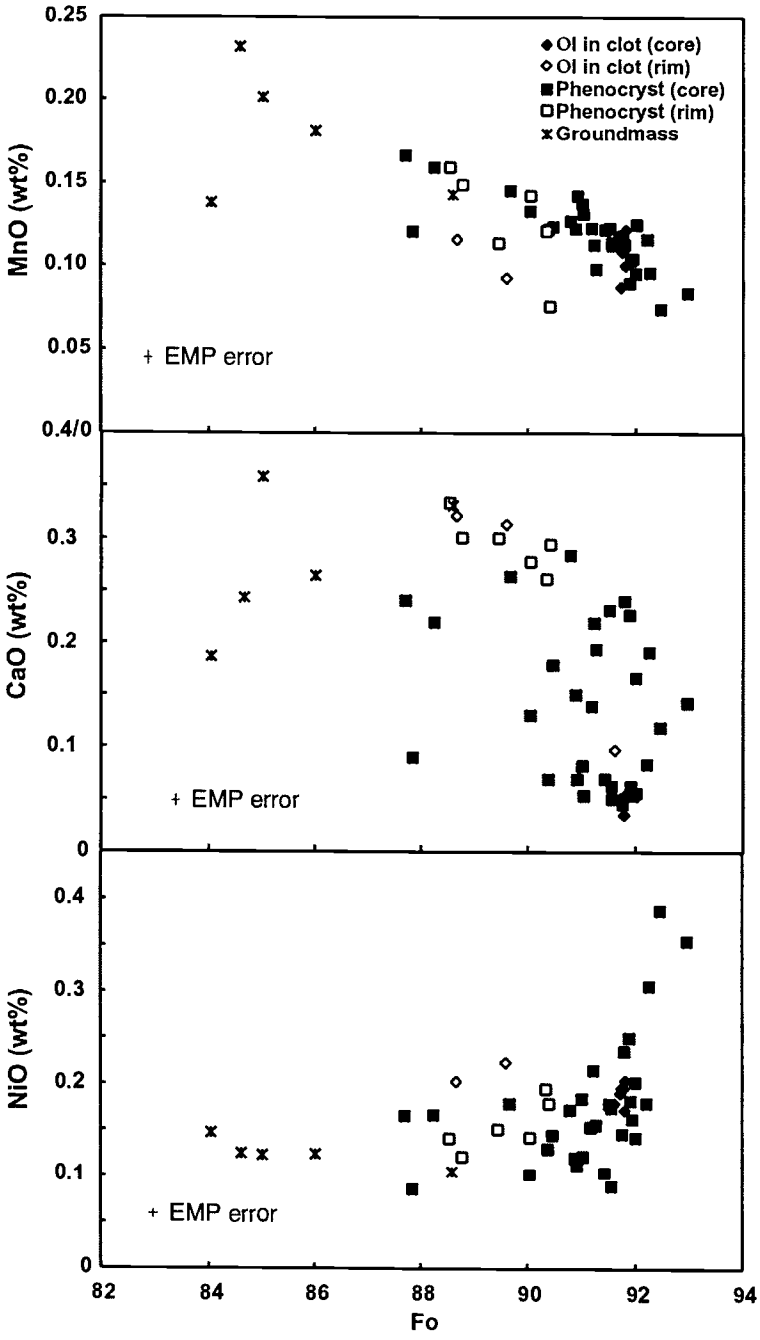

Figure 31: Trace element compositions of olivine in the picrite. Continuous trends from high-Fo phenocrysts to groundmass olivine support magmatic origin for phenocrysts. High Ni olivine phenocrysts do not correspond to very low Ca phenocrysts (see text).

Table 14 Representative Olivine Analyses (cores)

	1	2	3	4	5	6	7	8	9	10	11	12	13	14
SiO_2 %	39.51	39.61	38.72	40.03	39.91	40.25	40.48	40.21	38.19	38.70	38.12	38.62	38.44	38.04
Cr_2O_3	0.00	0.00	0.01	0.01	0.02	0.03	0.04	0.04	0.02	0.11	0.08	0.06	0.07	0.04
FeO*	8.08	8.16	11.42	11.25	9.97	9.62	8.38	8.06	14.85	8.42	9.13	10.33	8.14	14.50
MgO	50.67	50.77	46.32	47.43	48.61	48.89	50.78	51.69	43.88	48.71	48.30	48.10	52.66	45.26
MnO	0.11	0.09	0.12	0.16	0.15	0.13	0.12	0.10	0.14	0.15	0.15	0.15	0.13	0.14
NiO	0.20	0.19	0.09	0.17	0.18	0.10	0.18	0.16	0.15	0.25	0.15	0.15	0.15	0.10
Na_2O	0.02	0.00	0.03	0.02	0.01	0.03	0.02	0.02	0.02	0.00	0.01	0.01	0.03	0.00
CaO	0.04	0.05	0.19	0.22	0.26	0.13	0.17	0.05	0.29	0.13	0.15	0.20	0.08	0.24
Fo	91.8	91.8	87.8	88.3	89.7	90.1	91.5	92.0	84.0	91.2	90.4	89.20	92.00	85.20

1,2 Olivine in crystal clots in picrite
3-8 picrite phenocrysts
9 picrite groundmass
10-13 ankaramite phenocrysts
14 ankaramite groundmass

Table 15 Representative CPX Analyses (cores)

	1	2	3	4	5	6	7	8	9	10	11	12	13	14
SiO_2 %	54.03	53.80	52.82	51.83	50.89	52.48	52.63	51.76	52.00	50.80	51.74	51.06	55.44	49.33
TiO_2	0.16	0.16	0.13	0.18	0.24	0.14	0.12	0.18	0.18	0.18	0.13	0.19	0.12	0.44
Al_2O_3	1.19	1.30	1.19	2.31	2.84	1.33	1.66	1.91	2.21	2.22	1.45	2.22	1.56	3.96
Cr_2O_3	0.31	0.37	0.85	0.57	0.39	0.98	0.82	0.62	1.40	1.09	0.56	0.88	0.81	0.17
FeO*	2.01	1.91	2.80	3.48	3.94	2.73	3.11	3.46	3.56	3.52	3.40	3.49	2.86	5.41
MgO	18.14	18.02	18.35	17.16	16.69	17.91	17.69	17.54	17.58	17.18	18.49	17.09	16.19	16.39
MnO	0.08	0.07	0.05	0.07	0.14	0.09	0.11	0.07	0.08	0.07	0.08	0.07	0.07	0.12
Na_2O	0.10	0.12	0.11	0.12	0.08	0.11	0.10	0.10	0.11	0.13	0.10	0.13	0.12	0.13
CaO	24.18	24.45	22.25	22.62	23.13	22.71	22.51	22.43	21.77	21.82	21.42	21.73	22.16	21.20
Wo	47.4	47.9	44.5	46.0	46.8	45.7	45.4	45.3	44.4	45.0	43.0	45.1	47.2	44.0
En	49.5	49.2	51.1	48.5	5.5	6.2	4.3	49.3	4.9	49.3	51.7	49.3	48.0	47.3
Fs	3.1	2.9	4.4	5.5	6.2	4.3	4.9	5.5	5.7	5.7	5.3	5.6	4.8	8.8
Mg#	94.1	94.4	92.1	89.8	88.3	92.1	91.0	90.0	88.8	89.7	90.7	89.7	91.0	84.4

1,2 Olivine in crystal clots in picrite
3-8 picrite phenocrysts
9 picrite groundmass
10-13 ankaramite phenocrysts
14 ankaramite groundmass

Table 16 Representative Spinel Analyses

	1	2	3	4	5	6	7	8	9	10
SiO_2 %	0.00	0.01	0.02	0.02	0.03	0.01	0.06	0.03	0.02	0.13
TiO_2	0.39	0.41	0.26	0.37	0.37	0.35	0.37	0.35	0.40	0.46
Al_2O_3	20.58	18.41	12.45	11.75	11.60	11.89	10.77	17.14	12.42	15.26
Cr_2O_3	39.31	40.93	47.74	41.20	40.99	40.79	53.85	43.56	47.65	46.96
Fe_2O_3	1.92	2.13	3.48	17.55	16.76	15.74	9.25	12.56	13.09	10.60
FeO	22.41	23.76	18.91	15.05	15.31	15.81	11.51	9.84	12.07	10.12
MgO	14.76	13.66	15.79	12.50	12.73	12.94	14.78	16.24	14.40	16.00
MnO	0.17	0.23	0.28	0.23	0.21	0.21	0.17	0.22	0.24	0.18
VO_2	0.12	0.09	0.05	0.12	0.12	0.11	0.06	0.12	0.13	0.12
ZnO	0.13	0.20	0.14	0.09	0.20	0.15	0.02	0.09	0.04	0.11
Cr#	0.56	0.60	0.72	0.70	0.70	0.70	0.77	0.63	0.72	0.67
Mg#	0.93	0.93	0.87	0.59	0.60	0.62	0.70	0.75	0.68	0.74

1 Spinel in crystal clot
2-6 spinel as phenocryst
7-10 spinel included in olivine

ankaramite groundmass was dated at 1.73±0.06 Ma. In comparison, the maximum age of volcanism along the Mariana volcanic arc is considered to be 3-4 Ma.. This constraint is provided by the minimum age of the latest rifting event in the arc that produced the currently active Mariana Trough (Stern et al., 2003).

Melt Inclusion Compositions

The number of inclusion hosting olivines in both lavas was small (~10%). Consequently, we concentrated our melt inclusion (MI) analyses on those from the picrite, which provided more inclusions to work with due to its greater abundance of olivine. In general, melt inclusion compositions were more primitive than the host lava, with median Mg# of 79.06 and a maximum of 81 (Table 17). Many of the melt inclusions had komatiite-like compositions (LeBas, 2000), with greater than 18% MgO and < 2% total alkalis. Compositional trends for most MI projected along a liquid line of descent through the host lava composition to groundmass glass, indicating a genetic relation between the melt trapped in olivine phenocrysts and the lava (Figure 32). Major element compositions regressed to 8 % MgO corresponded to groundmass glass compositions and were also similar to many primitive arc basalts (e.g. BSVP, 1980; Nye and Reid, 1986; Tatsumi and Eggins, 1995).

Melt inclusions normative assemblages were close to the critical plane of silica undersaturation on the basalt tetrahedron (Yoder and Tilley, 1962), and in general the least magnesian were hypersthene normative olivine tholeiites, while the most primitive were slightly nepheline normative (Table 17). Projection of normative compositions onto the Fo-Di-An side in the quaternary system Fo-Di-An-Ab (Yoder and Tilley, 1962) reveals that the most can be divided into two groups. The first group plotted along a crystallization path from the Fo endmember towards the An-Di sideline and included the most magnesian and nepeheline normative MI (A-Figure 33). The other group of MI normative compositions largely clustered together in a location that corresponded with the higher pressure Fo-Di cotectics described by Presnall et al. (1978) and Grove et al. (1992) for the system (B-Figure 33). Normative compositions based on whole rock analyses of the picrite correlated with the MI norms at the higher pressure cotectic, while groundmass glass norms plotted near the 1 atm Ol-An cotectic (Osborn and Tait, 1952). Compositions on the Fo-Di cotectic that are related to the A norms would plot from the

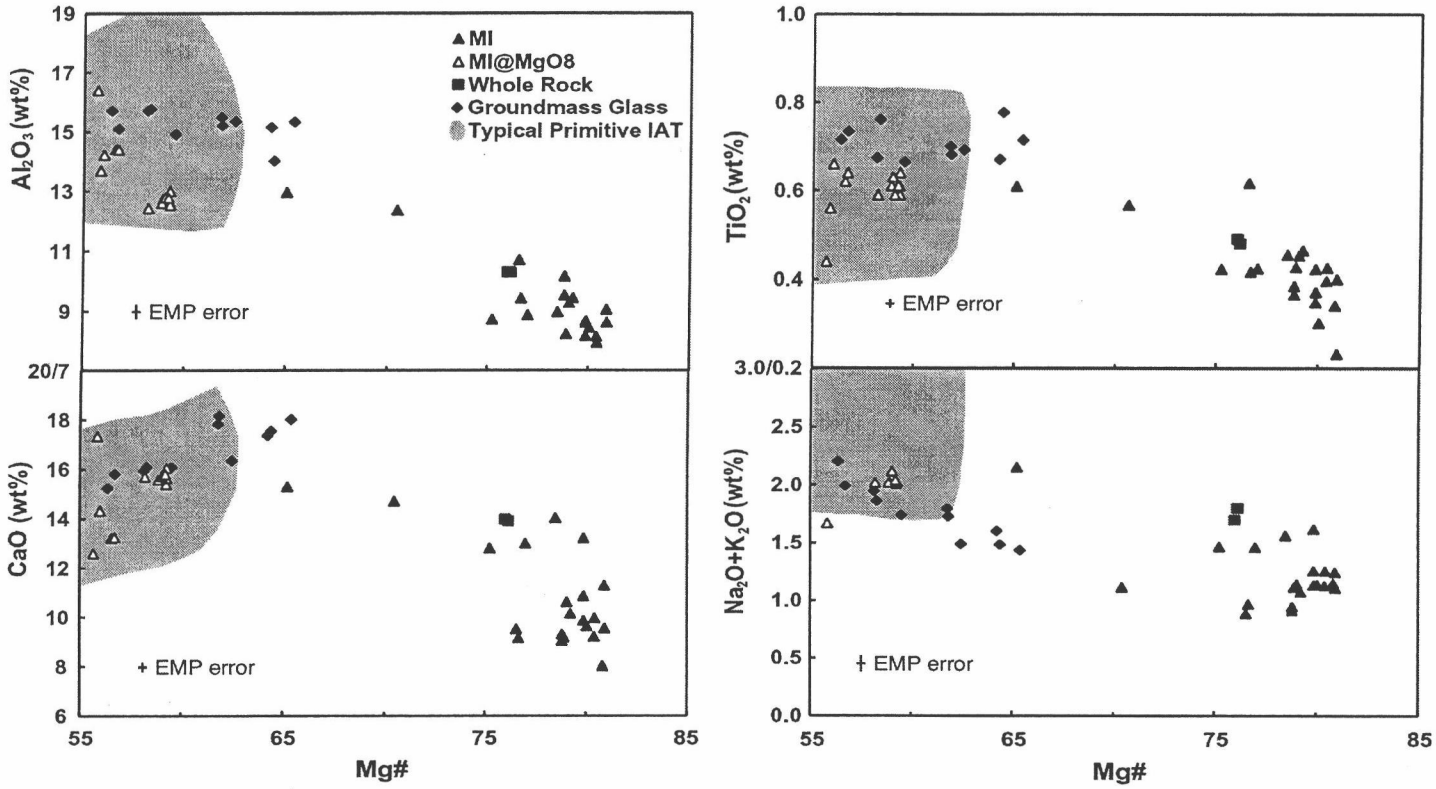

Figure 32: Variation of major element compositions with Mg# (at% $Mg/Mg+Fe^T$). MI are melt inclusions, MI @MgO8 are melt inclusion compositions regressed to 8% MgO. Shaded areas are for typical primitive (~8% MgO) island arc tholeiites. Most MI compositions fall along trends through the host glass to groundmass glass. This indicates a genetic relationship and melt included in olivine phenocrysts are parent magmas for the picrite. MI @MgO8 compositions suggest that these magmas could theoretically evolve to more common arc tholeiites.

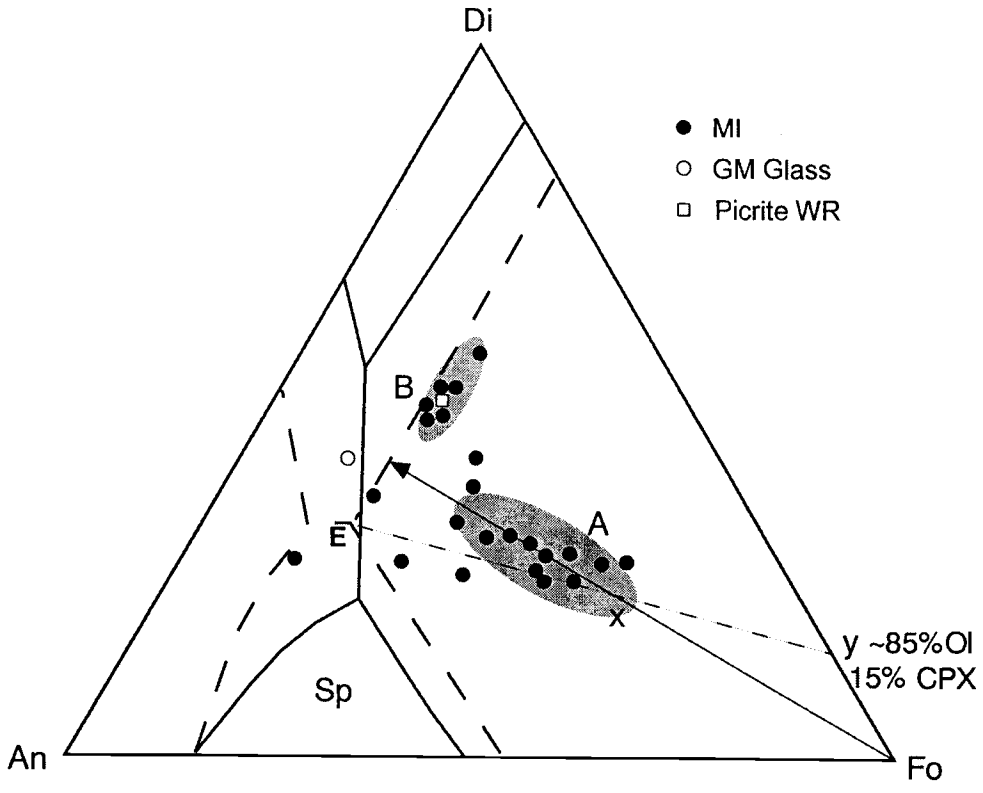

Figure 33: Normative proportions of Di, An, and Fo of melt inclusions, whole rock and groundmass glass compared to 1 atm. phase boundries (solid line) of Osborn and Tait (1952) and 7 kbar. phase boundaries (heavy dashed line) of Grove et al. (1992). Group A compositions appear to line on crystallization path, Group B on the Ol-Di cotectic. Group A compositions could not evolve to B along cotectic and this may indicate two separate liquids (see text). Light dashed line from the eutectic (E) through approximate location of the most parental A group melt (x) to Di-Fo sideline (y) indicates ultimate crystallizing assemblages of Group A liquids on cotectic to eutectic. Proportions at y do not concur with modal assemblage of picrite and may indicate Group A MI represent an added, high MgO melt.

point where the trend and cotectic intersected, along the cotectic towards the eutectic (E-Figure 33). The norms of group B instead plot towards the Di endmember. A line drawn from the eutectic to through a possible parent for the group A compositions (x-Figure 33) to the Fo-Di sideline would crystallized a solid of ~85% olivine and 15% (y-Figure 33). This does not correspond with the lava modal assemblages determined petrographically, but may indicate that large crystal clot may be the result of crystal accumulation from this melt. The two groups of normative compositions appear to indicate the presence of two liquids, and the scattered compositions in between mixing.

Chlorine and sulfur concentrations were measured using EMP. Chlorine contents were generally in the range of 103-334 ppm, although some were as high as 1346 ppm (Table 17). All but the highest Cl inclusion plotted between the mantle Cl/K values of 0.04 and a value of 0.0625 (Figure 34a). Inclusions with very low Cl (<100 ppm) also had low S (Figure 34b), and these MI were likely breached and volatiles were lost during re-heating (Nielsen et al., 1998). Sulfur contents of unbreached inclusions ranged from 1362-2426 ppm (Figure 34b). Water contents measured in unheated inclusions via FTIR ranged from 0.16 to 0.64 wt%, with most in the range of 0.3 –0.5 wt% (Table 17). These were in general lower than the 0.6 to 4.0 wt% primary water contents estimated for most arc magmas (Sakuyama, 1979; Danyushevsky et al., 1993; Gaetani et al., 1993; Sisson and Layne, 1993). Due to the small size of the inclusions, 30-90 μm, we not able to polish the host olivine to a thin enough to expose the inclusions on both sides. As a result, the IR beam had to pass through a layer of host crystal and the resultant SiO_2 peak in the FTIR spectra prevented us from obtaining CO_2 data.

Trace-element concentrations normalized to N-MORB had patterns similar to typical island-arc tholeiites (IAT), but at lower abundances (Figure 35). The LILE were enriched relative to MORB and HFSE, especially Nb and Ta were depleted. No MI examined had a distinctively MORB or OIB-like pattern. In a few of the most depleted MI, which also were nepheline normative and had MgO contents up to 24.16 wt% (8 and 9-Tables 17 and 18), the trace element patterns lacked the characteristic N-MORB normalized Pb spike of IAT. If elevated Pb is suggestive of an added sediment-derived component, then these particular inclusions may have sampled mantle melt without a significant sediment contribution. The MI with the highest normalized trace element concentrations of Ba, Rb, U and Pb were also those with the highest alkalis (1.72-2.53% Na_2O, 0.52-0.72% K_2O) and this group include the inclusion with 1346 ppm Cl. These data seem to indicate the existence of a more alkaline, LILE enriched parent magma.

Co-variation of trace ratios were examined to determine the relative contribution of a subduction derived component to the melts. Variation of trace elements considered to be conserved in the downgoing slab to those that are released during subduction (non-conservative) provide measures of the subduction component in a melt (Pearce and Peate, 1995). We compared Th (non-conservative) to Nb, which is conservative and instead

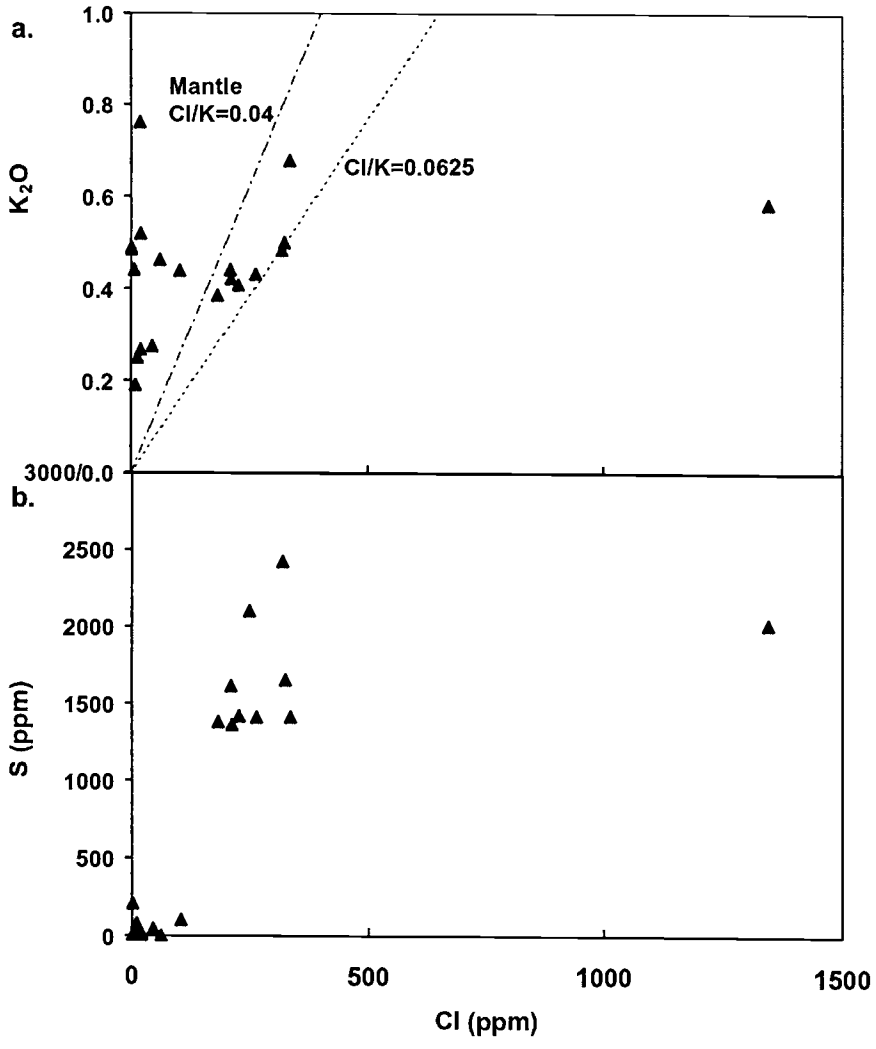

Figure 34: Chlorine systematics of melt inclusions. **a.** Cl vs. K, most MI plot between the mantle value of 0.04 and 0.625, indicating a minor volatile component. One MI has elevated Cl and also has higher LILE and U than most MI. **b.** Low S and Cl inclusions are likely breached and lost volatiles during rehomogenization. No correlation was noted between Cl and S.

indicates the relative depletion of the mantle in the asthenospheric wedge (Figure 36a). These concentrations are Yb normalized after the practice of Pearce and Peate (1995) to minimize partial melting and fractionation effects. The range of Nb/Yb values in the melt inclusions was ~0.6-1, similar to N-MORB (Pearce and Peate, 1995). The Th/Yb values elevated relative to mantle in most MI are interpreted as an added subduction component. The lack of Zr/Yb enrichment above the mantle array (Figure 36b) indicates that melting of the slab did not take place, and the subduction component instead derived from sediment melt and/or aqueous fluid. The relative contributions of aqueous fluid and

sediment were determined by comparison of Nb normalized Th to Ba/Th, U/Th and Pb/Ce (Figure 37). Barium and Pb are present in sediment, but can be mobilized by fluid. Uranium is enriched in aqueous fluids (Hawkesworth et al., 1997), while in contrast Th is present in subducted sediment but is not mobilized by aqueous fluids. An increase in Th/Nb may then result from sediment melting, while elevated Pb/Ce and Ba/Th could arise from either source (Elliot et al., 1997; Class et al., 2000). Melt inclusion compositions had a continuous Th/Nb trend within the range typical of island-arc tholeiites. The values of Ba/Th and Pb/Ce varied directly with Th/Nb, while U/Th decreased. The values of U/Th, Pb/Ce and Ba/Th each had a strong enrichment in single different inclusions analysed by LA-ICP-MS, possibly due to differing effects of fluid contribution (Figure 37). The Th and U data thus indicate contribution from both sediment and fluid, with the sediment signal persisting in a wider range of MI compositions.

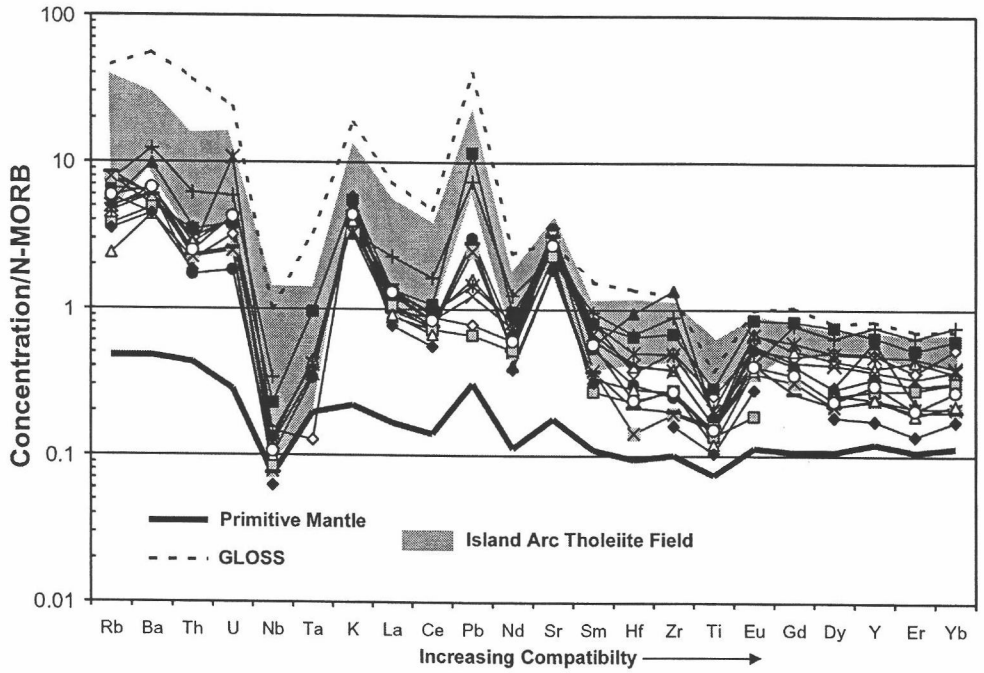

Figure 35: Spider diagram of N-MORB normalized MI trace element concentrations. All MI have arc-like pattern. The most depleted have no Pb peak and Nb below primitive mantle. Primitive Mantle from McDonough and Sun (1995), Global Subducting Sediment (GLOSS) from Plank and Langmuir (1998), Island Arc Tholeiite from Peate et al., (1997) and Taylor and Maclennan (1995).

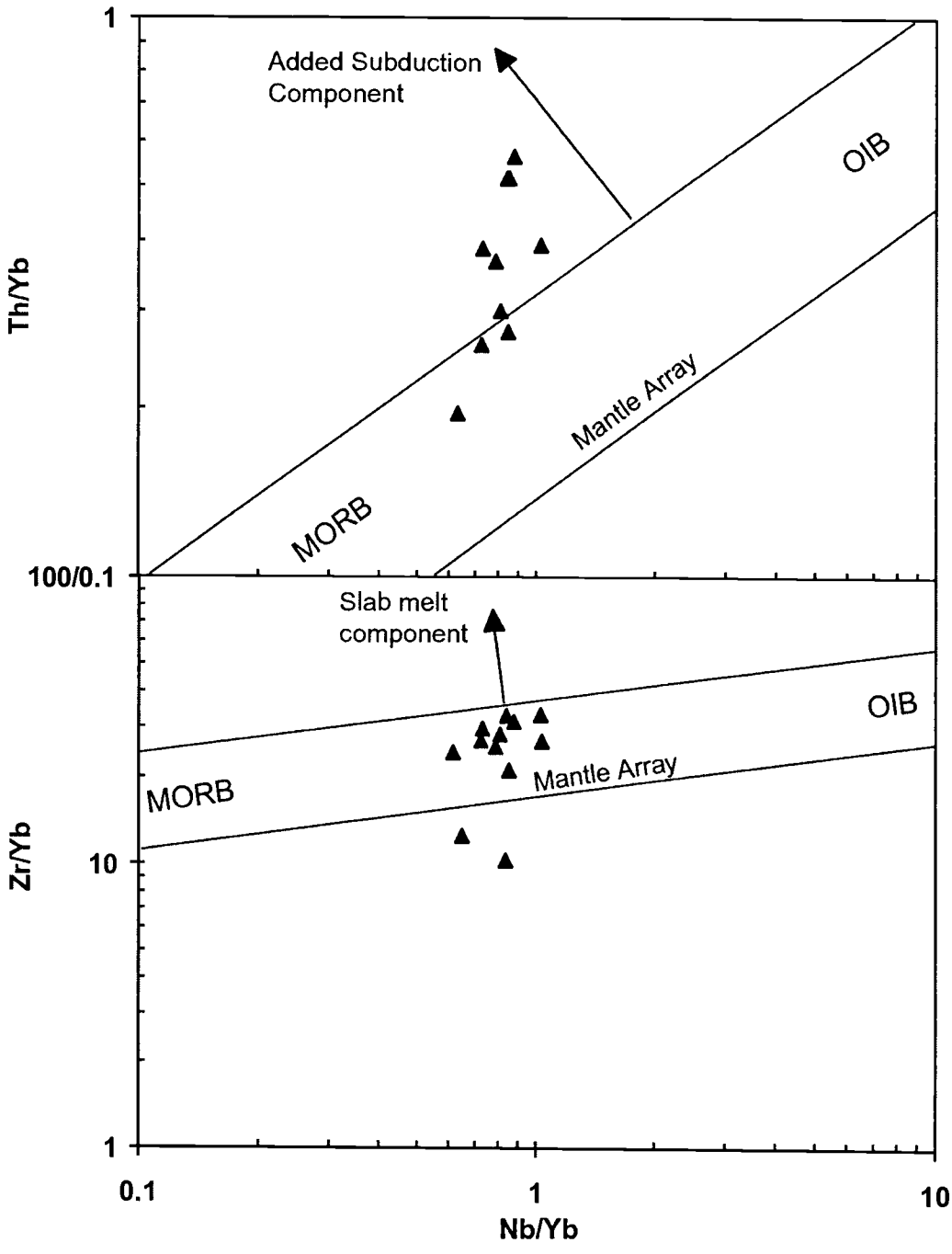

Figure 36: Th/Yb and Zr/Yb variation with Nb/Yb. Elevated Th/Yb above the mantle array indicates the addition of a subduction component, elevated Zr/Yb above mantle is evidence for slab melt. Nb/Yb shows relative mantle enrichment. Most MI have a subduction Th signature, but no evidence of slab melt.

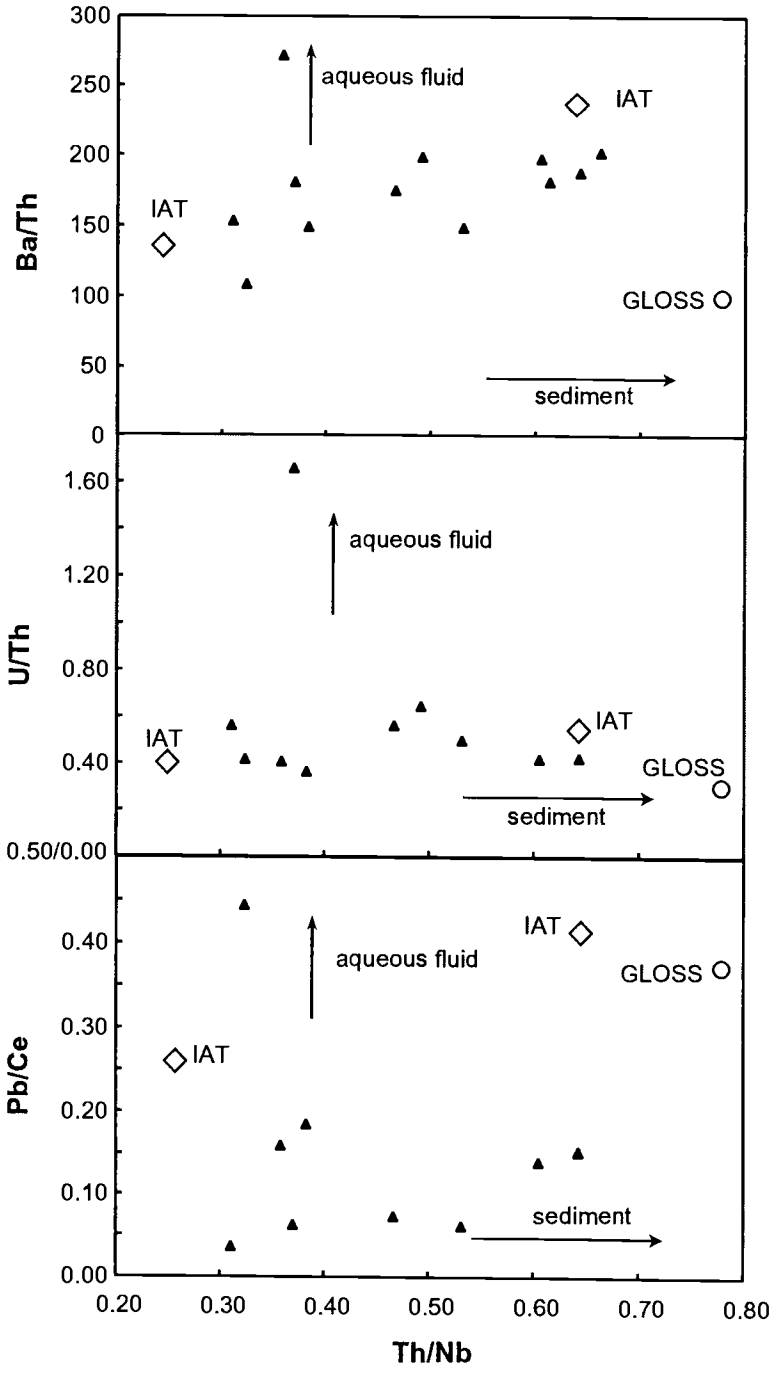

Figure 37: Aqueous fluid and sediment-derived (potentially sediment melt) components in MI compositions. Only a few MI have a mild fluid enrichment signal, most have some sediment signal. Sediment and fluid enrichment do not correspond. IAT-Island Arc Tholeiite, GLOSS- Global Subducting Sediment, references in Figure 35.

Table 17 Representative Melt Inclusion Compositions

	1	2	3	4	5	6	7	8	9	10	11	12	13	14	15
SiO_2 %	50.99	48.39	48.96	46.20	47.71	48.52	46.44	45.46	47.28	48.54	49.63	48.53	45.81	45.31	47.47
TiO_2	0.58	0.73	0.62	0.45	0.42	0.42	0.30	0.43	0.42	0.46	0.61	0.57	0.52	0.49	0.40
Al_2O_3	12.71	11.34	10.71	9.29	8.73	8.87	8.44	7.94	9.44	8.97	12.78	11.34	12.07	11.41	8.93
Cr_2O_3	0.04	0.04	0.07	0.06	0.05	0.05	0.06	0.03	0.02	0.54	0.02	0.01	0.02	0.05	0.07
FeO*	10.73	9.58	10.00	10.24	10.76	9.68	9.93	10.47	10.58	8.25	9.47	8.99	9.52	9.44	10.13
MgO	14.70	17.56	18.33	20.69	18.34	18.20	22.35	24.16	20.25	16.89	13.65	19.63	18.22	20.16	20.54
MnO	0.22	0.14	0.14	0.16	0.18	0.13	0.18	0.20	0.19	0.13	0.14	0.14	0.14	0.14	0.16
K_2O	0.71	0.64	0.44	0.59	0.41	0.43	0.44	0.49	0.52	0.48	0.68	0.51	0.56	0.45	0.53
Na_2O	2.53	1.99	1.72	1.08	0.99	0.99	1.12	1.05	1.76	1.24	1.72	1.31	1.43	1.35	1.21
CaO	6.84	8.78	9.52	10.62	12.81	13.00	10.63	9.97	9.15	14.04	12.17	9.63	11.12	9.48	10.53
P_2O_5	0.17	0.19	0.16	0.11	0.12	0.10	0.15	0.12	0.12	0.09	0.09	0.06	0.05	0.04	0.13
S (ppm)	61	1382	105	2022	1419	1412	11	209	12	2426	136	88	1115	102	801
Cl (ppm)	99	182	103	1346	225	262	7	15	20	318	152	295	422	235	222
H_2O %	-	-	-	-	-	-	-	-	-	-	0.64	0.34	0.47	0.12	0.39
Total	100.22	99.38	100.67	99.49	100.52	100.39	100.04	100.32	99.73	99.63	100.97	100.71	99.46	98.31	100.10
Mg#	70.95	76.6	76.7	78.3	75.2	77.0	80.1	80.4	77.3	78.5	66.65	78.42	74.50	79.13	79.06
CaO/Al_2O	0.54	0.77	0.89	1.14	1.47	1.47	1.26	1.26	0.97	1.57	0.95	0.85	0.92	0.83	1.18
Cl/K	0.01	0.03	0.02	0.23	0.05	0.06	0.00	0.00	0.00	0.07	0.02	0.06	0.08	0.05	0.04

Table 17 Continued

	1	2	3	4	5	6	7	8	9	10	11	12	13	14	15
an	23.71	3.86	19.84	24.41	23.85	24.63	16.84	32.63	17.05	25.24	36.12	31.58	30.95	32.58	26.04
ab	2.06	0.34	1.72	2.12	2.07	2.14	1.46	2.84	1.48	2.20	3.14	2.75	2.69	2.83	1.37
or	2.30	4.20	2.72	2.90	2.01	2.54	2.60	2.30	3.07	2.78	3.96	3.01	3.01	2.72	3.13
ne	0.00	0.00	5.10	0.00	0.00	0.00	4.25	0.17	6.80	0.00	0.00	0.00	1.99	0.16	0.00
di	22.55	9.61	25.97	28.40	23.72	28.21	23.95	25.48	22.56	40.36	27.58	18.87	23.96	18.67	26.98
hy	21.49	21.70	0.00	14.58	2.52	22.98	0.00	0.00	0.00	4.49	5.90	12.08	0.00	0.00	4.69
wo	0.00	0.00	0.00	0.00	0.00	0.00	0.00	0.00	0.00	0.00	0.00	0.00	0.00	0.00	0.00
fo	25.18	18.73	41.18	23.63	42.77	15.67	46.88	33.34	44.61	20.58	20.21	28.82	34.49	40.18	34.69
il	0.44	1.10	0.87	0.74	0.70	0.70	0.57	0.76	0.80	0.85	1.14	1.08	0.99	0.95	0.76
mt	1.68	1.91	2.19	2.48	2.06	2.49	3.06	1.84	3.33	2.35	1.68	1.59	1.71	1.73	1.81
ap	0.23	0.23	0.37	0.28	0.28	0.23	0.35	0.25	0.28	0.21	0.21	0.14	0.12	0.09	0.30
cm	0.09	0.09	0.07	0.06	0.04	0.10	0.13	0.12	0.04	1.16	0.06	0.06	0.06	0.06	0.09
pr	0.30	0.02	0.00	0.36	0.02	0.30	0.00	0.28	0.00	0.51	0.02	0.06	0.06	0.06	0.17
Halite	0.04	0.02	0.02	0.06	0.00	0.06	0.00	0.04	0.00	0.04	0.00	0.00	0.00	0.00	0.04

Table 18 Melt Inclusion Trace Element Concentrations

	1	2	3	4	5	6	7	8	9
Rb (ppm)	9.41	7.34	5.83	8.40	9.91	10.68	4.76	4.44	7.42
Sr	263.88	249.64	337.89	402.90	353.63	359.42	262.94	209.95	309.83
Y	27.03	17.42	17.12	12.05	8.60	8.40	9.89	6.18	10.80
Zr	92.08	52.77	51.01	26.07	19.99	20.73	28.98	16.62	28.46
Nb	3.02	1.31	1.25	0.90	0.70	0.68	0.76	0.56	0.95
Ba	172.82	62.43	83.80	87.24	83.63	82.53	67.90	62.51	92.77
La	8.95	3.76	5.22	4.16	3.46	3.74	4.12	2.99	5.08
Ce	19.68	10.54	11.38	9.35	8.65	9.11	8.66	6.61	9.98
Pr	2.82	1.66	2.00	1.44	1.12	1.22	1.27	0.79	1.45
Nd	13.92	6.72	9.14	7.30	5.69	5.81	5.80	4.31	6.71
Sm	3.56	3.07	3.02	2.00	1.42	1.40	1.02	1.17	2.14
Eu	0.57	0.70	0.88	0.70	0.49	0.56	0.25	0.37	0.54
Gd	3.93	2.40	2.98	2.08	1.61	1.34	*BDL*	*BDL*	1.80
Dy	3.99	3.20	3.13	1.79	1.36	1.37	1.61	1.15	1.47
Er	2.63	1.52	1.93	1.23	0.88	0.82	1.16	0.56	0.84
Yb	2.95	2.07	1.54	1.24	0.82	0.78	1.23	0.67	1.06
Hf	1.99	1.09	1.49	0.91	0.42	0.63	0.69	*BDL*	0.70
Ta	*BDL*	0.02	0.08	0.06	*BDL*	*BDL*	*BDL*	*BDL*	*BDL*
Pb	3.64	0.38	0.71	1.49	1.22	1.39	0.32	*BDL*	*BDL*
Th	1.16	0.41	0.46	0.32	0.42	0.44	*BDL*	0.34	0.47
U	0.42	0.23	0.77	0.13	0.18	0.19	*BDL*	*BDL*	0.30

Samples correspond to those in Table 17

Temperature Estimates

We estimated magmatic temperatures using olivine-spinel geothermometers (Fabries, 1979; Roeder et al., 1979; Ballhaus et al., 1991) the olivine-liquid thermometer of Roeder and Emslie (1970), and from MI MgO concentrations using the empirical relation T≈18*MgO+1050 described by Eggins (1993). These calculations are limited to the picrite, as the ankaramite lacked any spinel except in the groundmass. We made several estimates for each mineral pair using pressures of 10, 20 and 30 kbar to account for pressure dependence in the thermometers, but this resulted in only 30-40° higher calculated temperatures at 30 kbar compared to 10 kbar. For olivine-spinel pairs in the large crystal clot ($Fo_{91.8}$ olivine and Cr#60 spinel), temperature estimates were 1375-1478.3° C; other estimates calculated using compositions of olivine phenocrysts and included spinel ranged from 1199.65 to 1449.47° (Table 19). Temperatures determined using the MgO contents of the MI and the Eggins calculation were 1278.55-1504.6°, while the Roeder and Emslie olivine-liquid thermometers calculated temperatures up to1452° C. One $Fo_{91.6}$ olivine had a melt-spinel inclusion and this allowed a comparison of temperature estimates via both methods (Olivine 8-Table 14). The Roeder thermometer gave a temperature of 1359.40° and the Ballhaus 1354.21° at 15 kbar. In comparison, the estimation of temperature using the MgO content of the MI was 1353.99°, and this demonstrates that liquidus temperature estimates using the olivine-spinel thermometers and the liquid MgO approximation were in agreement, at least for this example. The effects of water in the melt on liquidus temperature must also be considered, as it has been estimated that each percent H_2O dissolved in a melt will depress the liquidus ~50° C (Foden and Green, 1992). However, due to the low water contents of the melts (0.16 to 0.62 wt% water) the temperatures estimates would need to be adjusted downward only 6-32°.

Due to the phenocryst assemblages in the lava, there was not a robust geobarometer we could utitilize. The Ol/CPX Ca exchange geobarometer of Köhler and Brey (1990) could be used with the available mineral pairs, but the strong temperature dependence of this barometer is a major drawback. The pressure dependence of the olivine-spinel geothermometers we used is a further complication. The OPX-CPX

thermometer has a minimal pressure dependence (Köhler and Brey, 1990), but this option simply was not available to us due to the lack of OPX in the lavas. There is a further difficulty in matching olivine-CPX pairs. EMP data from CPX inclusions in olivine was of poor quality, and the possibility of two melts with different crystallizing phenocryst assemblages, as suggested by the normative data (Figure 33), casts doubt on the ability to correctly match co-crystallizing olivine and CPX.

Table 19. Estimated Magmatic Temperatures From Phenocrysts

	1	2	3	4
Ol-Sp Geothermometry				
Ol Mg#	91.8	91.04	91.5	89.7
Sp Cr#	0.56	0.63	0.84	0.77
Fabries	1375	1449	1272	1200
Roeder	1478	1430	1359	1180
Ballhaus	1454	1367	1354	1241

Temperatures in ° C

Fabries-Ol-Sp Thermometer in Fabries (1979)
Roeder-Ol-Sp Thermometer in Roeder et al. (1979)
Ballhaus-Ol-Sp Thermometer in Ballhaus et al. (1979)

Degree of melting

The co-variation of elements with differing degrees of compatibility can show both the degree of melting (F) and the amount of depletion of the melt source. We used a Nb-Yb variation diagram due to its ability to show distinctly the differences between F and source depletion(Pearce and Parkinson, 1993). The latter results from the large Nb depletions in sources that have been depleted by even small degrees of melting. We produced several melting curves using primitive mantle (McDonough and Sun, 1995) and 1, 2 and 5% depleted primitive mantle compositions and compared these to the MI data. Simple non-modal batch melting models had the best fit to the MI compositions, which plotted between melting curves for primitive mantle (McDonough and Sun, 1995) and 2% depleted primitive mantle on the Nb-Yb diagram. Based on these models, F derived from melt inclusion compositions ranged from 5% to 60% (Figure 38a). The MI data do not show significant scatter and plot along what may be interpreted as a single melting curve or several closely spaced curves. To test whether the MI compositions reflect melting of a single or multiple mantle sources, we modeled curves for a variety of mantle types. We found that the some MI data best fit melting curves for primitive mantle

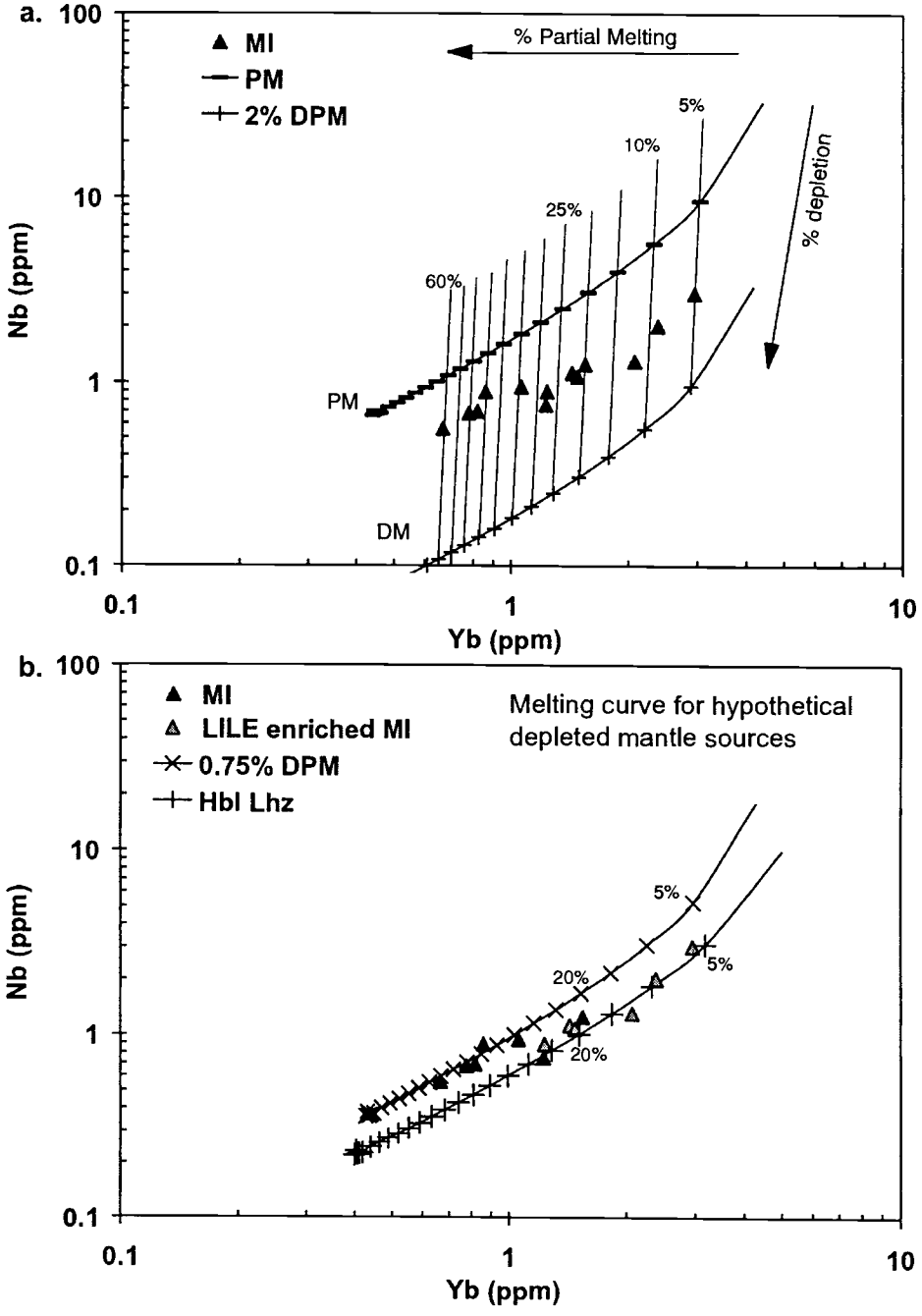

Figure 38: Batch melting models compared to MI data on Nb-Yb variation diagram. a. MI data plot between melting curve for primitive mantle (MacDonough and Sun, 1995) and mantle depleted by 2% melting. MI data indicate up to 60% partial melting (F). b. MI data compared to melting models for primitive mantle depleted by 0.75 % melting and depleted hornblende lherzolite. MI with higher LILE, U, Ba and Cl plot along hornblende lherzolite curve, while magnesian, nepheline normative MI plot along primitive mantle curve and have the highest F. Data suggest LILE enriched MI represent ~6-25% partial melts of metasomatized mantle, while other MI trap high degree melts of primitive mantle.

depleted 0.75%. Other MI data fit a melting curve for a hypothetical depleted amphibole bearing mantle. The Nb and Yb concentrations for amphibole bearing mantle were taken from those given for hornblende lherzolite in Pearce and Parkinson (1993). The bulk distribution coefficients of D_{Nb} of 0.022 and D_{Yb} of 0.08 were determined to produce a hornblende lherzolite melting curve with the best fit to the MI data. This corresponded to a modal assemblage of 61% Ol, 28% OPX, 7% CPX, 2% hornblende and 2% spinel, using mineral melt partition coefficients in the literature (Shimizu, 1982; Fuijimaki, and Tatsumoto, 1984; Kennedy et al., 1993; Beattie, 1994; Forsythe et al., 1994; Schwandt, and McKay, 1998). Melt inclusions with the highest levels of LILE, U/Th and Na plotted along the hornblende lherzolite curve (Figure 38b). Degrees of partial melting for these MI based on this curve were ~6–25%. The rest of the MI data fell along the depleted primitive mantle curve and had estimated Fs of 35-60%. These included the magnesian, nepheline normative and depleted MI. The highest degrees of melting may represent locally high degrees of melt and would not be unexpected if the temperatures estimated are valid.

DISCUSSION

The magma-genesis of high-MgO basaltic arc lavas has been related to early arc magmatism and proximity to a triple junction (Hawkins, 2003), arc-ridge collision (Baker and Condliffe, 1996; Monzier et al. 1997), subduction of young crust (Schuth, 2003), decompression melting during induced counterflow separate from a vertically rising diapir (Nye and Reid, 1986). These circumstances and mechanisms largely do not apply to the genesis of the Chaife seamount lavas. The crust being subducted in the Mariana subduction zone is among the oldest known (Hirschmann 2000; Stern et al., 2003) and there is no collision between an arc and ridge. The maximum age of Mariana arc lava is constrained by the initiation of seafloor spreading in the Mariana Trough 3-4 Ma. (Yamakazi and Stern, 1997), which would have displaced the original arc and led to the creation of a new one. With an age of 2.49 Ma., the picrite lava may have origins related to the creation of this new arc, and thus may be similar to the early-arc high-MgO tholeiites of Tonga (Hawkins, 2003). The MI data show that the Chaife picrite magmas were water-poor, and this suggests the presence of anhydrous decompression melt.

Pressure-release melting could be generated by induced counter flow in the mantle wedge, as described by Nye and Reid (1986). However, in this process the decompression melt would be produced separately from the melt generated near the slab-wedge interface. In order for the melt inclusions to have arc-like compositions, the counter-flow decompression melt would have to be transported to a point where it could mix with a typical arc melt prior to eruption. We contend that this process is unnecessarily complicated and our data can be explained by a simpler model.

In this model, the picrite originated from processes that have been suggested for the generation of typical island arc tholeiites (Figure 39). In currently accepted models of subduction zone magma-genesis (summarized in Tatsumi and Eggins, 1995 and Stern, 2002), the fore-arc and descending limb of convecting asthenosphere in the mantle wedge are hydrated by fluid released from the crust and sediments in the subducting slab (A-Figure 39). This hydration may lead to the generation of phases such as amphibole in the mantle wedge peridotite, and these minerals would then transport fluid deeper into the subduction zone above the slab. The location of the magmatic front in arcs has been shown by seismic data to lie at least ~100 km (3 GPa) above the slab-wedge interface (Gill, 1981; Tatsumi and Eggins 1995) and this coincides with the pressure stability limit for pargasitic amphibole in the mantle. Pressure related breakdown of amphibole would flux the surrounding mantle and promote primary melting where the geotherm intersected the solidus for hydrated mantle (B-Figure 39). The typical arc lava trace element pattern of LILE enrichment and HFSE depletion is thought to result in part from metasomatism of the mantle prior to melting (summarized in Davidson, 1996; Stern, 2002). The MI with higher LILE, U, Ba, Cl and alkali contents could conceivably result from 5-25% melting of metasomatised, depleted mantle (Figure 38). As stated earlier, Th is sediment derived but is not soluble in aqueous fluids (Elliot et al., 1997) and the elevated Th/Yb and Th/Nb levels in the melt inclusions (Figure 36 and 37) may indicate the mixing of sediment melt (C Figure 39). It has been proposed that sediments in subduction zone commonly melts (Johnson and Plank, 1999) and with the high temperatures our data indicates for the mantle beneath the Chaife seamount this may be a reasonable assumption.

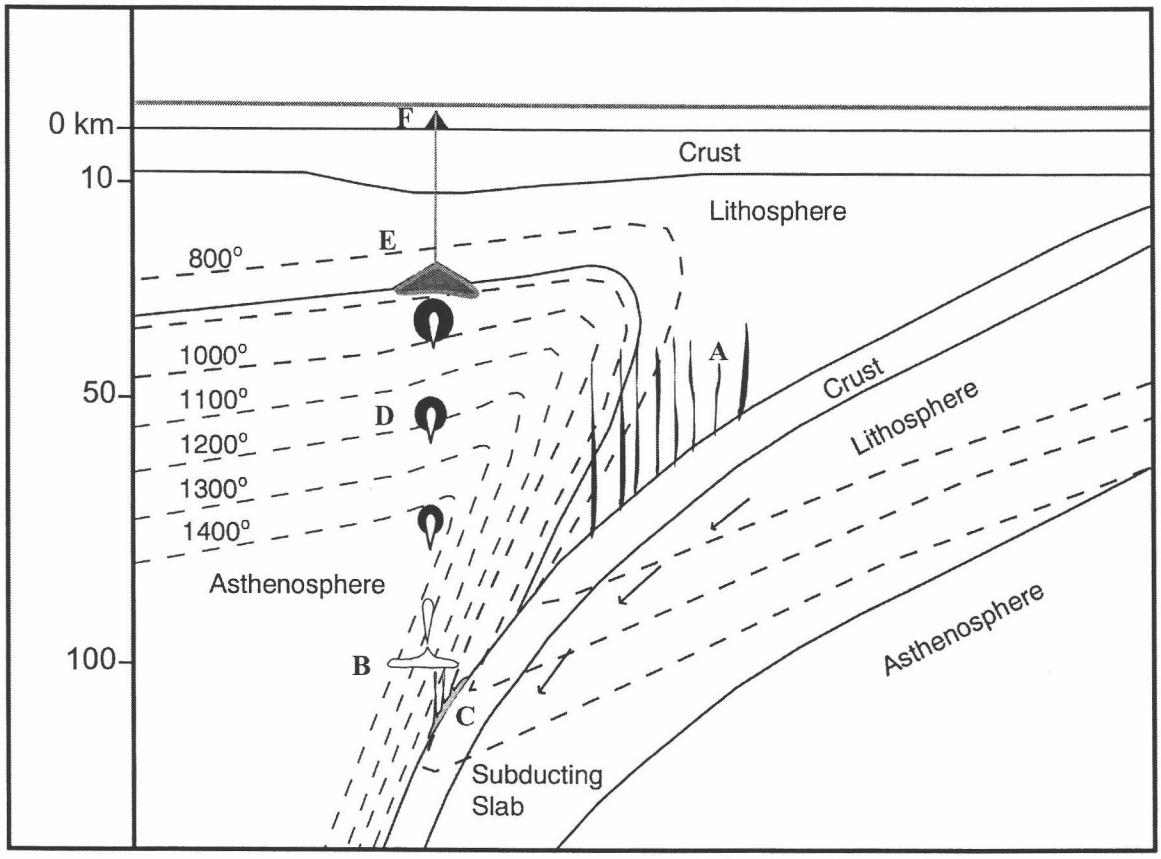

Figure 39: Model for the magma-genesis of the Chaife picrite. The steep dip of the slab in the model and the crustal thickness are based on Figures 11 and 13 in Stern et al. (2003). Geotherms are speculative, but are based on temperature data from geothermometry (see text). A-dehydration of subducting slab hydrates forearc and descending limb of mantle wedge. Fluid may also be added at greater depths B-breakdown of hydrous phases in fluxes melt and produces initial arc melt at ~100 km depth. High LILE MI may represent this melt. C-Sediment melting may occur, mixing with primary arc melts and elevating Th levels. C-Melts collects and rise in a partially molten peridotitic diapir. Ascent of this hot diapir perturbs geotherm and induces decompression melting, which mixes with melt within diapir. E-diapir ascent arrested at base of lithosphere and crystal accumulation takes place. F. Magma from location at E ascends to the surface without undergoing substantial low-pressure segregation or assimilation and erupts as picrite. A similar melt with possibly less subduction signal and CPX fractionation and accumulation erupts several hundred ka. later as ankaramite.

Several workers have argued that melt is transported from the point of initial partial melting through the lateral and downward flowing asthenosphere when a sufficiently large volume of melt accumulates and rises in a buoyant diapir due to Rayleigh-Taylor instabilities (e.g. Scott and Stevenson, 1986; Hall and Kincaid, 2001; Stern, 2002). We have no constraints on ascent rates for our melts, but Hawkesworth et al. (1997) have estimated (based on U-series disequilibrium measurements) that melt ascent rates may be

as high as ~1-4 m/yr. The rising melt diapir would locally perturb the regional geotherm and generate melting of the surrounding mantle when the T-P conditions intersected the dry peridotite solidus (D-Figure 39). There is a growing body of evidence for the presence of water-poor, decompression melting in subduction zones (e.g., Nye and Reid, 1986; Bacon et al., 1997; Sisson and Bronto, 1998), and such secondary melting may not be uncommon. A larger diaper will contain much more heat and ascend more quickly than smaller ones (Hall and Kincaid, 2001) and consequently larger volumes of initial melt would induce greater secondary melting. Substantial decompression melting would dilute the trace element and volatile signals of the hydrous magma while buffering MgO contents at high levels. We suggest the highly magnesian, nepheline normative, depleted MI compositions are samples of this secondary decompression melting. Continual mixing of the decompression melt into the larger melt body as it ascended could produce the low trace element concentrations we observed in the melt inclusions, while maintaining the typical arc pattern (Figure 35). Experimental data of Schwab and Johnston (2001) indicate that Mg#s increase and alkalis and Al decrease with increasing melt fraction and this also corresponds with what is observed in the MI. Temperatures similar to the higher values we obtained from our thermometers (≥1450°) can at 1 GPa lead to Mg#s of ~80 (Falloon et al., 2001) and degrees of melting exceeding 50% (Jacques and Green, 1980) and this also correlates with our data.

As the diapir rises, the amount of melting would reach a maximum and the incompatible trace element concentrations a minimum when the upward movement is arrested at or near the base of the lithosphere at (D Figure 39). During this period of stagnation continual crystallization would lead to an accumulation of phenocrysts. A large diapir that rose adibatically would maintain high temperatures in its interior with slow cooling and near-isothermal crystallization. The polyhedral morphology and of the phenocrysts and the scarcity of melt inclusions does suggest that a large amount of crystallization occurred with slow cooling, possibly near isothermal (Donaldson, 1976; Faure et al., 2003; Kohut and Nielsen in press).

It is the contention of Furukawa (1993) that melt transport occurs in vertical magma filled cracks, ~100 km. in height, that result from differential stress fields in the mantle wedge and it may be argued that the picrite parent magmas were transported to

the surface by this process rather than in a rising diapir. However, propagation through a network of fracture pathways would likely result in reaction with the surrounding mantle and rapid cooling along the lengths of the channels walls. The latter would result in more incomplete phenocryst morphologies, such as hopper textures and a greater abundance of melt inclusions, features that we did not observe in these lavas.

For most arc volcanoes, the parental melts would segregate and propagate through the lithosphere after diapiric ascent stops at the moho. The melt separated from the crystal rich magma would then undergo further modification from assimilation, fractionation and mixing at shallow levels (<10 kbar) that result in the typical evolved and diverse arc magmas. However, it appears that at the Chaife seamount the very primitive, crystal-rich magma erupted onto the surface relatively unmodified. The reasons why typical low pressure segregation and modification did not occur are unclear at the present time and require further study of the area. One possibility is that the lithosphere may be thinner in this region of the Mariana arc due to extension. Another is that there is a leaky transform that allows eruption of deep magmas and might also enhance upwelling. This possibility is supported by the presence of the cross-arc seamount chains in the vicinity, which indicate that magmatism was not confined to a single locale on the arc front. Tamura et al. (2002) have suggested that advection of hotter asthenosphere into the wedge, perpendicular to the magmatic front, controls the spacing of arc volcanoes. An enhanced version of such a feature could produce strong upwelling, lithospheric thinning and allow primitive magmas erupt. Nye and Reid (1986) postulate that the Okmok high-MgO lavas reached the surface more readily due to the location of the volcano on a segment boundary. The locations of the cross-chains near the Chaife seamount and other locations in the southern Mariana arc may be evidence for segment boundary magmatism. However, we presently lack the geophysical or structural data necessary to determine any mechanism or structure in the Mariana arc that would facilitate the transport of high-MgO magmas through the lithosphere.

The eruption of the compositionally similar ankaramite several hundred thousand years after the picrite indicates that production of high-MgO lavas was not a singular event. The ankaramite might have developed from fractionation of a komatiitic magma with CaO/Al_2O_3 numbers >1, similar to those sampled by MI from the picrite (Della-

Pasqua and Varne, 1997). The greater normative Di content, Ni, lower Ce, and slightly different Pb isotopic characteristics and the age difference indicates that it arose from a separate melt in a similar source region. Furthermore, it suggests that there may be more primitive lavas yet to be sampled from Chaife and other seamounts in its vicinity.

CONCLUSIONS

The lavas from the Chaife seamount have characteristics consistent with presumed primary magma compositions, i.e. Mg#s>70, Ni>200 ppm and Cr>400 ppm (Kinzler et al., 1990; Tatsumi and Eggins, 1995). The trace element patterns and isotopic compositions indicate that they are arc-like melts that originated in an Indian mantle domain typical of Mariana arc lavas. Melt inclusions in olivine phenocrysts in the picrite provide direct sampling of melts isolated from the low-pressure re-equilibration, mixing and fractionation that may obscure parental component signals.

Major element, trace element and volatile measurements reveal that the melt inclusions from the picrite represent samples of two primitive magmas. Evidence for the first magma type was provided by a small number of inclusions. These had MgO contents of ~14.6- 20% MgO and LILE, U, and Na within the range of typical island arc tholeiites, and Cl up to 1346 ppm. We propose that these melts derived from initial partial melting (~5-30%) of metasomatised mantle near the slab-wedge interface. Most MI had Th/Yb and Th/Nb values above the mantle levels and we interpret these data as being possible evidence for a sediment melt component, separate from the LILE and U enrichment, that mixed into the parent magmas. We propose that the initial melts rose adiabatically in a diapir through the convecting mantle wedge and induced secondary decompression melting in the surrounding asthenosphere. Evidence for such melts are provided by nepheline normative, high MgO melt inclusions with subdued arc-like trace element patterns and Th/Yb and Pb/Ce levels. Mixing of the secondary decompression melt with the primary melt buffered the MgO contents at high levels and diluted the subduction signal and volatiles. Following a period of stagnation and crystal accumulation, the magma erupted relatively unaffected by low-pressure modification in comparison to most arc lavas. Although it is uncertain how representative these melt inclusion compositions are to arc parent magmas in general, the MI compositions regressed to 8% MgO are similar to the more primitive examples of island-arc tholeiites.

The high-Fo olivines and magnesian MI compositions, coupled with the high degrees of melting and temperature estimates of >1450°C indicate that, at least for the southern Mariana arc, temperatures are greater than predicted by existing geothermal models of subduction zones.

SUMMARY OF CONCLUSIONS

The objectives for the first part of this thesis were to determine experimentally the compositions of anhydrous mafic-silicate melts in equilibrium with high-An feldspar, and develop a possible model for the petrogenesis of anorthite bearing MORB lavas. The results of the phase-equilbria experiments indicate that it is possible to experimentally produce anorthite and Fo_{90} saturated basaltic liquids close in composition to naturally occurring lavas. These experimental liquids are also saturated with Al-rich spinel that is similar in composition to spinels observed in naturally occurring anorthite megacrysts (Fisk et al., 1982; Allan et al., 1989; Dick, 1989; Sinton et al., 1993). This association suggests the possibility that primitive MORB basalts are high-An plagioclase saturated due to continued reaction with the upper mantle above the melting regime. Such a reaction of the rising basaltic magma with the spinel in the depleted upper mantle at depths less than 10 kb would drive the magma toward saturation with feldspar. In essence, high-An feldspar in MORB may be produced by a buffering reaction at the Sp + liquid $\rightarrow$Fo + An reaction point. Our experiments also indicate that this buffering reaction will result in an average of ~16–26 % crystallization for each percent decrease in MgO. These data suggest primitive MORB lavas (>8% MgO) have undergone ~62–77% fractionation and reaction with the uppermost mantle and lower crust before eruption. The implication of these results is that any interpretation of compositional data from melt inclusions in MORB high-An feldspar must take into consideration the possibility that the entrapped liquids may not represent primary magmas.

The next experimental objectives were to determine the melt inclusion formation mechanisms in olivine and plagioclase in anhydrous mafic-silicate liquids and whether the entrapment process could produce the diversity observed in natural inclusions. The results of the inclusion formation experiments showed that melt inclusions in high-An plagioclase and high-Fo olivine in low pressure, anhydrous mafic melts could arise from changes in growth mechanisms and crystal morphology during undercooling and subsequent isothermal crystallization. As a consequence of this change in dominant growth mechanisms, the planar growth that developed during the isothermal periods sealed the embayments of hopper and skeletal crystals formed during cooling and entrapped the melt. Since this was the dominant inclusion formation mechanism, most of the experimentally produced inclusions formed during isothermal crystallization

following cooling. The experiments with 6-hour and greater isothermal periods exhibited the highest frequencies of inclusions, and these times appear to have been long enough to preclude trapping a boundary layer or diffusive profile. For this reason, all experimentally produced inclusions in olivine and plagioclase had compositions identical to the surrounding glass, except in the case of the few inclusions formed during cooling. Thus, entrapment by this mechanism will not lead to compositional diversity in the inclusions. Circumstances in nature similar to our experimental conditions may occur when a partial melt rises through a conduit into cooler crust and stagnates at low pressure (<10 kb) prior to eruption and quenching.

The final objectives of this thesis research were to utilize melt inclusions analysis techniques to directly sample the parental melt(s) for a very primitive arc picrite, determine the mantle and subduction components of the parent magmas, and provide a possible model for the picrite magma-genesis. Major element, trace element and volatile measurements revealed that the melt inclusions from the picrite represented samples of two primitive magmas. Evidence for the first magma type was provided by a small number of inclusions. These had MgO contents of ~14.6- 20% MgO and LILE, U, and Na within the range of typical island arc tholeiites, and Cl up to 1346 ppm. We suggest that these melts derived from initial partial melting (~5-30%) of metasomatised mantle near the slab-wedge interface. Most MI had Th/Yb and Th/Nb values above the mantle levels and we interpret these data as being a possible contribution from a sediment melt component (separate from the LILE and U enrichment) that mixed into the parent magmas. We propose that the initial melts rose adiabatically in a diapir through the convecting mantle wedge and induced secondary decompression melting in the surrounding asthenosphere. Evidence for such melts were provided by nepheline normative, high MgO melt inclusions with subdued arc-like trace element patterns and lower Th/Yb and Pb/Ce levels. Mixing of the secondary decompression melt with the primary melt buffered the MgO contents at high levels and diluted the subduction signal and volatiles. The polyhedral morphology of the phenocrysts and the relative lack of melt inclusions, together with the high phenocryst content of the picrite lava indicate slow cooling and crystal accumulation at depth. Although it is uncertain how representative these melt inclusion compositions are to arc parent magmas in general, the

MI compositions regressed to 8% MgO are similar to the more primitive examples of island-arc tholeiites. The high-Fo olivines and magnesian MI compositions, coupled with the high degrees of melting and temperature estimates of >1450°C indicate that, at least for the southern Mariana arc, temperatures are greater than predicted by existing geothermal models of subduction zones.

BIBLIOGRAPHY

Allan, J. F., R. Batiza, M. R. Perfit, D. J. Fornari, and R. O. Sack, Petrology of lavas from the Lamont seamount chain and adjacent East Pacific Rise, 10°N, J. Petrol., 30, 1245–1298, 1989.

Anderson, A. T., Evidence for a picritic volatile-rich magma beneath Mt. Shasta, California, J. Petrol. 15: 243-267, 1974.

Anderson, A. T. and Wright, T. L. Phenocrysts and glass inclusions and their bearing on oxidation and mixing of basaltic magmas, Kilauea volcano, Hawaii, Am. Mineral. 57: 188-216, 1972.

Bacon, C.R., Bruggman, P.E., Christiansen, R.L., Clynne, M.A., Donnelly-Nolan, J.M., Hildreth, W. Primitive magmas at five Cascade volcanic fields: melts from hot, heterogeneous sub-arc mantle, Can Mineral. 35: 397-423, 1997.

Baldan, A. Progress in Ostwald ripening theories and their applications to nickel base superalloys J. Mater. Sci. 37:2171-2202, 2002.

Baker, M. B., T. L. Grove, R. J. Kinzler, J. M. Donnelly-Nolan, and G. A. Wandless, Origin of compositional zonation (high alumina basaltic andesite) in the Giant Crater Lava Field, Medicine Lake Volcano, northern California, J. Geophys. Res., 96, 21,819–21,842, 1991.

Baker, P.E. and Condliffe, E. Compositional variation in submarine volcanic ashes from the vicinity of the Vanuatu Island Ac: a response to ridge-arc collision? J. Volc. Geophys. Res., 72: 225-238, 1996.

Ballhaus, C.G., Berry, R.F., Green, D.H., High pressure calibration of the olivine-orthopyroxene-spinel oxygen barometer, implications for the oxidation sate of the upper mantle, Contrib. Mineral. Petrol. 107: 27-40, 1991.

Bartles, K.S.; Kinzler, R.J.; Grove, T.L., High-pressure phase relations of primitive high-alumina basalts from Medicine Lake volcano, northern California, Contrib. Mineral. Petrol. 108: 253-270, 1994.

Basaltic Volcanism Study Project (BVSP), Ocean-floor basaltic volcanism, in Basaltic Volcanism on the Terrestrial Planets, pp. 132–160, Pergamon, New York, 1981.

Beattie, P., Systematics and energetics of trace-element partitioning between olivine and silicate melts: Implications for the nature of mineral/melt partitioning Chem. Geol. 117: 57-71, 1994.

Bloomer, S.H., Hawkins, J.W., Petrology and geochemistry of boninite series volcanic rocks from the Mariana trench: Contributions to Mineralogy and Petrology, v. 97, p.361-377, 1987.

Bloomer, S.H., Stern, R.J., and Smoot, N.C., 1989. Physical volcanology of the submarine Mariana and volcano arcs: Bulletin of Volcanology, v. 51, p.210-224.

Bodnar, R J and Sterner, S M (1984) Synthesis of fluid inclusions in natural quartz, Eos Trans., 78:

Cashman, K. V. Crystallization of Mount St. Helens 1980-1986 dacite: a quantitative textural approach, Bull. Volcanol. 50: 194-209, 1988.

Cashman, K. V. Relationship between plagioclase crystallization and cooling rate in basaltic melts, Contrib. Mineral. Petrol. 113: 126-142, 1993.

Cashman, K. V. and Ferry, J. M., Crystal size distribution (CSD) in rocks and the kinetics and dynamics of crystallization III. Metamorphic crystallization, Contrib. Mineral. Petrol. 99: 401-415, 1988.

Cashman, K.V. and Marsh, B. D. Crystal-size spectra and kinetics of crystal growth in magmas II. Application. Geol. Soc. Am. Abstr. Programs, 16: 465, 1984.

Cervantes, P., and P. Wallace, Water in subduction zone magmatism: New insight from melt inclusions in high-Mg basalts from central Mexico, Eos Trans. AGU, 81(48), Fall Meet. Suppl., abstract V21G-03, 2000.

Cherkaoui, A. S. M., Wilcock, W. S. D., Dunn, R. A., Toomey, D. R., A numerical model of hydrothermal cooling and crustal accretion at a fast spreading mid-ocean ridge Geochem. Geophys. Geosys. 4: doi:10.1029/2001GC000215, 2003.

Corrigan, G. M. The crystal morphology of plagioclase feldspar produced during isothermal supercooling and constant rate cooling experiments, Miner. Mag. 46: 433-439, 1982

Cooper, K. M., Reid, M. R., Murell, M. T., Clague, D. A. Crystal and magma residence at Kilauea Volcano, Hawaii: 230^{Th}-226^{Ra} dating of the 1955 east rift eruption, Earth Planet. Sci. Lett. 184: 703-718, 2001.

Danyushevsky, L.V., Falloon, T.J., Sobolev, A.V., Crawford, A.J., Carroll, M., Price, R.C., The H_2O content of basalt glasses from southwest Pacific back-arc basins. Earth Planet. Sci. Lett., 117: 347-362, 1993.

Danyushevsky, L. V., McNeill, A. W., and Sobolev, A.V., Experimental and petrological studies of melt inclusions in phenocrysts from mantle-derived magmas: an overview of techniques, advantages and complications, Chem. Geol. 183: 5-24, 2002.

Danyushevsky, L. V., M. R. Carroll, and T. J. Falloon, Origin of high-An plagioclase in Tongan high-ca boninites: Implications for plagioclase-melt equilibria at low (PH_2O), Can. Mineral., 35, 313–326, 1997.

Davidson, J. P., Deciphering mantle and crustal signatures in subduction zone magmatism (overview), *in* Bebout, G.E., Scholl, D.W., Kirby, S.H., Platt, J.P. eds. Subduction top to bottom, American Geophysical Union, Washington: 251-262, 1996.

Davis, A. S., and D. A. Clague, Geochemistry, mineralogy, and petrogenesis of basalt from the Gorda Ridge, J. Geophys. Res., 92, 10,467–10,483, 1987.

Della-Pasqua, F.N. and Varne, R., Primitive ankaramitic magmas in volcanic arcs: a melt inclusion approach, *Can Mineral.* 35: 291-312, 1997.

Dick, H. J. B., Abyssal peridotites, very slow spreading ridges and ocean ridge magmatism, in Magmatism in the Ocean Basins, edited by A. D. Saunders and M. J. Norry, Geol. Soc. Spec. Publ., 42, 71–106, 1989.

Dick, H. J. B., and T. Bullen, Chromian spinel as a petrogenetic indicator in abyssal and alpine-type peridotites and spatially associated lavas, Contrib. Mineral. Petrol., 86, 54–76, 1984.

Dick, H. J. B., and R. L. Fisher, Mineralogic studies of the residues of mantle melting: Abyssal and alpine type peridotites, in Kimberlites II: The Mantle and Crust-Mantle Relationships, edited by J. Kornprobst, pp. 295–308, Elsevier Sci., New York, 1983.

Dick, H. J. B., and J. H. Natland, Late-stage melt evolution and transport in the shallow mantle beneath the East Pacific Rise, Proc. Ocean Drill. Program Sci. Results, 147, 103–134, 1996.

Dixon, T.H., Stern, R.J., 1983. Petrology, chemistry, and isotopic composition of submarine volcanoes in the southern Mariana arc: Geological Society of America Bulletin, v. 94, p.1159-1172.

Donaldson, C. H. , Calculated diffusion coefficients and the growth rate of olivine in a basalt magma, Lithos 8: 163-174, 1975.

Donaldson, C. H., An experimental investigation of olivine morphology, Contrib. Mineral. Petrol. 57: 187-213, 1976.

Donnelly-Nolan, J. M., D. E. Champion, T. L. Grove, M. B. Baker, J. E. Taggert, and P. E. Bruggman, The Giant Crater Lava Field, Geology and geochemistry of a compositionally zoned, high alumina basalt to basaltic andesite eruption at Medicine Lake Volcano, J. Geophys. Res., 96, 21,843–21,863, 1991.

Draper, D.S. and Johnston, A.D., Anhydrous PT relations of an Aleutian high-MgO basalt: an investigation of the role of olivine-liquid reaction in the generation of high-alumina basalts, Contrib. Mineral. Petrol., 34: 501-519, 1992.

Dungan, M. A., and J. M. Rhodes, Residual glasses and melt inclusions in basalts form DSDP Legs 45 and 46: Evidence for magma mixing, Contrib. Mineral. Petrol., 67, 417–431, 1978.

Eggins, S.M. Origins and differentiation of picritic arc magmas, Ambae (Aoba), Vanuatu, Contrib. Mineral. Petrol. 114: 79-100, 1993.

Elliot, T., Plank, T., Zindler, A., White, W., Bourdon, B., Element transport from slab to volcanic front at the Mariana arc, J. Petrol. 41: 229-256, 1997.

Elthon, D., Pressure of origin of primary mid-ocean ridge basalts, in Magmatism in the Ocean Basins, edited by A. D. Saunders and M. J. Norry, Geol. Soc. Spec. Publ., 42, 125–136, 1989.

Erbel, DD, Drits, VA, and Środoń, J (1998) Deducing growth mechanisms for minerals from the shapes of crystal size distributions Am. J. Sci. 298:499-533

Fabriés, J. Spinel-olivine geothermometry in peridotites from ultramafic complexes. Contrib. Mineral. Petrol., 69, 329-336, 1979.

Falloon, T.J., Danyushevsky, L.V., and Green, D.H., Peridotite melting at 1 GPa: Reversal experiments on partial melt compositions produced by peridotite-basalt sandwich experiments, J. Petrol. 42: 2636-2390, 2001.

Faure, F., Trolliard, G., Nicollet, C., Montel, J-M., A developmental model of olivine morphology as a function of the cooling rate and the degree of undercooling, Contrib. Mineral. Petrol. 145: 251-263, 2003.

Fisk, M. R., Depths and temperatures of mid-ocean-ridge magma chambers and the composition of their source magmas, in Ophiolites and Oceanic Lithosphere, edited by I. G. Gass, S. J. Lippard, and A. W. Shelton, Geol. Soc. Spec. Publ., 13, 17–32, 1984.

Fisk, M. R., A. E. Bence, and J. G. Schilling, Major element geochemistry of Galapagos Rift Zone magmas and their phenocrysts, Earth. Planet. Sci. Lett., 61, 171–189, 1982.

Ford, C.E., Russell, D.G., Craven, J.A., Fisk, M.R., Olivine-liquid equilibria: Temperature, pressure and compositional dependence of the crystal/liquid cation partition coefficient. J. Petrol. 24: 256-265, 1983.

Forsythe, L.M., Nielsen, R.L. and Fisk, M.R., High field-strength element partitioning between pyroxene and basaltic to dacitic magmas Chem. Geol. 117: 107-125, 1994.

Fram, M. S., and J. Longhi, Phase equilibria of dikes associated with Proterozoic anorthite complexes, Am. Mineral., 77, 117–136, 1992.

Freer, R., Diffusion in silicate minerals and glasses: a data digest and guide to the literature, Contrib. Mineral. Petrol. 76: 440-454, 1981.

Fuijimaki, H. and Tatsumoto, M. Partition coefficients of Hf, Zr and REE between phenocrysts and groundmass, J. Geophys. Res. 89: 662-672: 1984

Furukawa, Y. Magmatic processes under arcs and formation of the volcanic front. J. Geophys. Res., 98: 8309-8319, 1993.

Gaetani, G. A. and Watson, E. B., Modeling the major-element evolution of olivine hosted melt inclusions, Chem. Geol. 183: 25-41, 2002.

Gaetani, G. A. and Watson, E. B., Open system behavior of olivine-hosted melt inclusions, Earth Planet. Sci. Lett. 183: 27-41, 2000.

Gaetani, Glenn A. Grove, Timothy L. Bryan, Wilfred B., The influence of water on the petrogenesis of subduction-related igneous rocks, Nature, 365: 332-334, 1993.

Garrido, C. J., Kelemen, P.B., and Hirth, G., Variation of cooling rate with depth in lower crust formed at an oceanic spreading ridge: plagioclase size distributions in gabbros from the Oman ophiolite, Geochem, Geophys, Geosyst. 2 doi:10.1029/2000GC000136, 2001.

Ghiorso, M. S., and R. O. Sack, Chemical mass transfer of in magmatic processes; IV, A revised and internally consistent thermodynamic model for the interpolation and extrapolation of liquid-solid equilibria in magmatic systems at elevated temperatures and pressures, Contrib. Mineral. Petrol., 119, 197–212, 1995.

Gill, J.B., Orogenic andesite and plate tectonics. Springer-Verlag, New York, 1981.

Gribble, Stern, Bloomer, S., Stuben, O'Hearn, Newman., MORB mantle and subduction components interact to generate basalts in the southern Mariana Trough back-arc basin: Geochimica et Cosmochimica Acta, v. 60, p. 2153-2166, 1996.

Grove, T. L., M. B. Baker, and R. J. Kinzler, Coupled CaAl-NaSi diffusion in plagioclase feldspar: Experiments and application to cooling rate speedometry, Geochim. Cosmochim. Acta, 48, 2113–2121, 1984.

Grove, T.L., Kinzler, R.J., Bryan, W. B., Fractionation of Mid-Ocean Ridge Basalt (MORB) in Mantle Flow and Melt Generation at Mid-Ocean Ridges, Geophysical Mongraph 71: 281-310, 1992.

Gust, D.A., and Perfit, M.R., Phase relations of a high-Mg basalt from the Aleutian island arc: implications for primary island arc basalts and high-Al basalts, Contrib. Mineral. Petrol. 97: 7-18, 1987.

Hall, P.S. and Kincaid, C., Diapiric flow at subduction zones: a recipe for rapid transport, Nature 292: 2472-2475, 2001.

Hart, S. R., A large scale isotope anomaly in the Southern Hemisphere mantle, Nature, 309: 753-757, 1984.

Hawkins J., 2003 High-mg rocks of a Tonga (Tofua) arc seamount: implications for early arc history Geological Society of America Annual Meeting, GSA Abs. Prog., 35, 2003.

Hawkesworth, C.J., Turner, S.P., McDermott, F., Peate, D.W., von Calstern, P. , U-Th isotopes in arc magmas: implications for element transfer from subducted crust, Science 276: 551-555, 1997.

Hibbard, M. J. Petrography to petrogenesis, Prentice Hall, Englewood Cliffs, NJ 587p., 1995.

Higgins, M. D. Measurement of crystal size distributions Am. Mineral. 85: 1105-1116, 2000.

Hirschmann, M., Wiens, D., Peacock, S., Subduction Factory Science Plan: NSF Margins Initiative www.ldeo.columbia.edu/margins/SF_Sci_Plan_revised.pdf , 42 p., 2000.

Hort, M. and Spohn, T. Crystallization calculations for a binary melt cooling at constant rates of heat removal, implications for the crystallization of magma bodies, Earth Planet. Sci. Lett. 107: 463-474, 1991.

Ikeda, Y. Grain size of plagioclase of the basaltic andesite dikes, Iritono, central Abukuma plateau, Can. J. Earth Sci. 14: 1860-1866, 1977.

Jacques, A.L., Green, D.H., Anhydrous melting of peridotite at 0-15 kbar pressure and the generation of tholeiitic basalts. Contrib. Mineral. Petrol. 73: 287-310, 1980.

Jambon, A., Lussiez, P., Clocchiatti, R., Olivine growth rates in a tholeiitic basalt; an experimental study of melt inclusions in plagioclase, Chem. Geol. 96: 277-287, 1992.

Joesten, R.L. Kinetics of coarsening and diffusion-controlled mineral growth. In: Kerrick, DM (ed) Contact metamorphism. Reviews in mineralogy, vol. 26, Mineral. Soc. Am.: 507-582, 1991.

Johnson, .J, Nielsen, R. L., and Fisk, M. R., Plagioclase-hosted melt inclusions in the Steens Mountain Basalts, Southeastern Oregon, Petrol. 4: 267-273, 1996.

Johnson, K. T. M., M. R. Fisk, and H. R. Naslund, Geochemical characteristics of refractory silicate melt inclusions from Leg 140 diabases, Proc. Ocean Drill. Program Sci. Results, 137/140, 131–139, 1995.

Johnson, M.C. and Plank, T., Dehydration and melting experiments constrain the fate of subducted sediments, Geochem. Geophys. Geosys., 1: 199GC000014, 1999.

Johnston, A.D. and Draper, D.S. Near-liquidus phase relations of an anhydrous high-magnesia basalt from the Aleutian Islands: Implications for arc magma genesis and ascent, J. Volcanl. Geotherm. Res., 52: 27-41, 1992.

Karsten, J. L., J. R. Delaney, J. M. Rhodes, and R. A. Liias, Spatial and temporal evolution of magmatic systems beneath the Endeavor Segment, Juan de Fuca Ridge: Tectonic and petrologic constraints, J. Geophys. Res., 95, 19,235–19,256, 1990.

Kelemen, P. B., Shimizu, N. and Salters, V. J. M. Extraction of mid-ocean ridge basalt from the upwelling mantle by focused flow of melt in dunite channels, Nature, 375: 747–753, 1995.

Kennedy, A.K., Lofgren, G.E. and Wasserburg, G.J., An experimental study of trace element partitioning between olivine, orthopyroxene and melt in chondrules: equilibrium values and kinetic effects, Earth Planet. Sci. Lett. 115: 177-195, 1993.

Kent, A.J.R. and Elliot, T.R., Melt inclusions from Marianas arc lavas: implications for the composition and formation of island arc magmas. Chem. Geol. 183: 263-286, 2002.

Kinzler, B.J.; Grove, T.L.; Recca, S.I., An experimental study on the effect of temperature and melt composition on the partitioning of nickel between olivine and silicate melt, Geochim. Cosmochim. Act., 54: 1255-1265, 1990.

Köhler, T.P. and Brey, G.P. Calcium exchange between olivine and clinopyroxene calibrated as a geothermobarometer for natural peridotites from 2 to 60 kb with applications, Geochim. Cosmochim. Act., 54: 2375-2388, 1990.

Kohut, E. J., and R. L. Nielsen, Melt inclusion formation mechanisms and compositional effects in high-An feldspar and high-Fo olivine in anhydrous mafic silicate liquids, Contrib. Mineral. Petrol., in press.

Korenga, J., and P. B. Kelemen, Origin of gabbro sills in the Moho transition zone of the Oman ophiolite: Implications for magma transport in the lower crust, J. Geophys. Res., 102, 27,729–27,749, 1997.

Le Bas, M.J., IUGS reclassification of the high-Mg and picrite volcanic rocks, J. Petrol. 41: 1467-1470, 2000.

Lee, J. and Stern, R.J. Glass inclusions in Mariana arc phenocrysts; a new perspective on magmatic evolution in a typical intra-oceanic arc, J. Geol. 106: 19-33, 1998.

Lofgren, G. An experimental study of plagioclase crystal morphology: Isothermal crystallization Am. J. Sci. 274: 243-273, 1974.

Maclennan, J., D. McKenzie, K. Gronvold, and L. Slater, Crustal accretion under northern Iceland, Earth Planet. Sci. Lett., 191, 295–310, 2001.

Mangan, M. T. Crystal size distribution systematics and the determination of magma storage times: the 1959 eruption of Kilauea volcano, Hawaii J. Volc. Geotherm. Res. 44: 295-302, 1990.

Manton, W. I., Separation of Pb from young zircon by single-bead ion exchange, Chem. Geol., 73: 147-152, 1988.

Marsh, B.D., Crystal-size spectra and kinetics of crystal growth in magma: I. Theory Geol. Soc. Am., Abstr. Programs 16: 585, 1984.

Marsh, B. D. Crystal size distributions (CSD) in rocks and the kinetics and dynamics of crystallization I. Theory Contrib. Mineral. Petrol. 99: 277-291, 1988.

Marsh, B. D., J. Fournelle, J. D. Myers, and Chou, I. -M., On plagioclase thermometry in island arc rocks: Experiments and theory, in Fluid-Mineral Interactions: A Tribute to H. P. Eugster, edited by R. J. Spencer and I.-M. Chou, Geol. Soc. Spec. Publ., 2, 65–83, 1990.

McNeill, A.W. and Danyushevsky, L.V., Compositions and crystallization temperatures of primary melts for hole 896A basalts: evidence from melt inclusion studies, Proc. ODP, Scientific results, 148: 21-35, 1996.

Michael, P. J., McDonough, W. F., Nielsen, R. L., Cornell, W. C., Depleted melt inclusions in MORB plagioclase; messages from the mantle or mirages in the magma chamber? Chem. Geol. 183: 43-61, 2002.

Monzier, M., Robin, C., Eissen, J-P., Cotton, J., Geochemistry vs. seismo-tectonics along the New Hebrides Central Chain (Southwest Pacific), J. Volc. Geotherm. *Res.* 78: 1-29, 1997.

Mueller, R. F. and Saxena, S. K., Chemical petrology with applications to the terrestrial planets and meteorites, Springer-Verlag, New York, 394 p., 1977.

Muncill, G.E. and Lasaga, A.C., Crystal-growth kinetics of plagioclase in igneous systems: one-atmosphere experiments and application of a simplified growth model, Am. Mineral. 72: 299-311, 1987.

Muncill, G.E. and Lasaga, A.C., Crystal-growth kinetics of plagioclase in igneous systems: Isothermal H_2O-saturated experiments and extension of a growth model to complex silicate melts, Am. Mineral. 73: 982-992, 1988.

Muir, I. D., and C. E. Tilley, Basalts from the northern part of the rift zone of the Mid-Atlantic Ridge, J. Petrol., 5, 409–434, 1964.

Myers, J.D. and Johnston, A.D., Phase equilibria constraints on subduction zone magmatism *in* Bebout, G.E., Scholl, D.W., Kirby, S.H., Platt, J.P. eds. Subduction top to bottom, American Geophysical Union, Washington: 229-250, 1996.

Nakamura and Shimikita, Dissolution origin and syn-entrapment compositional change of melt inclusion in plagioclase, Earth Planet. Sci. Lett.161: 119-133, 1998.

Natland, J. H., Partial melting of a lithologically heterogeneous mantle: Inferences from crystallization histories of magnesian abyssal tholeittes from the Siquerios Fracture Zone, in Magmatism in the Ocean Basins, edited by A. D. Saunders and M. J. Norry, Geol. Soc. Spec. Publ., 42, 41–70, 1989.

Natland, J. H., A. C. Adamson, C. Laverne, W. G. Melson, and T. O'Hearn, A compositionally nearly steady-state magma chamber at the Costa Rica Rift: Evidence from basalt glass and mineral data DSDP Sites 501, 504, and 505, Initial Rep. Deep Sea Drill. Proj., 69, 1065–1077, 1983.

Nielsen, R. L., Simulation of igneous differentiation processes, in Modern Methods of Igneous Petrology, Rev. Mineral., vol. 24, edited by J. Nicholls and J. K. Russel, pp. 65–106, Mineral. Soc. of Am., Washington, D. C., 1990.

Nielsen, R. L., and E. J. Kohut, Melt inclusion formation mechanisms in MORB high-An feldspar, Eos Trans. AGU, 81(48), Fall Meet. Suppl., abstract V51A-10, 2000.

Nielsen, R. L., Crum, J., Bourgeois, R., Hascall, K., Forsythe, L. M., Fisk, M. R., Christie, D. M., Melt inclusions in high-An plagioclase from the Gorda Ridge, an example of the local diversity of MORB parent magmas, Contrib. Mineral. Petrol. 122: 34-50, 1995.

Nielsen, R. L., Peter, M. J., Sours-Page, R., Chemical and physical indicators of compromised melt inclusions, Geochim. Cosmochim. Act.62: 831-839, 1998.

Nye, C. J., and M. R. Reid, Geochemistry of primary and least fractionated lavas from Okmok volcano, central Aleutians: Implications for arc magmagenesis, J. Geophys. Res., 91, 10,271–10,287, 1986.

Onuma, K., and T. Tohara, Effect of chromium on phase relations in the join forsterite-anorthite-diopside in air at 1 atm, Contrib. Mineral. Petrol., 84, 174–181, 1983.

Osborn, E. F. and Tait, D. B. The system diopside-anorthite-forsterite Amer. J. Science Bowen Volume: 413-433, 1952.

Panjasawatwong, Y, Danyushevsky, L.V., Crawford, A.J., Harris, K.L., An experimental study of the effects of melt composition on plagioclase-melt equilibria at 5 and 10 kbar: implications for the origin of high-An plagioclase in arc and MORB magmas, Contrib. Mineral. Petrol. 18: 420-435, 1995.

Park, Y. and Hanson, B., Experimental investigation of Ostwald-ripening rates of forsterite in the haploblastic system, J Volcan. Geotherm. Res. 90: 103-113, 1999.

Pearce, J.A. and Peate, D.W., Tectonic implications of the compositions of volcanic arc magmas, Annu. Rev. Earth Planet. Sci. 23: 251-285, 1995.

Pearce, J.A.; Kempton, P.D.; Nowell, G.M.; Noble, S.R., Hf-Nd Element and isotope perspectives on the nature and provenance of mantle and subduction components in Western Pacific arc-basin systems, J. Petrol., 40: 1579-1611, 1999.

Pearce, J.A. and Parkinson, I.J. Trace element models for mantle melting: application to volcanic arc petrogenesis *in* Pritchard, H.M.; Alabaster, T., Narris, N.B.W., Neary, C.R. eds. Magmatic Processes and Plate Tectonics, Geological Society Special Pub. 76: 373-403, 1993.

Philpotts, A.R., Principles of igneous and metamorphic petrology, Prentice Hall, Englewood Cliffs, NJ pp. 215-234, 1994.

Phipps Morgan, J., and Y. J. Chen , The genesis of oceanic crust: Magma injection, hydrothermal circulation, and crustal flow, J. Geophys. Res. 98: 6283–6297, 1993.

Pier, G., Luhr, J. F., Podesek, F.A., Brannon, J. C., Aranda-Gomez, J. J., Correlated Sr-Nd isotopes and trace element abundances in a lherzolite-bearing basanitic suite from the southernmost Basin and Range Province, San Luis Potsoi, Mexico, American Geophysical Union EOS Trans., 68: 1526, 1987.

Plank, T. and Langmuir, C.H., 1998. The chemical composition of subducting sediment and its consequences for the crust and mantle: Chemical Geology, v. 145, p. 325-394.

Presnall, D.C., Dixon, S.A., Dixon, J.R., O'Donnell, T.H., Brenner, N.L., Schrock. R.L., Ducus, D.W., Liquidus phase relations on the join diopside-forsterite-anorthite form 1 atm to 20 kbar: their bearing on the generation and crystallization of basaltic magma, Contrib. Mineral. Petrol. 66: 203-220, 1978.

Qin, Z., Lu, F., Anderson, A.T., Diffusive reequilibration of melt and fluid inclusions, Am. Mineral. 77: 565-576, 1992.

Ramsay, W.R.H., Crawford, A.J., Foden, J.D., Field setting, mineralogy, chemistry and genesis of arc picrites, New Georgia, Solomon Islands, Contrib. Mineral. Petrol. 88: 386-402, 1984.

Ribbe, P. H., Aluminum-silicon order in feldspars: Domain textures and diffraction patterns, in Feldspar Mineralogy, Rev. Mineral., vol. 2, 2nd ed., edited by P. H. Ribbe, pp. 21–54, Mineral. Soc. of Am., Washington, D. C., 1983.

Roeder, P. L., and R. F. Emslie, Olivine-liquid equilibrium, Contrib. Mineral. Petrol., 29, 275–289, 1970.

Roeder, P. L., Campbell, J. H. and Jamieson, H. E. A re-evaluation of the olivine-spinel geothermometer. Contrib. Mineral. Petrol., 68, 325-334, 1979.

Roedder, E. Fluid inclusions: Ribbe, P H (ed) Reviews in Mineralogy, vol. 12. Mineralogical Society of America, Blacksburg, VA, 646p., 1984.

Roggensack, K., Sizing up crystals and their melt inclusions: a new approach to crystallization studies, Earth Planet. Sci. Lett. 187: 221-237, 2001.

Saal, A E, Hart, S R, Shimizu, N, Hauri, E H, Layne, G D, (1998) Pb isotopic variability in melt inclusions from oceanic island basalts, Polynesia, Science, 282: 1481-1484

Sakuyama, M., Lateral variation of H_2O contents in Quaternary magmas of north-eastern Japan. Earth Planet. Sci. Lett. 43:103-111, 1979.

Scott, D.R. and Stevenson, D.J., Magma ascent by porous flow, J. Gephys. Res., 91: 9238-9296, 1986.

Scuth, S., Ronrbach, A., Münker, C., Ballhaus, S., Petrogenesis of arc picrites and basalts from the New Georgia group, Solomon Islands-a geochemical approach, Geophys. Res. Abs. 5: 06541, 2003.

Schwab, B.E. and Johnston, A.D., Melting sytematics of modally variable , compositionally intermediate peridotites and the effects of mineral fertility, J. Petrol. 42: 1789-1811, 2001.

Schwandt, C. and McKay, G.Rare, Earth element partition coefficients from enstatite/melt synthesis experiments. Geochim. Cosmochim. Act 62: 2,845-2,848: 1998

Shimizu, H., Sangen, K. and Masuda, A. Experimental study on rare-Earth element partitioning in minerals formed at 10 and 20 kbar for basaltic systems, Geochem. J. 16: 107-117: 1982

Simkin, T. and Smith, J. V., Minor-element distribution in olivine, J. Geol., 78: 304-325, 1970.

Sinton, C.W., Christie, D.M., Coombs, V. L., Nielsen, R. L., Fisk, M. R., Near-primary melt inclusions in anorthite phenocrysts from the Galapagos Platform, Earth Planet. Sci. Lett. 119: 527-537, 1993.

Sinton, J .M. and Detrick, R .S., Mid-ocean ridge magma chambers, J. Geophys. Res. 97: 197–216, 1992.

Sisson, T.W. and Bronto, S., Evidence for pressure-release melting beneath magmatic arcs from basalt at Galunggung, Indonesia, Nature, 391: 883-886, 1998.

Sisson, T. W., and T. L. Grove, Experimental investigations of the role of H_2O in calc-alkaline differentiation and subduction zone magmatism, Contrib. Mineral. Petrol., 113, 143–166, 1993.

Sisson, T.W. and Layne G.D., H_2O in basalt and basaltic andesite glass inclusions from four subduction related volcanoes, Earth Planet. Sci. Lett. 117:619-635, 1993.

Snyder, V.A., Akaiwa, N., Alkemper, J., and Vorrhees, P.W., The influence of temperature gradients on Ostwald Ripening, Metal. Mater. Trans. A., 30A: 2341-2348, 1999.

Sobolev, A.V., Melt inclusions in minerals as a source of petrological information, Petrology, 4: 228-239, 1996.

Sobolev, A.V. and Shimizu, N., Ultra-depleted primary melt included in an olivine from the Mid- Atlantic Ridge, Nature, 363: 151-154, 1993.

Sours-Page, R., Johnson, K.T.M., Nielsen, R. L., Karsten, J. L., Local and regional variation of MORB parent magmas: evidence from melt inclusions from the Endeavour segment of the Juan de Fuca Ridge, Contrib. Mineral. Petrol. 134: 342-363 , 1999.

Sours-Page, R., Nielsen, R.L., Batiza, R., Melt inclusions as indicators of parental magma diversity on the northern East Pacific Rise, Chem. Geol., 183: 237-261, 2002.

Stern, R .J. Subduction zones, Rev. Geophys. doi:10.1029/2001RG000108, 2002.

Stern, R.J. and Bibee, L.D., 1984. Esmeralda Bank: geochemistry of a submarine volcano in the Mariana Island arc: Contributions to Mineralogy and Petrology, v. 86, p. 159-169.

Stern, R.J.; Fouch, M.J.; Klemperer, S.L., An overview of the Izu-Bonin-Mariana subduction factory, Inside the Subduction Factory, Geophysical Monograph 138, American Geophysical Union, doi: 10.1029/138GM10, 2003.

Student, J. J. and Bodnar, R. J., Melt inclusion microthermometry: petrologic constraints from the H_2O saturated haplogranite system, Petrology, 4: 291-306, 1996.

Student, J. J. and Bodnar, R.J., Modeling the P-V-T-X properties of haplogranite melt inclusions during heating and cooling, Eos Trans., 78: S0429, 1997.

Student, J. J. and Bodnar, R. J., Synthetic fluid inclusions XIV: microthermometric and compositional analysis of coexisting silicate melt and aqueous fluid trapped in the haplogranite-H_2O-NaCl-KCl system at 800° C and 2000 bars, J. Petrol., 40: 1509-1525, 1999.

Tamura, Y., Tatsumi, Y., Zhao, D., Kidoa, Y., Hot fingers in the mantle wedge: new insights into magma genesis in subduction zones, Earth Planet. Sci. Lett. 197: 105-116, 2002.

Tatsumi, Y. Origin of high-magnesian andseites in the Setouchi volcanic belt, southwest Japan, II: melting experiments at high pressures, Earth Planet. Sci. Lett., 60: 305-317, 1982.

Tatsumi, Y. and Eggins, S. Subduction zone magmatism, Blackwell Science, Cambridge, MA, 1995.

Tatsumi, Y., Furukawa, Y., Yamashita, S., Thermal and geochemical evolution of the mantle wedge in the NE Japan arc I: contribution from experimental petrology. J. Geophys. Res. 1994.

Taylor, S.R. and Mclennan, S.M., The geochemical evolution of the continental crust Reviews in Geophysics 33: 241-265, 1995.

Watson E. B., Glass inclusions as samples of early magmatic liquid: determinative method and application to a South Atlantic basalt, J. Volcanol. Geotherm. Res. 148: 527-544., 1976.

Yamakazi, T. and Stern, R.J., Topography and magnetic vector anomalies in the Mariana Trough, JAMSTEC J. Deep Sea Res. 13, 1997.

Yoder, H.S. and Tilley, C.E. Origin of basalt magmas: and experimental study of natural and synthetic rock systems, J. Petrol. 3: 342-532, 1962.

Wallace, P. J., Volatiles in submarine basaltic glasses from the Northern Kerguelen Plateau (ODP Site 1140): Implications for source region compositions, magmatic processes and plateau subsidence, J. Petrol. 43: 1311-1326, 2002.